Generation of Squeezed Light in Semiconductors

Gian-Mattia Schucan

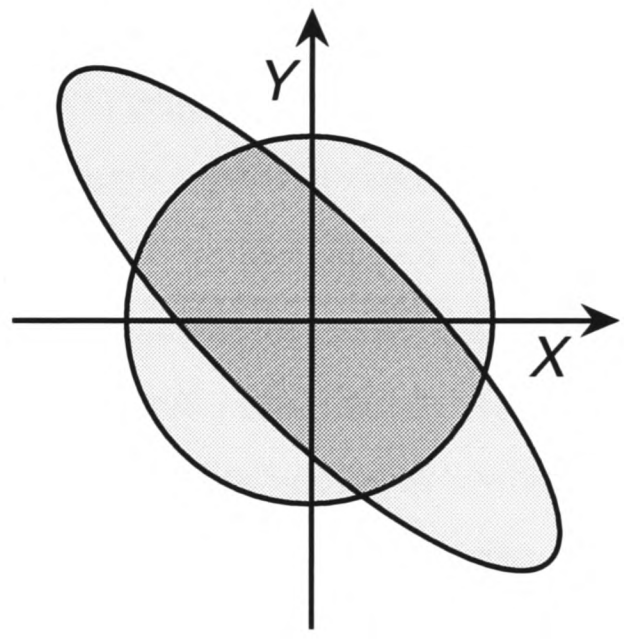

Clarendon Laboratory

Department of Physics

University of Oxford

Thesis submitted for the degree of

Doctor of Philosophy

Merton College

Trinity Term 1998

Generation of Squeezed Light in Semiconductors

Gian-Mattia Schucan

Merton College, Oxford

Thesis submitted for the degree of Doctor of Philosophy

Trinity Term 1998

Abstract

We present experimental studies based on all three methods by which the generation of squeezed light in semiconductors has thus far been demonstrated experimentally: Four-wave mixing, multi-photon absorption and direct generation at the source.

Four-wave mixing was used to generate femtosecond-pulsed quadrature squeezed light by cross-phase modulation in single-crystal hexagonal CdSe at wavelengths between 1.42 and 1.55 μm. We measured 0.4 dB squeezing (1.1 dB is inferred at the crystal) using 100 fs pulses. The wavelength and the intensity dependence, as well as variations in the local oscillator configuration were investigated. At higher intensities squeezing was shown to deteriorate owing to competing nonlinear processes. We also characterised the nonlinear optical properties of CdSe in this wavelengths range using an interferometric autocorrelator. In addition, we studied the feasibility of extending this technique to AlGaAs waveguides. The key problems are addressed and solutions are proposed.

In a different experiment we used an AlGaAs waveguide to demonstrate for the first time photon-number squeezing by multi-photon absorption. By tuning the pump energy through the half bandgap energy we could effectively select two- or three-photon absorption as the dominant mechanism. Squeezing by these two mechanisms could be clearly distinguished and was found to be in good agreement with longstanding theoretical predictions. We also established the generality of the effect, by demonstrating the same mechanism in organic semiconductors, where it led to the first ever observation of squeezed light in an organic material.

Finally, we present our measurements of photon-number squeezing in high-efficiency double heterojunction AlGaAs light-emitting diodes. We measured squeezing of up to 2.0 dB. In addition, we observed quantum noise correlations when several of these devices were connected in series.

To my parents

Acknowledgements

I would like to gratefully acknowledge:

- My supervisors Prof. John F. Ryan and Dr. A. Mark Fox for their total support, their guidance and many good ideas and suggestions.
- Dr. Rudolf H. Morf for his contagious enthusiasm and the support in setting it all up.
- Prof. J. M. Baker and Prof. R. A. Cowley for making available the facilities of the Clarendon laboratory.
- The Greendale Foundation, Merton College, and the Committee of Vice-Chancellors and Principles of the Universities of the United Kingdom for funding my studies here in Oxford.
- Drs. J. S. Aitchison, C. N. Ironside, and K. J. Donovan for providing the samples.
- M. B. Ward, F. Wölfl, E. D. O'Sullivan, Drs. K. Turner, M. Dabbicco, G. von Plessen, R. G. Ispasoiu, and T. Goodson III for the excellent collaboration.
- The "Foreign Office" for all the support and fun.
- All the other members of the group for passing on all those clever tricks and helping me to find the missing lens.
- All of the technical staff of the Clarendon laboratory, far too many to list here.
- My friends at Merton and elsewhere, who made sure I had such an excellent time here in Oxford.
- Charlotte for all her love and her 3547 email messages.
- My family for all their love and support.

Publications

Journals:

1. **Femtosecond quadrature squeezed light generation in CdSe at 1.55 μm.**

   G.-M. Schucan, A. M. Fox, and J. F. Ryan

   Opt. Lett. **23**, 712–714 (1998).

2. **Improved photon-number squeezing in light-emitting diodes.**

   F. Wölfl, G.-M. Schucan, A. M. Fox, and J. F. Ryan

   J. Mod. Opt. **45**, 1147–1153 (1998).

3. **Ultrafast two-photon nonlinearities in CdSe near 1.5 μm studied by interferometric autocorrelation.**

   G.-M. Schucan, R. G. Ispasoiu, A. M. Fox, and J. F. Ryan

   IEEE J. Quant. Electr. **34**, 1374–1379 (1998).

4. **Generation of photon-number squeezed light by multiphoton absorption.**

   G.-M. Schucan, M. B. Ward, K. Turner, T. Goodson III, A. M. Fox, and J. F. Ryan; J. S. Aitchison and C. N. Ironside

   submitted to Phys. Rev. Lett.

5. **Generation of bright squeezed light in organic polymers.**

   T. Goodson III, K. Turner, M. B. Ward, G.-M. Schucan, K. J. Donovan, A. M. Fox, and J. F. Ryan

   submitted to Science.

Publications cont'd

Conferences:

6. **Nonlinear semiconductor waveguides for quantum communication systems.**

   G.-M. Schucan, M. Dabbicco, A. M. Fox, G. von Plessen, and J.F. Ryan

   Proceedings of the 23rd ICPS, ed. M. Scheffler and R. Zimmermann (World Scientific Press, Singapore, 1996), pp. 3235-3238.

7. **Generation of quadrature squeezed light by cross-phase modulation in semiconductors.**

   G. von Plessen, A. M. Fox, M. Dabbicco, G.-M. Schucan, and J. F. Ryan

   Presented at CLEO/Europe (Hamburg, 1996).

8. **Interferometric autocorrelation measurements of ultrafast two-photon nonlinearities in CdSe.**

   R. G. Ispasoiu, G.-M. Schucan, E. D. O'Sullivan, A. M. Fox, and J. F. Ryan

   Presented at IQEC (San Francisco, 1998).

9. **Generation of amplitude squeezed states of light in an organic non-linear optical polymer PTS-PDA.**

   T. Goodson III, K. Turner, M. B. Ward, G.-M. Schucan, A. M. Fox, K. J. Donovan, and J. F. Ryan

   Presented at SPIE Annual Meeting (San Diego, 1998).

10. **Femtosecond squeezed light generation in CdSe at 1.55 μm.**

    G.-M. Schucan, A. M. Fox, and J. F. Ryan

    Presented at EQEC (Glasgow, 1998).

Publications cont'd

11. **Photon-number squeezed light generation by multi-photon absorption.**

    M. B. Ward, G.-M. Schucan, K. Turner, T. Goodson III, K. J. Donovan, J. S. Aitchison, C. N. Ironside, A. M. Fox, and J. F. Ryan

    Postdeadline paper presented at EQEC (Glasgow, 1998).

Contents

1 Introduction **5**

2 Squeezed light **10**

2.1 Introduction 11

2.2 Theoretical foundations 11

2.2.1 Standard quantum limit 11

2.2.2 Quadrature squeezing 14

2.2.3 Number-phase squeezing 17

2.2.4 Relation between quadrature and photon-number squeezing . . . 18

2.3 Generation of squeezed light 21

2.3.1 Generation of quadrature squeezed light 21

2.3.2 Generation of photon-number squeezed light 23

3 Midgap nonlinear optical properties of semiconductors **25**

3.1 Introduction 26

3.2 Constitutive relation 26

3.3 Nearly degenerate four-wave mixing 28

3.3.1 Self-phase modulation 29

3.3.2 Cross-phase modulation 31

3.4 Stimulated Raman scattering 32

3.5 Multi-photon absorption 35

4 Experimental apparatus and techniques **38**

4.1 Laser system 39

4.1.1 Argon ion laser 39

4.1.2 Ti:sapphire laser 39

4.1.3 Optical parametric oscillator 40

4.2 Interferometric autocorrelator 42

4.3 Detection systems 43

4.3.1 Quadrature squeezing detection 44

4.3.2 Photon-number squeezing detection 48

5 Ultrafast two-photon nonlinearities in CdSe **50**

5.1 Introduction 51

5.2 Experimental setup 53

5.3 Nonlinear absorption 53

5.4 Autocorrelations 58

5.4.1 Measurements 58

5.4.2 Calculations 60

5.5 Nonlinear figure of merit 64

5.6 Spectra 65

5.7 Conclusions 67

6 Quadrature-squeezed light generation in CdSe **68**

6.1 Introduction 69

6.2 Experimental setup 70

6.3 Results 72

6.3.1 Intensity and wavelength dependence 74

6.3.2 Alternative local oscillator arrangement 76
6.3.3 Discussion 77
6.4 Feasibility of extending the XPM-technique to waveguides 79
6.4.1 Self-phase modulation 80
6.4.2 XPM-squeezing 80
6.5 Conclusions and outlook 83

7 Photon-number squeezing by multi-photon absorption **85**
7.1 Introduction 86
7.2 Experimental setup 88
7.3 Experimental results for AlGaAs-waveguide 89
7.3.1 Nonlinear transmission 89
7.3.2 Squeezing 91
7.4 Theoretical considerations 92
7.5 MPA-squeezing in organic semiconductor 96
7.6 Conclusions and outlook 100

8 Photon-number squeezing in light emitting diodes **102**
8.1 Introduction 103
8.2 Experimental setup 104
8.3 Results 106
8.3.1 Photon-number squeezing in single LED 106
8.3.2 Correlation effects in multiple LEDs in series 107
8.4 Conclusions and outlook 110

A Sample descriptions **112**
A.1 AlGaAs-waveguide 112
A.2 PTS-PDA sample 113

Bibliography **115**

Chapter 1

Introduction

Since the original demonstration of squeezed state generation in sodium vapour by Slusher *et al.* in 1985 [1], squeezed light has been generated in a variety of different media and geometries. In parallel, a number of potential applications ranging from gravity wave detection to improved channel capacity in optical communications have been investigated. Convenient sources of squeezed light are therefore of great interest and substantial research efforts have been devoted to them. Due to their advanced fabrication technology and their potential for integration, semiconductors could form the basis for such sources. Up to now, three fundamental methods of generating squeezed light in semiconductors have been experimentally demonstrated (in chronological order):

- Photon-number squeezing by *direct conversion* of quiet current statistics using high-efficiency light emitters.
- Quadrature squeezing by *four-wave mixing.*
- Photon-number squeezing by *multi-photon absorption.*

The present thesis contains work in all three areas.

The direct conversion approach was first demonstrated by Teich and Saleh in 1985 [2] and then extended to semiconductor devices in 1987, by Machida *et al.* for laser diodes [3] and by Tapster *et al.* for light emitting diodes (LEDs) [4]. A number of interesting applications for the squeezed light generated by this method have been proposed and demonstrated, such as noiseless taps, amplifiers and optical beam splitters [5, 6]. Here the direct conversion approach is used to obtain strong squeezing from low-cost LEDs and to investigate quantum correlations in series-connected emitters [7].

Four-wave mixing was already used in the aforementioned experiment by Slusher *et al.* [1] and was extended to semiconductors by Fox *et al.* in 1995 [8, 9]. The latter technique uses femtosecond pulses in a single pass through bulk semiconductors and therefore does not rely on cavity-enhancement. Here we further extend this technique to the technologically important wavelength range around 1.5 μm using CdSe [10, 11] and study the feasibility of using it in optical waveguides. This method could be applied in future integrated sources of quadrature squeezed light.

Finally, photon-number squeezing by multi-photon absorption is demonstrated for the first time [12, 13]. This squeezing mechanism was predicted as early as 1974 [14, 15], but has never been observed experimentally. We present measurements of squeezing by two- and three-photon absorption both in an AlGaAs waveguide and in an organic semiconductor (PTS-PDA, p-toluene sulphonate polydiacetylene). This constitutes also the first observation of squeezing in an organic material. We expect this new technique to be applicable at all optical frequencies. This could lead to a wide variety of applications in sub-shot-noise spectroscopy.

The thesis is structured as follows:

Chapter 2

In Chapter 2 the basic concepts of squeezed light are reviewed. We discuss the theoretical foundations of both quadrature squeezed light and number-phase squeezed light as well as their mutual relations. The basic mechanisms for the generation of squeezed light are presented.

Chapter 3

Chapter 3 is concerned with the nonlinear optical processes which arise near the midgap of semiconductors which are relevant to this thesis. After giving the constitutive relation for nonlinear optics we discuss nearly degenerate four-wave mixing, self- and cross-phase modulation as well as stimulated Raman scattering and multi-photon absorption.

Chapter 4

In Chapter 4 some of the experimental apparatus and techniques are described. We discuss the femtosecond laser system, namely the optical parametric oscillator as well as the autocorrelator used to characterise the laser pulses. The chapter ends with a more detailed description of the systems used for the detection of squeezed light including the underlying theoretical principles and the diagrams of the custom-made electronics.

Chapter 5

In Chapter 5 the nonlinear optical properties of CdSe are investigated and it is shown to be a suitable nonlinear material for the technologically important wavelength range around 1.5 μm. First we study the nonlinear absorption in this wavelength region. Then we show that interferometric autocorrelations are a useful tool to determine the nonlinear refractive index in the femtosecond range where the interpretation of spectral

data becomes increasingly difficult. In addition, we find that free carrier absorption modifies the autocorrelations traces, and including this effect in the theoretical model leads to very good agreement with the experimental results. We then estimate the nonlinear figure of merit of CdSe and show that it compares favourably with AlGaAs as a nonlinear optical material in this wavelength range.

Chapter 6

Chapter 6 is mainly dedicated to studies of quadrature squeezed light in CdSe generated by cross-phase modulation. Maximum squeezing of 0.4 dB (1.1 dB is inferred at the crystal) was measured. We studied the behaviour of the squeezing as a function of both wavelength and pump intensity. We found that above a certain peak intensity the squeezing saturates and the noise increases again. Finally, we discuss the feasibility of extending this technique to AlGaAs waveguides. The key problems are addressed and solutions are proposed.

Chapter 7

In Chapter 7 we present our experimental discovery of squeezing by multi-photon absorption (MPA). The experiments were carried out in an AlGaAs waveguide, where both two-photon absorption and three-photon absorption can be selected by choosing the appropriate wavelength. We compare our results with longstanding theoretical predictions and find a good agreement. We then extend this technique to the organic semiconductor PTS-PDA where it is found to produce squeezed light extremely efficiently. Apart from showing the general applicability of MPA-squeezing, this is also the first demonstration of squeezing in an organic material. In concluding the chapter, we discuss the universality of the effect that could form the basis of sources of squeezed light over a broad range of wavelengths.

Chapter 8

Chapter 8 is concerned with the third possibility of producing squeezed light in semiconductor devices, i.e. the direct conversion approach. First we show squeezing levels of as much as 40% in low-cost commercially available LEDs. We then use LEDs of this type to perform experiments with several devices connected in series, where interesting quantum correlation effects are seen.

Appendix A

Appendix A.1 provides a description of the waveguide sample used in the feasibility study for quadrature squeezing in AlGaAs waveguides in § 6.4 and for the MPA-squeezing presented in Chapter 7. In Appendix A.2 the PTS-PDA sample used in Chapter 7 is described including details about the growth process and the chemical structure.

The calculations of the interferometric autocorrelations were performed by R. G. Ispasoiu. The work on squeezing by multi-photon absorption was done in conjunction with M. B. Ward, K. Turner and T. Goodson, and the experiments on squeezing in LEDs were performed in collaboration with F. Wölfl.

Chapter 2

Squeezed light

Contents

2.1 Introduction 11

2.2 Theoretical foundations 11

2.3 Generation of squeezed light 21

2.1 Introduction

The present chapter provides the theoretical background to understanding the phenomena associated with squeezed light. Both quadrature squeezing and photon-number squeezing, as well as their mutual relation are discussed in § 2.2. A brief overview of the possible ways of generating such light is given in § 2.3.

2.2 Theoretical foundations

The quantum mechanical foundations are now reviewed, following and illustrating a treatment given by Davidovich [16].

2.2.1 Standard quantum limit

Optical fields obey the laws of quantum mechanics and have an inherent quantum indeterminacy which can not be removed no matter how carefully the light source is controlled. Let us consider the electric field operator corresponding to a mode of the electromagnetic field in a cavity[1] with volume V, with angular frequency ω, at time t (assumed for simplicity to be linearly polarised):

$$\hat{E}(t) = \frac{E_0}{2}(\hat{a}e^{-i\omega t} + \hat{a}^\dagger e^{i\omega t}), \tag{2.1}$$

where $E_0 = (\hbar\omega/V)^{1/2}$ is the one-photon field, $\hat{a}$ and $\hat{a}^\dagger$ are the photon annihilation and creation operators, with $[\hat{a}, \hat{a}^\dagger] = 1$. We can also write the electric field as

$$\hat{E}(t) = E_0(\hat{X}\cos\omega t + \hat{Y}\sin\omega t), \tag{2.2}$$

where $\hat{X}$ and $\hat{Y}$ are the *quadrature component* operators, given by

$$\hat{X} = \frac{1}{2}(\hat{a} + \hat{a}^\dagger), \qquad \hat{Y} = -i\frac{1}{2}(\hat{a} - \hat{a}^\dagger), \tag{2.3}$$

[1] This formulation can be generalised readily to propagating fields [17].

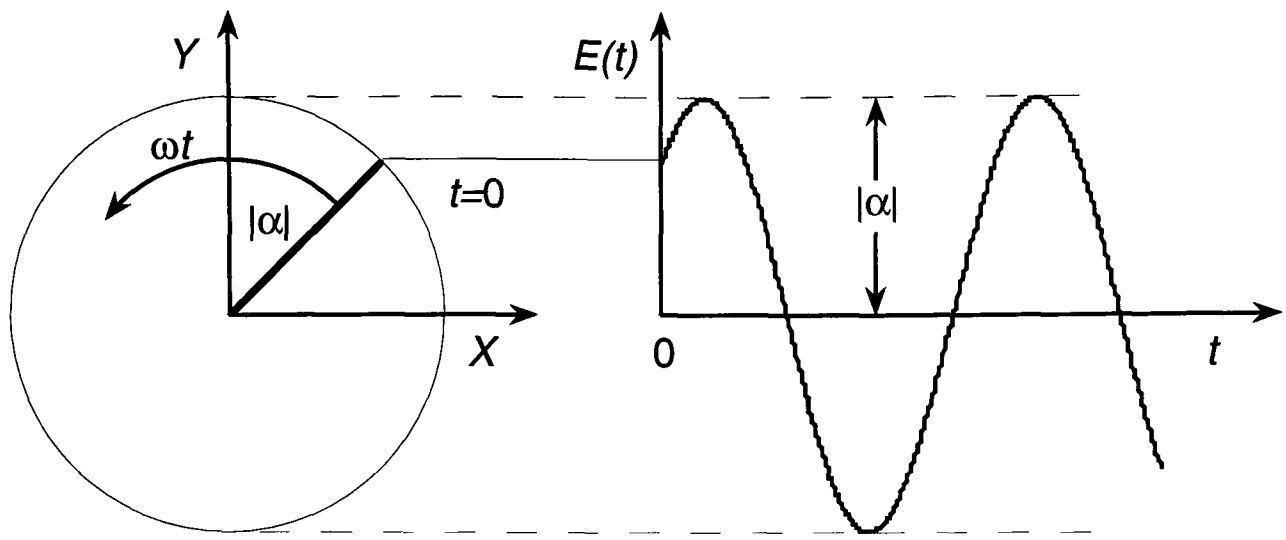

Figure 2.1: Classical representations of an electric field of amplitude $|\alpha|$.

so that

$$[\hat{X}, \hat{Y}] = \frac{i}{2}. \tag{2.4}$$

Fig. 2.1 shows two equivalent classical representations of the electric field according to (2.2). The left hand side of the figure shows a rotating phasor whose projection on the Y-axis determines the sinusoidal electric field shown on the right hand side. The quadrature components X and Y of the phasor are a quarter cycle ($\frac{\pi}{2}$) out of phase with each other. The rotating phasor also describes the motion of a classical harmonic oscillator: the X-component is proportional to the position and the Y-component to the momentum. The equivalence to a quantum mechanical harmonic oscillator can be seen from the definitions (2.3) of the quadratures $\hat{X}$ and $\hat{Y}$ [18].

From the commutation relation (2.4) it follows that the product of the fluctuations in the measurement of the two quadratures $\hat{X}$ and $\hat{Y}$ satisfies a Heisenberg inequality:

$$\Delta X \Delta Y \geq \frac{1}{4}, \tag{2.5}$$

where $\Delta X = (\langle\psi|\widehat{\Delta X}^2|\psi\rangle)^{1/2}$ for any state $|\psi\rangle$.

For *coherent states* [19], (2.5) is satisfied as an equality, and the two fluctuation components are identical: $\Delta X = \Delta Y = \frac{1}{2}$, i.e., they are at the *Standard quantum limit*

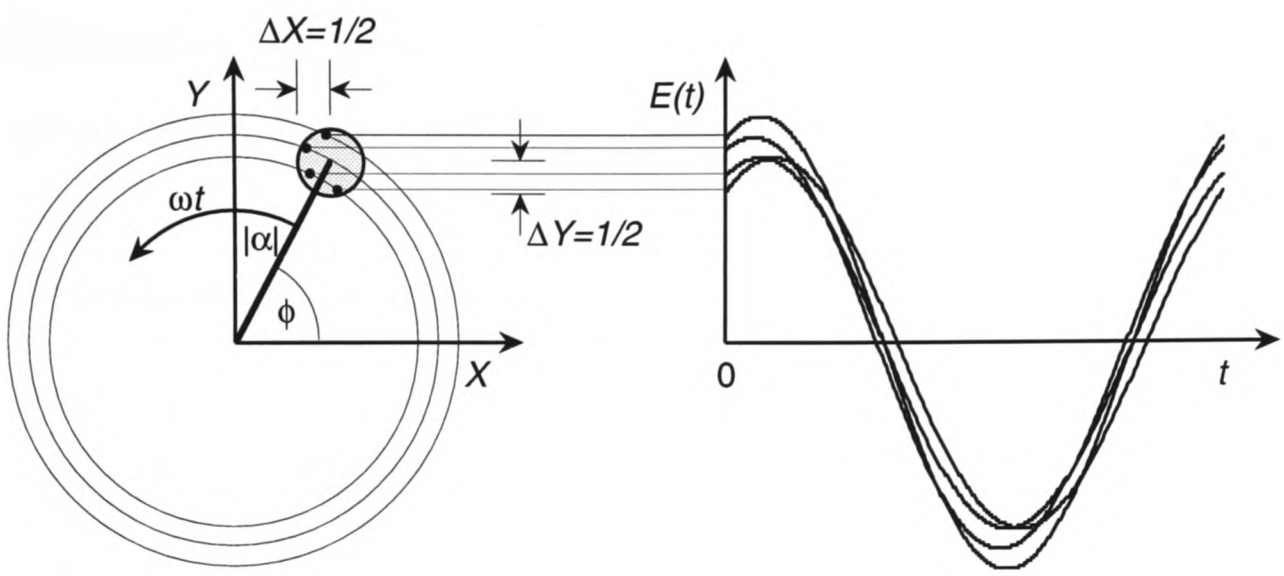

Figure 2.2: Uncertainties for the coherent state. Representative illustrations of $E(t)$ are drawn by choosing arbitrary points in the uncertainty circle.

(SQL) or *shot noise limit.* The coherent state is the closest quantum approximation to the field generated by a laser. It corresponds to a harmonic oscillator state, and can be obtained from the vacuum state $|0\rangle$ (or the ground state of the harmonic oscillator) by applying a displacement operator $\hat{D}(\alpha)$:

$$|\alpha\rangle = \hat{D}(\alpha)|0\rangle = \exp(\alpha\hat{a}^\dagger - \alpha^*\hat{a})|0\rangle, \tag{2.6}$$

where $\alpha = |\alpha|\exp(i\phi)$ is a complex number, corresponding to the phasor representation of the electromagnetic field, where $|\alpha|$ represents the amplitude of the field and ϕ its phase. This is shown in Fig. 2.2. The shaded circle at the tip of the phasor expresses the uncertainty. The state $|\alpha\rangle$ is an eigenstate of the annihilation operator $\hat{a}$:

$$\hat{a}|\alpha\rangle = \alpha|\alpha\rangle. \tag{2.7}$$

It can be expanded in terms of Fock states of the field (eigenstates $|n\rangle$ of the number operator $\hat{n} = \hat{a}^\dagger\hat{a}$):

$$|\alpha\rangle = e^{-|\alpha|^2/2}\sum_{n=0}^{\infty}\frac{\alpha^n}{\sqrt{n!}}|n\rangle. \tag{2.8}$$

This corresponds to a Poisson distribution of the photon number:

$$p(n) = |\langle n|\alpha\rangle|^2 = \exp(-|\alpha|^2)\frac{|\alpha|^{2n}}{n!} = \exp(-\langle n\rangle)\frac{\langle n\rangle^n}{n!}. \tag{2.9}$$

For this distribution, the variance of the photon number $\langle \Delta n^2 \rangle$ is equal to the mean photon number $\langle n \rangle$. Note that the coherent states form a overcomplete basis set.

2.2.2 Quadrature squeezing

Coherent states are of course not the only possibilities to satisfy Heisenberg's uncertainty principle (2.5). A particularly interesting set of states are the *quadrature squeezed states*, where the noise in one of the quadratures is "squeezed" below that of a coherent state. This happens at the expense of increasing the noise in the other quadrature, preventing the Heisenberg inequality from being violated.

One particular class of squeezed states can be created from the vacuum state using the following unitary transformation [20]

$$\hat{S}(\xi) = \exp\left[(\xi^* \hat{a}^2 - \xi \hat{a}^{\dagger 2})/2\right], \tag{2.10}$$

where $\xi = r_s e^{i2\theta_s}$ is an arbitrary complex number. This transformation amounts to compressing and stretching the uncertainty area in the two rotated quadratures $\hat{X}'$ and $\hat{Y}'$ (cf. Fig. 2.3), defined by

$$\hat{X}' + i\hat{Y}' = (\hat{X} + i\hat{Y})e^{-i\theta_s}. \tag{2.11}$$

It can be shown that the variances in the state $|\xi\rangle = \hat{S}(\xi)|0\rangle$ become,

$$\langle \xi | \widehat{\Delta X'}^2 | \xi \rangle = \frac{1}{4} e^{-2r_s}, \qquad \text{and} \qquad \langle \xi | \widehat{\Delta Y'}^2 | \xi \rangle = \frac{1}{4} e^{2r_s}. \tag{2.12}$$

The above transformation therefore has the effect of producing a quadrature squeezed state with noise below that of the vacuum state in a quadrature making an angle θ_s with respect to the original phase-space axis. The parameter r_s is called the *squeeze parameter*, the state $|\xi\rangle$ is called *squeezed vacuum* and the unitary transformation $\hat{S}(\xi)$ is called the *squeeze operator*. Fig. 2.4 shows the relation between the unsqueezed (a) and the squeezed vacuum (b) and the translation of the uncertainty areas into electric field pictures. While

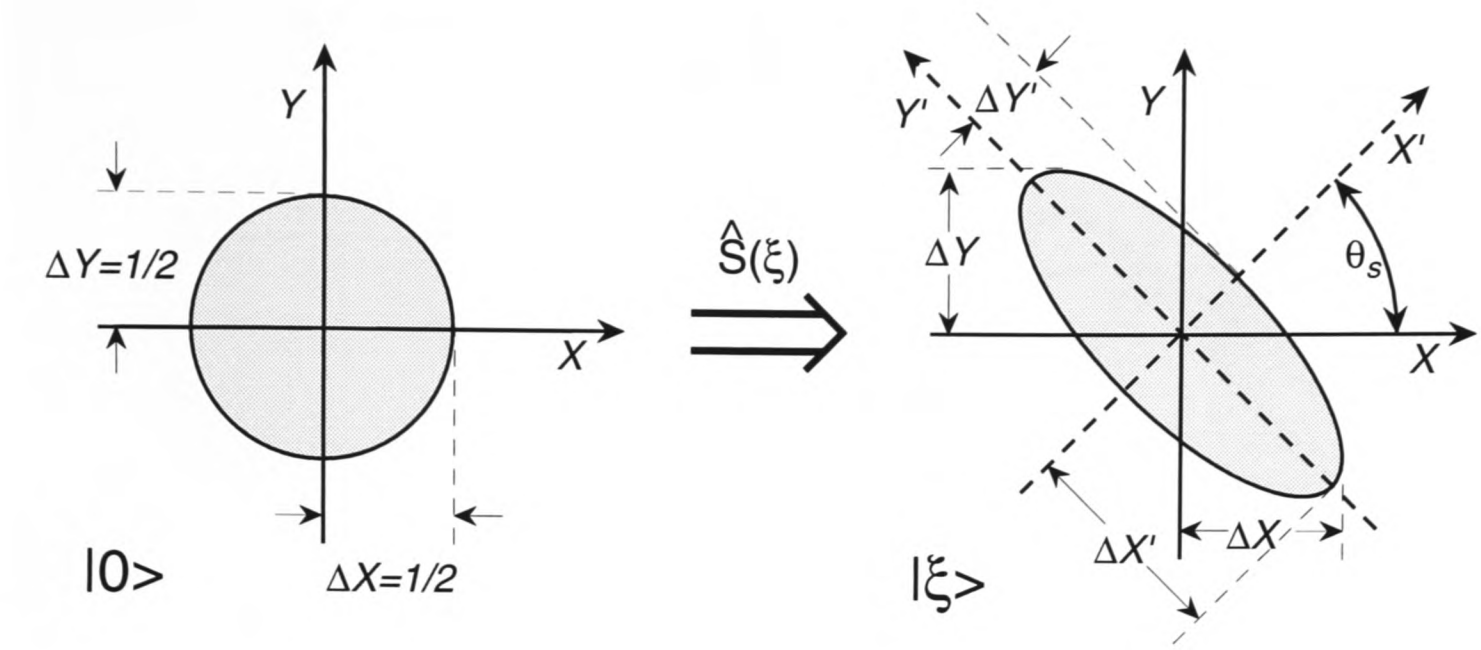

Figure 2.3: The action of the squeezing operator $\hat{S}(\xi)$ on the uncertainty circle of the vacuum state $|0\rangle$: the circle is squeezed into an ellipse of equal area to form a squeezed vacuum state $|\xi\rangle$. The symbols are explained in the text.

the noise is constant as a function of phase for the unsqueezed case, the squeezed vacuum exhibits phase-dependent noise, as can be seen from both the phasor and the electric field representation. Note that the term *squeezed vacuum* is somewhat misleading, because its average photon number is different from zero.[2] Indeed,

$$\langle \xi | \hat{a}^\dagger \hat{a} | \xi \rangle = \sinh^2 r_s. \tag{2.13}$$

A more general class of states can be obtained by first squeezing the vacuum, and then displacing it [20]:

$$|\alpha, \xi\rangle = \hat{D}(\alpha)\hat{S}(\xi)|0\rangle. \tag{2.14}$$

Eqs. (2.12) remain valid for these states. The average photon number is now given by

$$\langle \alpha, \xi | \hat{a}^\dagger \hat{a} | \alpha, \xi \rangle = |\alpha|^2 + \sinh^2 r_s. \tag{2.15}$$

[2]This point is thus far of purely theoretical interest, as the squeezing levels observed to date would not allow this increase in average photon number to be detected directly.

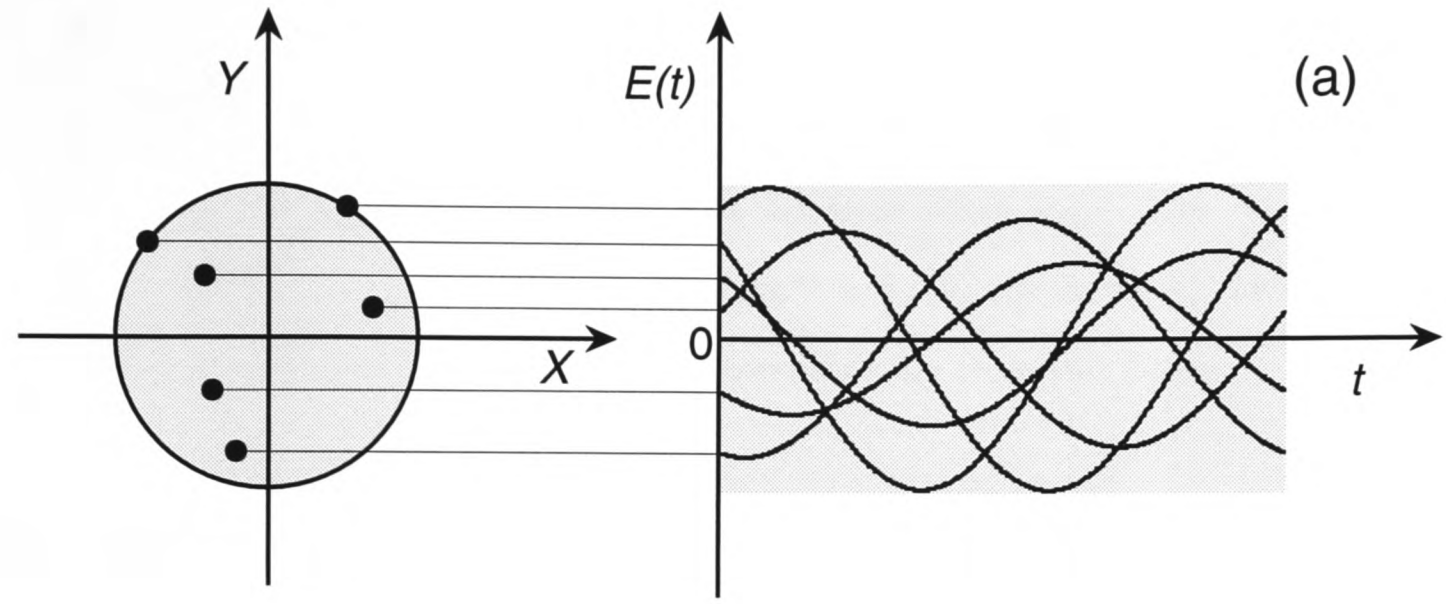

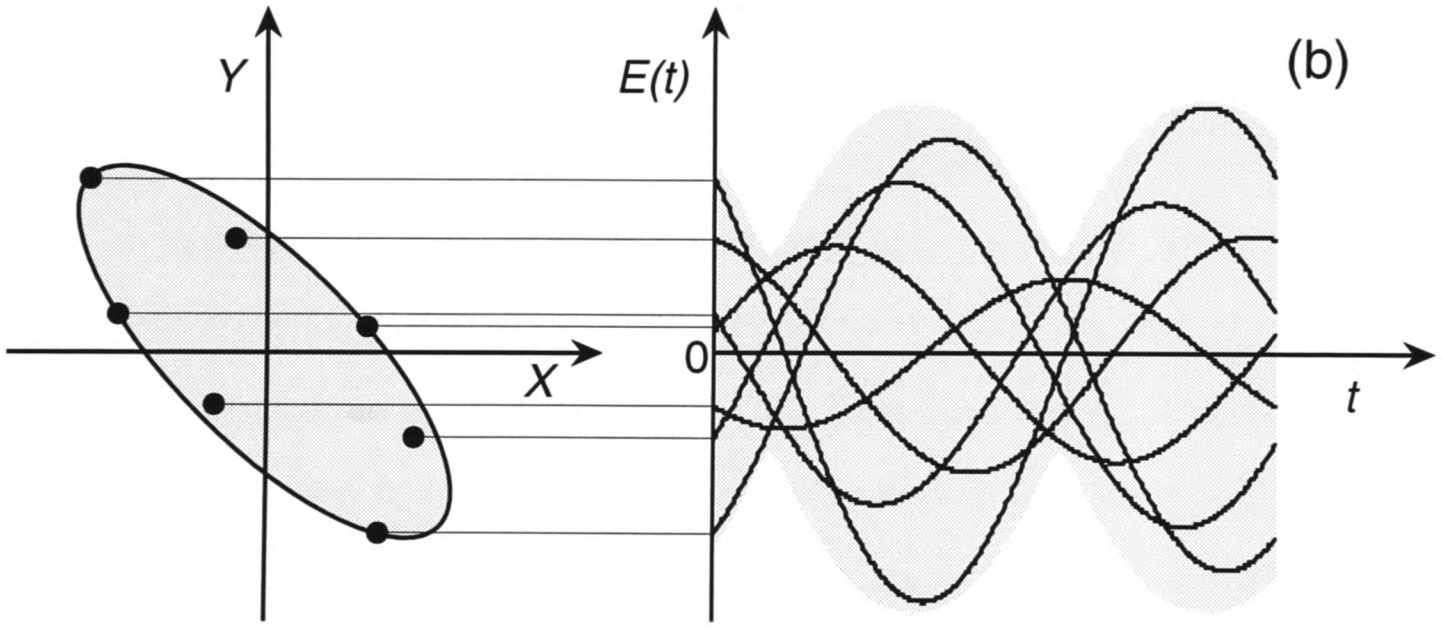

Figure 2.4: Uncertainties for the vacuum state (a) and for the squeezed vacuum (b). The noise is independent of the phase for the vacuum state, but strongly phase-dependent for the squeezed vacuum.

Again we see that the squeezed state contains more photons than its underlying coherent state.

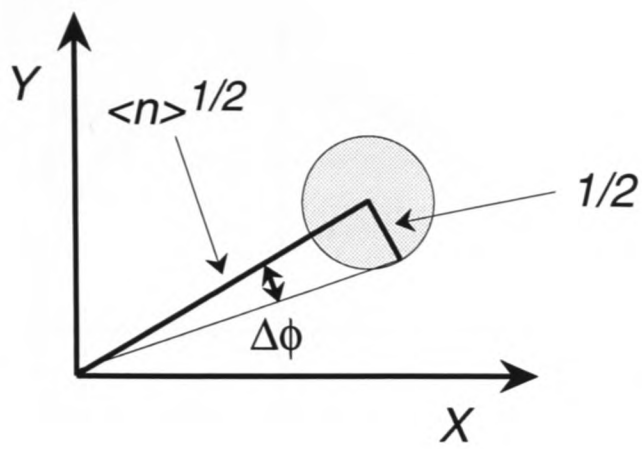

Figure 2.5: Phase uncertainty for a coherent state $|\alpha\rangle$. The relation $\langle\Delta\phi^2\rangle = \frac{1}{4}/\langle n\rangle$ can be easily deduced geometrically from this figure.

2.2.3 Number-phase squeezing

A related, though not equivalent, class of quantum-noise-compressed states are the *number-phase squeezed states.* The precise definition of these states requires the introduction of an operator corresponding to the phase of the electromagnetic field. Finding a Hermitian phase operator has long been a problem [21, 22]. Only in 1988/89, Pegg and Barnett [23, 24] showed how to construct a Hermitian phase operator, the eigenstates of which, in an appropriate limit, generate the correct phase statistics for arbitrary states. For a coherent state $|\alpha\rangle$, with $|\alpha| \gg 1$, its average value coincides with the phase of $|\alpha\rangle$, while its variance is given by $\langle\Delta\phi^2\rangle = \frac{1}{4}/\langle n\rangle$ [25]. Note that the same value for the variance would be obtained from the phase-space picture (Fig. 2.5), in the limit of a large average photon number $\langle n\rangle$. Since, for a coherent state, the photon-number variance $\langle\Delta n^2\rangle$ is given by $\langle\Delta n^2\rangle = \langle n\rangle$, we have $\langle\Delta n^2\rangle\langle\Delta\phi^2\rangle = \frac{1}{4}$, which represents the standard quantum limit in this case. Squeezing in photon number or in phase is obtained when the respective fluctuations get smaller than those for the coherent state. These states are called *photon-number squeezed* and *phase squeezed* states. As coherent states have a Poissonian photon-number distribution (cf. Eq. (2.9)), photon-number squeezed states are also referred to as sub-Poissonian states.

The number-phase squeezed states are also "nonclassical", in the same sense as quadrature squeezed states. A strongly photon-number squeezed state is shown in Fig. 2.6: The photon number is very clearly defined, the phase is completely random.

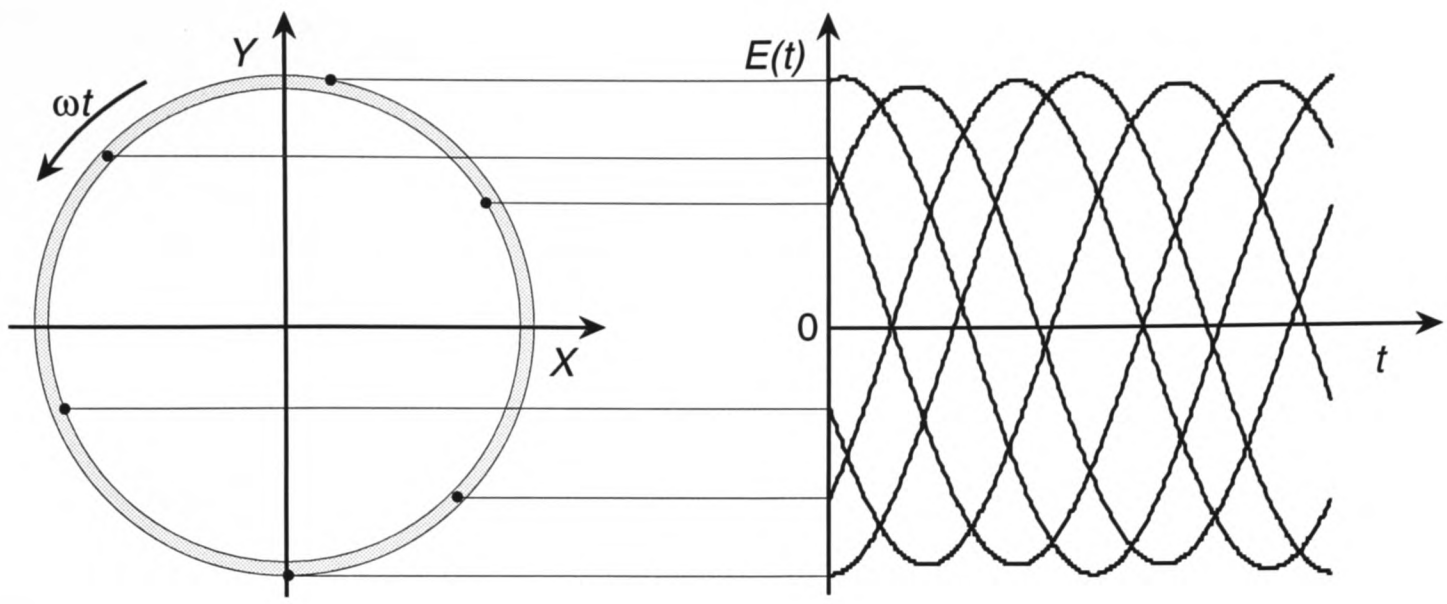

Figure 2.6: Uncertainty area and electric field picture of a strongly photon-number squeezed state with random phase.

2.2.4 Relation between quadrature and photon-number squeezing

Quadrature squeezing and photon-number squeezing are not equivalent: quadrature squeezed states may have super-Poissonian photon statistics, and photon-number squeezed (sub-Poissonian) states are not necessarily quadrature squeezed.

Indeed, for the Fock state $|n\rangle$, which has zero variance in photon number, one has

$$\langle \Delta X^2 \rangle = \langle \Delta Y^2 \rangle = \frac{1}{4}(2n+1) \geq \frac{1}{4}. \tag{2.16}$$

On the other hand the photon-number variance for the quadrature squeezed states $|\alpha, \xi\rangle$ given by (2.13), is

$$\langle \Delta n^2 \rangle = |\alpha \cosh r_s - \alpha^* e^{i2\theta_s} \sinh r_s|^2 + 2\cosh^2 r_s \sinh^2 r_s. \tag{2.17}$$

Setting $\alpha = |\alpha| e^{i\phi}$, we find for $\theta_s = \phi + \frac{\pi}{2}$

$$\langle \Delta n^2 \rangle = |\alpha|^2 e^{2r_s} + 2\cosh^2 r_s \sinh^2 r_s. \tag{2.18}$$

This corresponds to a squeezing that is $\frac{\pi}{2}$ out of phase with the complex field amplitude (*phase squeezed state*), as shown in Fig. 2.7(a). In this situation, the state has increased

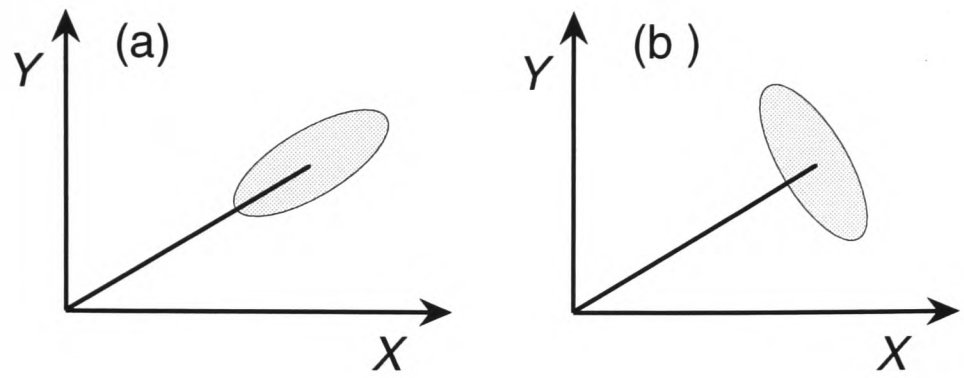

Figure 2.7: (a) Phase squeezed state. (b) Amplitude squeezed state.

amplitude fluctuations compared to a coherent state, and the photon-number statistics is super-Poissonian.

For $\theta_s = \phi$, on the other hand, we find

$$\langle \Delta n^2 \rangle = |\alpha|^2 e^{-2r_s} + 2\cosh^2 r_s \sinh^2 r_s. \tag{2.19}$$

The squeezing is now in phase with the complex amplitude (Fig. 2.7(b)), and the corresponding state is called an *amplitude squeezed state.* The first term on the right-hand side represents the contribution of the squeezed amplitude, while the second term is associated with the photon-number fluctuations in the corresponding squeezed vacuum state. For sufficiently large photon numbers, i.e. for $|\alpha|^2 \gg 2e^{2r_s}\cosh^2 r_s \sinh^2 r_s$, the first term dominates over the second, and one gets an amplitude squeezed state with sub-Poissonian photon distribution. Under these conditions, we can express the photon-number variance simply using the variance $\langle \Delta X'^2 \rangle < \frac{1}{4}$ in the squeezed quadrature:

$$\langle \Delta n^2 \rangle = |\alpha|^2 e^{-2r_s} = 4\langle n \rangle \langle \Delta X'^2 \rangle. \tag{2.20}$$

which exhibits sub-Poissonian statistics. Note that for $r_s = 1$, we find $\langle \Delta n^2 \rangle \approx 0.14\langle n \rangle$, i.e. a highly sub-Poissonian state.

For a fixed value of the average number of photons and as the squeeze parameter r_s is increased, one gets first a sub-Poissonian distribution and then, for sufficiently large r_s, a super-Poissonian distribution. This occurs when $\langle \Delta n^2 \rangle$ according to (2.19)

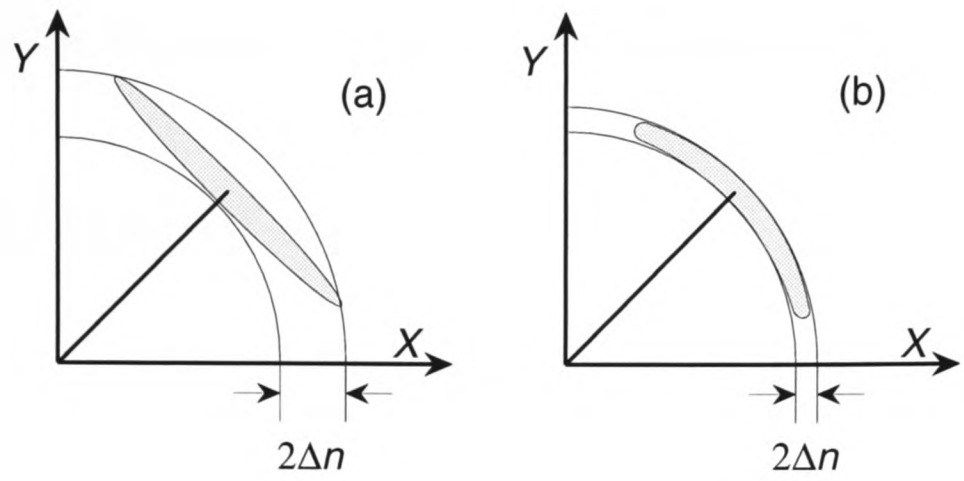

Figure 2.8: (a) Strongly amplitude squeezed state, exhibiting increased photon-number noise. (b) Example of a photon-number squeezed state created from a coherent state. Note that this "banana"-state is not quadrature squeezed.

becomes greater than $\langle n \rangle$ according to (2.15), i.e. when $(|\alpha|^2 e^{-2r_s} + 2\cosh^2 r_s \sinh^2 r_s) > |\alpha|^2 + \sinh^2 r_s$. The fact that the photon-number distribution becomes super-Poissonian can be understood heuristically from Fig. 2.8(a): as the uncertainty ellipse becomes more elongated, the range of intensities (squares of the distances to the origin) associated with the points within it becomes larger and larger, resulting in a wider photon-number distribution.

Fig. 2.8(b) on the other hand shows an example of a photon-number squeezed state created from a coherent state [26]. While the phase fluctuations are similar to Fig. 2.8(a), the curved uncertainty area leads to a strong reduction of photon-number noise. Note, however, that the bending of the uncertainty area leads to increased quadrature noise and eventually prevents this state from being quadrature squeezed.

There is some confusion in the literature about keeping apart the two states described in Fig. 2.8. The terms amplitude squeezed and photon-number squeezed are often used for any sort of sub-Poissonian light. For clarity we shall adopt the naming convention used in Fig 2.8 and use the term amplitude squeezed only for states of the type depicted in Fig. 2.8(a). Note, however, that for the moderate squeezing levels obtained to date, the

difference between the two states is marginal, and therefore only of conceptual interest.

2.3 Generation of squeezed light

2.3.1 Generation of quadrature squeezed light

Most of the experiments leading to the production of quadrature squeezed states are based on parametric processes in nonlinear optical media (nonlinear optical properties are discussed in detail in Chapter 3). The process of parametric amplification is easily illustrated by the example of a playground swing: The modulation of the length of the swing with a frequency twice its oscillation frequency leads to an amplification of one of the quadrature components, and the damping of the other. In nonlinear devices, it is the index of refraction that is modulated by a pump field in such a way that one of the quadrature components is amplified, and the other is damped, thus generating a quadrature squeezed state.

That a nonlinear medium is essential for obtaining quadrature squeezing can be seen from (2.10). The squeeze operator can be interpreted as corresponding to a time-evolution operator $\exp(-i\frac{\hat{H}t}{\hbar})$, generated by a Hamiltonian $\hat{H}$ quadratic in the field operators [27, 28]:

$$\hat{H} = \frac{\hbar}{2}(\eta^* \hat{a}^2 + \eta \hat{a}^{\dagger 2}), \tag{2.21}$$

with ξ in (2.10) being related to η through $\xi = i\eta t$. This Hamiltonian describes the creation or annihilation of pairs of identical photons. The pump field is described by a complex number, and its amplitude E_p is incorporated into the coupling constant. If $\eta = \chi^{(2)} E_p$, where $\chi^{(n)}$ is the nth-order susceptibility, one has a *degenerate parametric down-conversion* or *degenerate three-wave mixing* (D3WM): in this case, the frequency of the pump field is twice that of the signal field. If on the other hand $\eta = \chi^{(3)} E_p^2$, one

has *degenerate four-wave mixing* (D4WM) and the frequency of the pump field is equal to that of the signal field. While in the first case one photon of the pump field generates two photons of the signal field (hence the name "three-wave mixing"), in the second case one needs two photons of the pump field (thus yielding a four-wave mixing). Dissipation is disregarded here, but plays an important role in real experiments as any linear loss mechanism drives the photon statistics back towards a Poissonian.

More generally, the two photons of the signal field can belong to modes differing in propagation direction, polarisation or frequency, leading to the corresponding nondegenerate processes. If ω_s and ω_i are the frequencies of the two modes (conventionally called signal and idler beams), and ω_p is the frequency of the pump field, we have $\omega_p = \omega_s + \omega_i$ for 3WM, and $2\omega_p = \omega_s + \omega_i$ for 4WM. Conservation of photon momentum requires that $\vec{k}_p = \vec{k}_s + \vec{k}_i$ for 3WM and $2\vec{k}_p = \vec{k}_s + \vec{k}_i$ for 4WM (*phase-matching* conditions). This is a limiting factor in the first case, since then the frequency of the pump field is quite different from the frequency of the signal and idler waves. This usually results in quite different values for the nonlinear refractive index, so that the relation $\omega_p = \omega_s + \omega_i$ does not imply conservation of momentum for aligned beams: Fulfilling the phase-matching conditions requires particular nonlinear crystals and frequencies. This condition is easier to satisfy in the 4WM case, since then ω_p is close to ω_s and ω_i.

The first experimental observation of quadrature squeezing was made by Slusher *et al.* [1], using resonant 4WM in a sodium atomic beam, the interaction taking place in an optical cavity. They observed amplitude squeezing of 16% (0.8 dB) below the shot noise level.

In spite of the more difficult phase matching three-wave mixing has led to better results. Wu *et al.* [29] measured quadrature squeezing of 63% (-4 dB) below shot noise using a MgO doped $LiNbO_3$ crystal inside an optical parametric oscillator. Using a similar setup a noise suppression of up to 75% (-6 dB) has been observed [30].

More recently Fox *et al.* [8, 9] have demonstrated the possibility of using 4WM to generate quadrature squeezed light in semiconductors both in self-phase modulation and cross-phase modulation. The work presented in Chapter 6 represents the extension of this work to a different wavelength regime and a different crystal structure.

For a detailed description of other possible schemes for generating quadrature squeezed light see, for example, Bachor [17].

2.3.2 Generation of photon-number squeezed light

For the generation of photon-number squeezed light there exist two fundamentally different approaches. One option is to use nonlinear processes as in the case of quadrature squeezing. The other method is the direct conversion of sub-Poissonian electronic current statistics into the equivalent photon statistics using high-efficiency photoconverters.

The first demonstration of photon-number squeezed light by Short and Mandel in 1983 was based on the resonance fluorescence emission of a beam of sodium atoms [31]. Other nonlinear processes used to convert coherent beams into sub-Poissonian light include second-harmonic generation, where photon-number squeezing has been seen both in the fundamental [32] and in the frequency-doubled light [33], as well as parametric deamplification [34]. Only recently strong photon-number squeezing was obtained by spectrally filtering optical solitons [35, 36].

Photon-number squeezing by multi-photon absorption has been predicted as early as 1974 [14, 15]. The first experimental observations of this effect are discussed in Chapter 7.

The first to generate sub-Poissonian light by direct conversion were Teich and Saleh in 1985, using the Franck-Hertz effect in a vacuum tube with a space-charge limited current [2]. The concept of noise reduction by direct conversion using laser diodes was first proposed by Yamamoto *et al.* in 1986/7 [37, 38] and experimentally demonstrated by Machida and co-workers in 1987 [3]. In 1991 a noise suppression of 10 dB below shot noise

was achieved [39]. The first discovery of sub-Poissonian light emitted by light-emitting diodes was made by Tapster *et al.* in 1987 [4]. Since then the effect of noise reduction has been confirmed by several authors, demonstrating good agreement between experiment and theory (see e.g. [40, 41, 42, 43]). More recently Shinozaki *et al.* have shown 3 dB wideband squeezing in LEDs [44].

Squeezing by direct conversion in LEDs is discussed in more detail in Chapter 8.

Chapter 3

Midgap nonlinear optical properties of semiconductors

Contents

3.1 Introduction **26**

3.2 Constitutive relation **26**

3.3 Nearly degenerate four-wave mixing **28**

3.4 Stimulated Raman scattering **32**

3.5 Multi-photon absorption **35**

3.1 Introduction

From the discussion in the previous chapter it is apparent that optical nonlinearity is the key ingredient to the generation of squeezed light. After giving a brief introduction to the subject, the present chapter discusses the nonlinear processes relevant in the experiments presented in this thesis as well as the importance of these processes in semiconductors around midgap. For more details on nonlinear optics, see for example refs. [45, 46].

3.2 Constitutive relation

Nonlinear optical phenomena arise from a nonlinear response of a medium to an incident radiation.[1] The customary linear constitutive relation between the electric field $\mathbf{E}$ (magnetic field $\mathbf{H}$) and the electric polarisation $\mathbf{P}$ (magnetic polarisation $\mathbf{M}$) is no longer valid; it has to be modified into a more complex expression involving second, third, and higher powers of $\mathbf{E}(\mathbf{H})$. Since semiconductors are most often non-magnetic materials, the relevant constitutive relation to consider is the one correlating $\mathbf{P}$ and $\mathbf{E}$ which are functions of time t and spatial coordinates $\mathbf{r}$.

As in the linear case, nonlinear constitutive relations are conveniently written by taking the Fourier transform of any vector field $\mathbf{V}$

$$\mathbf{V}(\omega, \mathbf{k}) = \int \mathbf{V}(\mathbf{r}, t) \exp[i(\mathbf{kr} - \omega t)] d\mathbf{r} dt, \tag{3.1}$$

where ω is the angular frequency and $\mathbf{k}$ the wave vector. It is then possible to express the polarisation $\mathbf{P}(\omega_i, \mathbf{k}_i)$ as a power series of $\mathbf{E}(\omega_i, \mathbf{k}_i)$ thereby defining nth order optical susceptibilities $\chi^{(n)}(\omega, \mathbf{k})$. The $\mathbf{k}$-dependence of $\chi^{(n)}$ corresponds to the effects of spatial dispersion. These effects can generally be neglected, therefore allowing us to restrict ourselves to the electric dipole approximation. Under these conditions the constitutive

[1] For this section we follow a treatment given by Chemla and Jerphagnon [47]

relation for an incident radiation with frequency components ω_i, ω_j, is written as follows

$$\begin{aligned} P(\omega_i, \mathbf{k}_i) =& \epsilon_0 \chi^{(1)}(\omega_i) \cdot \mathbf{E}(\omega_i, \mathbf{k}_i) \\ &+ \epsilon_0 \sum_{j,l} \chi^{(2)}(-\omega_i; \omega_j, \omega_l) : \mathbf{E}(\omega_j, \mathbf{k}_j)\mathbf{E}(\omega_l, \mathbf{k}_l) \\ &+ \epsilon_0 \sum_{j,l,m} \chi^{(3)}(-\omega_i; \omega_j, \omega_l, \omega_m) \vdots \mathbf{E}(\omega_j, \mathbf{k}_j)\mathbf{E}(\omega_l, \mathbf{k}_l)\mathbf{E}(\omega_m, \mathbf{k}_m) + \cdots , \end{aligned} \tag{3.2}$$

where ϵ_0 is electric permeability of free space and $\chi^{(n)}$ an $(n+1)$ rank tensor. $\chi^{(1)}$ is the linear susceptibility related to the dielectric constant ϵ by $\epsilon = 1 + \chi^{(1)}$. Phenomena associated with $\chi^{(n)}$ become weaker as n becomes larger. High intensity laser fields are therefore required to observe these effects.

The number of individual processes associated with $\chi^{(n)}$ grows with increasing n. $\chi^{(1)}$ gives rise to the linear refraction through its real part and to linear absorption through its imaginary part. $\chi^{(2)}$ is responsible for second-harmonic generation ($\omega_j = \omega_l \rightarrow \omega_i = 2\omega_j$), optical rectification ($\omega_l = -\omega_j \rightarrow \omega_i = 0$), linear electro-optic effect or Pockels effect ($\omega_l \simeq 0 \rightarrow \omega_i \simeq \omega_j$), and various three-frequency processes such as difference frequency mixing, sum frequency generation, parametric amplification and parametric oscillation. To $\chi^{(3)}$ correspond third-harmonic generation ($\omega_j = \omega_l = \omega_m \rightarrow \omega_i = 3\omega_j$), the quadratic electro-optic effect or Kerr effect ($\omega_l = \omega_m \simeq 0 \rightarrow \omega_i \simeq \omega_j$), two-photon absorption ($\omega_j = -\omega_l = \omega_m \rightarrow \omega_i = \omega_j$, imaginary part) and the self-focussing of light ($\omega_j = -\omega_l = \omega_m \rightarrow \omega_i = \omega_j$, real part) as well as four-wave mixing (4WM) processes in general.

The susceptibilities $\chi^{(n)}$ obey crystallographic symmetry requirements. In particular $\chi^{(n)} \equiv 0$ for n even if there is a centre of symmetry. Since semiconductors most often belong to high symmetry point groups, the number of independent non-vanishing components of $\chi^{(n)}$ is small. For instance there is only one independent tensor element $\chi^{(2)}_{ikl}$ in zincblende structure materials (e.g. GaAs, AlGaAs).

All the experiments presented in this thesis are performed in symmetries where even-

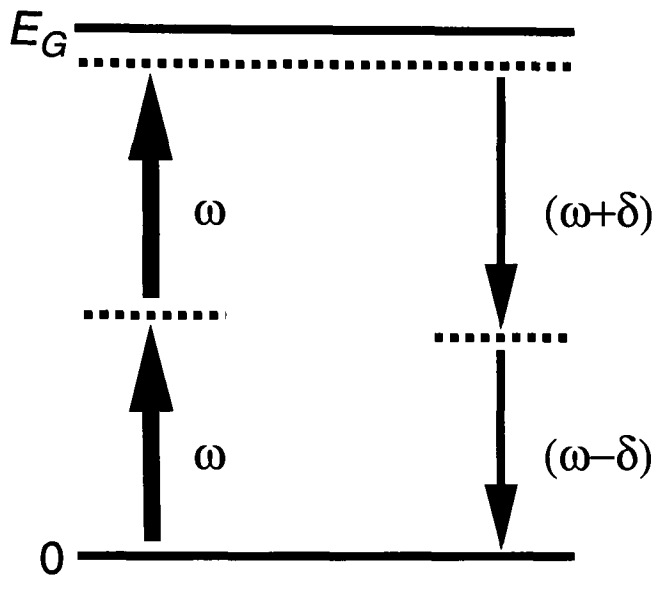

Figure 3.1: Nearly degenerate four-wave mixing (ND4WM) at photon energies just below half the bandgap E_G of a semiconductor. Two photons of frequency ω are absorbed and a pair of photons with frequencies $\omega + \delta$ and $\omega - \delta$ is created. The solid lines are real energy levels and the dotted lines represent virtual levels.

order nonlinear effects do not play a major role. We can therefore restrict our discussion to the relevant third- and fifth-order effects.

3.3 Nearly degenerate four-wave mixing

As discussed in §§ 2.3.1, four-wave mixing (4WM) provides a possibility for producing squeezed light through a Hamiltonian of the type (2.21). For the quadrature squeezing experiments presented in Chapter 6, we use so-called nearly degenerate 4WM (ND4WM) where squeezed light is generated at nearly the same frequency as the pump light (to within a small amount $\pm\delta$, where $\delta \ll \omega$) through the following Hamiltonian

$$\hat{H} = \frac{\hbar}{2}(\chi^{(3)*} E_p^{*2} \hat{a}_\omega \hat{a}_\omega + \chi^{(3)} E_p^2 \hat{a}^\dagger_{\omega+\delta} \hat{a}^\dagger_{\omega-\delta}), \tag{3.3}$$

where E_p is the amplitude of the classical pump field and $\hat{a}$ and $\hat{a}^\dagger$ are the photon annihilation and creation operators, respectively. The general form of $\chi^{(3)}$ for ND4WM is $\chi^{(3)}(-(\omega+\delta); \omega, -\omega, (\omega-\delta))$, although, due to $\delta \ll \omega$, its value will be very nearly the same as the degenerate susceptibility $\chi^{(3)}(-\omega; \omega, -\omega, \omega)$. Assessing this type of third-order susceptibility therefore provides important information on the suitability of a material for the production of squeezed light via ND4WM.

$\chi^{(3)}(-(\omega+\delta); \omega, -\omega, (\omega-\delta))$ mediates self-phase modulation (SPM) as well as cross-

phase modulation (XPM). In a semiconductor $\chi^{(3)}$ is resonantly enhanced at photon energies close to the bandgap energy E_G, and — to a lesser degree — at integer fractions of E_G. Working at photon energies just below the halfgap provides ideal circumstances for studying (N)D4WM-associated effects [48, 49, 50, 51], employing the resonance of $\chi^{(3)}(-(\omega+\delta);\omega,-\omega,(\omega-\delta))$ without the detrimental effects of two-photon absorption (cf. § 3.5).

3.3.1 Self-phase modulation

A direct consequence of the tensor element $\chi^{(3)}_{xxxx}(-(\omega+\delta);\omega,-\omega,(\omega-\delta))$ (often denoted χ_{xxxx}, the subscripts refer to the crystallographic directions along which the four photons involved are polarised) is the intensity dependent refractive index $n_2 = (2\pi/n_0)\mathrm{Re}\,[\chi_{xxxx}]$. The overall refractive index is then $n(I) = n_0 + n_2 I$. If pulsed light is used the intensity dependent refractive index translates into a time-dependent change of refractive index in the time domain. In the frequency domain this can be regarded as the generation of pairs of correlated photons on either side of each frequency component inside the pulse spectrum, resulting in a spectral broadening of the pulse, usually referred to as self-phase modulation (SPM). The output spectrum $I(\omega)$ of a pulse is given by the modulus squared of the Fourier transform $F(\omega)$ of the pulse amplitude [52]

$$F(\omega) \propto \int I(t)^{1/2} e^{i\Delta\Phi(t)} e^{-i(\omega-\omega_0)t} dt, \tag{3.4}$$

where $I(t)$ is the envelope function for the pulse intensity and ω_0 is the centre frequency of the pulse. $\Delta\Phi(t)$ represents the time-dependent nonlinear phase shift, which is related to the refractive index change $\Delta n(t)$ induced by the pulse according to

$$\Delta\Phi(t) = \frac{2\pi}{\lambda}\Delta n(t) L, \tag{3.5}$$

where λ is the wavelength and L the interaction length. In an ideal third-order material, the nonlinearity is described by an instantaneous response, and we write $\Delta n(t) = n_2 I(t)$.

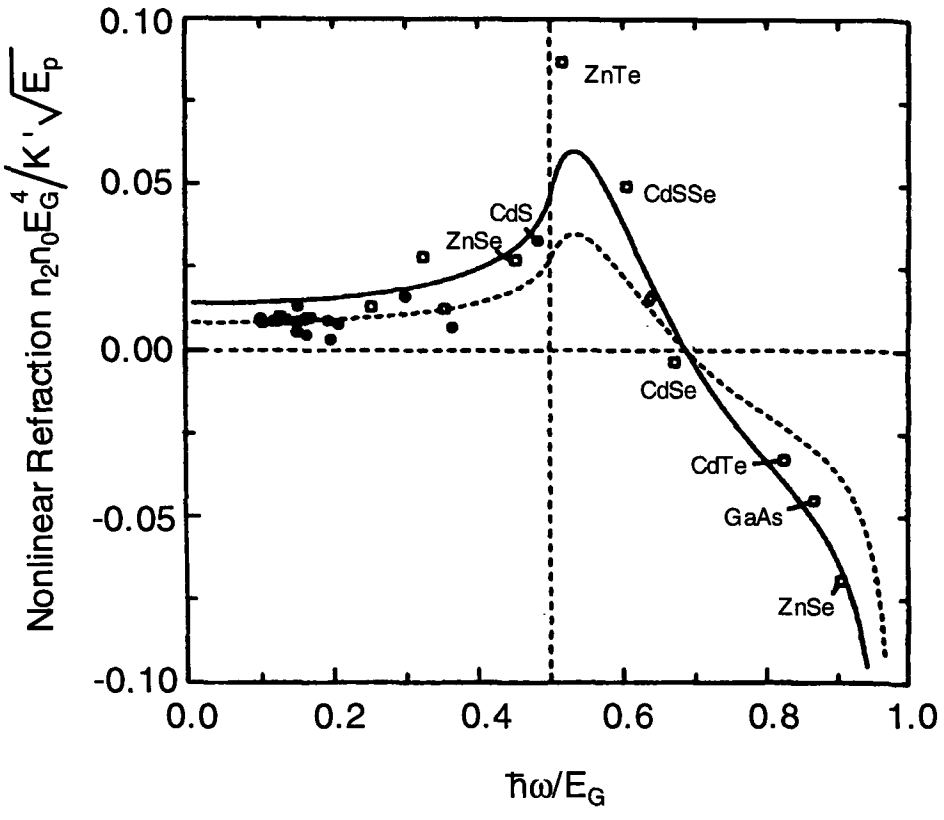

Figure 3.2: Dispersion of the nonlinear refractive index n_2. Data for n_2 are scaled as $n_2 n_0 E_G^4/K'\sqrt{E_p}$. The solid line is the $G_2(\hbar\omega/E_G)$ function derived in [49] with the theoretically predicted constant $K' = 0.94 \times 10^{-8}$. The dashed line corresponds to a fit to n_2 for wide-gap materials ($K' = 0.86 \times 10^{-8}$). *After Sheik-Bahae* et al. *[49]*

In this situation the spectrum broadens symmetrically about the centre frequency. In a non-ideal third-order material the response is not instantaneous, leading to a temporal asymmetry which in turn causes a spectral asymmetry. In addition, competing nonlinear processes, such as the stimulated Raman effect, free-carrier scattering and multi-photon absorption can alter the spectral profile at the same time (cf. § 3.4 and 3.5).

Because of the link between the nonlinear refractive index n_2 and $\chi^{(3)}$, there is a direct connection between the squeezing achievable through (3.3) and the nonlinear phase shift $\Delta\Phi$. When the pump intensity is high enough to generate a substantial amount of squeezing, it is also high enough to cause the pump to experience a nonlinear phase shift of the order of π [53]. In fact, for an ideal case with exact phase matching the squeeze parameter r_s as defined in (2.12) is exactly equal to $\Delta\Phi$ [54]. Investigating $\Delta\Phi$ is therefore a useful tool to study the potential suitability of a material for $\chi^{(3)}$ squeezing.

The wavelength dependence of the nonlinear refractive index n_2 in semiconductors has been studied extensively. Sheik-Bahae *et al.* [48, 49] have studied n_2 as a function of

$\hbar\omega/E_G$, i.e. the photon energy to bandgap ratio. Using a Kramers-Kronig transformation approach relating $\mathrm{Re}\chi^{(3)}$ to $\mathrm{Im}\chi^{(3)}$ in a two-band model, they find a general scaled form for n_2 given by

$$n_2 \text{ (esu)} = K' \frac{\sqrt{E_p}}{n_0 E_G^4} G_2(\hbar\omega/E_G). \tag{3.6}$$

Here K' is a constant and $E_p \simeq 21$ eV (related to the Kane momentum parameter[2]) is nearly material independent for a wide variety of semiconductors [56]. Note also the E_G^{-4} dependence for the magnitude of n_2, corresponding to the scaling predicted by Wherrett [57]. The function $G_2(\hbar\omega/E_G)$ contains the actual dispersion information and is compared to measured data in Fig. 3.2. We see broad resonances of n_2 both near E_G and $E_G/2$. Using photon energies at $E_G/2$ has the significant advantage of avoiding large linear absorption losses. Because of the width of the n_2-resonance at halfgap, it is even possible to work slightly below halfgap, where two-photon absorption vanishes rapidly (cf. § 3.5).

3.3.2 Cross-phase modulation

An intense pump field in a nonlinear crystal cannot only modulate itself by SPM, but can also influence waves of the same frequency but with orthogonal polarisation through cross-phase modulation (XPM). This process is mediated by the off-diagonal elements of $\chi^{(3)}_{ijkl}(-(\omega+\delta);\omega,-\omega,(\omega-\delta))$, i.e. χ_{xxyy}, χ_{xyxy}, and χ_{xyyx}. The effective nonlinear susceptibility for four-wave mixing is [58]

$$\begin{aligned}\chi^{(3)}_{\text{eff}} =& \chi_{xxyy}(\hat{\mathbf{a}}^* \cdot \hat{\mathbf{b}})(\hat{\mathbf{c}} \cdot \hat{\mathbf{d}}) + \chi_{xyyx}(\hat{\mathbf{a}} \cdot \hat{\mathbf{d}})(\hat{\mathbf{b}} \cdot \hat{\mathbf{c}}) + \chi_{xxyy}(\hat{\mathbf{a}}^* \cdot \hat{\mathbf{c}})(\hat{\mathbf{b}} \cdot \hat{\mathbf{d}}) \\ &+ \sigma\chi_{xxxx} \sum_i a_i^* b_i c_i d_i,\end{aligned} \tag{3.7}$$

where σ is the anisotropy parameter given by

$$\sigma = \frac{\chi_{xxxx} - (\chi_{xxyy} + \chi_{xyxy} + \chi_{xyyx})}{\chi_{xxxx}}. \tag{3.8}$$

[2] $E_p = 2P^2m/\hbar^2$, where P is the Kane momentum parameter and m the electron mass [55].

$\hat{\mathbf{a}}, \hat{\mathbf{b}}, \hat{\mathbf{c}}$, and $\hat{\mathbf{d}}$ are the polarisation vectors of the four photons involved, and a_i, b_i, c_i, and d_i are their projections along the principal crystallographic axes. In the case of linear polarisations, and for the signal and idler photons polarised orthogonally to the pump, we have $\hat{\mathbf{a}} \cdot \hat{\mathbf{b}} = \hat{\mathbf{c}} \cdot \hat{\mathbf{d}} = 1$ and $\hat{\mathbf{a}} \cdot \hat{\mathbf{c}} = \hat{\mathbf{a}} \cdot \hat{\mathbf{d}} = 0$. The second and third term on the right hand side of (3.7) vanish in this case.

For the semiconductors treated in this thesis, $\sigma \leq 0$ and hence the maximum XPM susceptibility $\chi^{(3)}_{\text{eff}}$ for the orthogonal case is χ_{xxyy}.[3] This maximum can be reached by choosing an appropriate geometry. The magnitude of χ_{xxyy} is equal to $\frac{1}{3}\chi_{xxxx}$ in the isotropic case, but can become slightly different in a non-isotropic case, depending on the particularities of a given semiconductor. The relation, however, provides a first approximation to the link between XPM and SPM. Values obtained for n_2 and $\Delta\Phi$ by SPM (discussed in the previous subsection) can therefore also serve as a basis to estimate the amount of XPM.

Note that in order to achieve parametric amplification (and in our case: squeezing) by XPM, phase matching is crucial. Linear as well as induced birefringence can bring the pump wave out of phase with the signal and idler waves, such as to prevent the parametric process.

3.4 Stimulated Raman scattering

As mentioned in §§ 3.3.1, stimulated Raman scattering can modify the spectrum of a light pulse, but it has also been found to act as a noise source detrimental to the production of squeezed light [61, 62].

Raman scattering is a two-photon process in which one photon at $\omega_1(\mathbf{k}_1)$ is absorbed and one photon at $\omega_2(\mathbf{k}_2)$ is emitted, while the material makes a transition from an initial state $|i\rangle$ to a final state $|f\rangle$, as shown in Fig. 3.3. Energy conservation requires

[3] For zincblende structures $\sigma < 0$ near $E_G/2$ [59, 60, 58] and for hexagonal structures $\sigma \equiv 0$ [46].

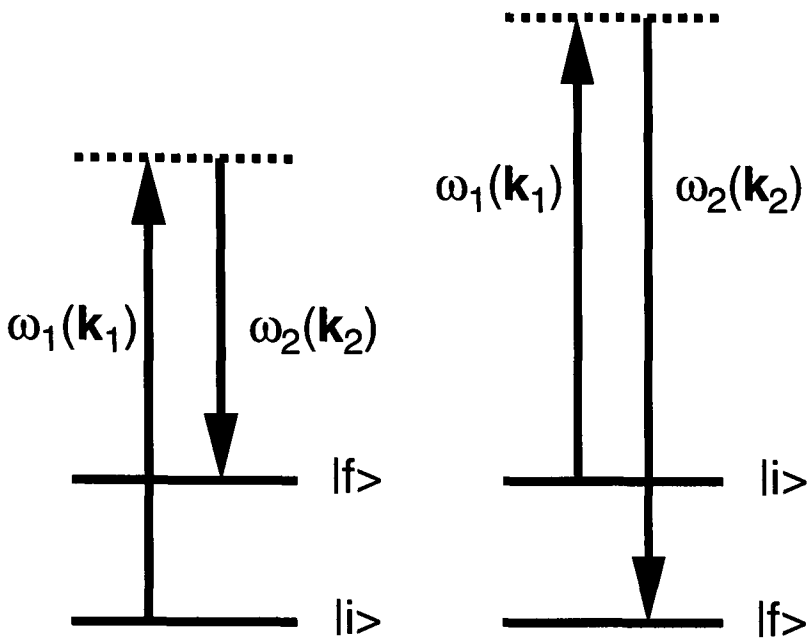

Figure 3.3: Schematic of Raman scattering from an initial state $|i\rangle$ to a final state $|f\rangle$ for the Stokes case (left) and the anti-Stokes case (right).

$\hbar(\omega_1 - \omega_2) = \mathbb{E}_f - \mathbb{E}_i \equiv \hbar\omega_{fi}$, which is the energy difference between the final and the initial states. Stokes and anti-Stokes scattering corresponds to $\omega_{fi} > 0$ and $\omega_{fi} < 0$, respectively.

The stimulated process is schematically represented in Fig. 3.4. In this case a light wave at frequency ω_s is incident on the material system simultaneously with a light wave at ω_p. A quantum $\hbar\omega_s$ is added to the wave at ω_s, which consequently becomes amplified, while the incident light beam loses a quantum $\hbar\omega_p$ and the material system is excited by a quantum $\hbar\omega_{fi}$. In the presence of N_s quanta of excitation at ω_s the probability of an additional transition to $N_s + 1$ quanta is enhanced by a factor of $N_s + 1$. This relates the stimulated to the spontaneous process.

In the Stokes case the process is mediated by a negative imaginary part of the third-order nonlinear susceptibility $\chi^{(3)}(-\omega_s; \omega_p, -\omega_p, \omega_s)$, which is often denoted $\chi''_{Raman} < 0$. The amplitude E_s at the Stokes frequency obeys the equation

$$\frac{dE_s}{dz} = -2\pi(\omega_s/n_s c)\chi''_{Raman}|E_p|^2 E_s. \tag{3.9}$$

Since $\chi''_{Raman} < 0$, there will be exponential growth of the intensity I_s of the Stokes wave

$$I_s(l) = I_s(0)e^{g_s l}, \tag{3.10}$$

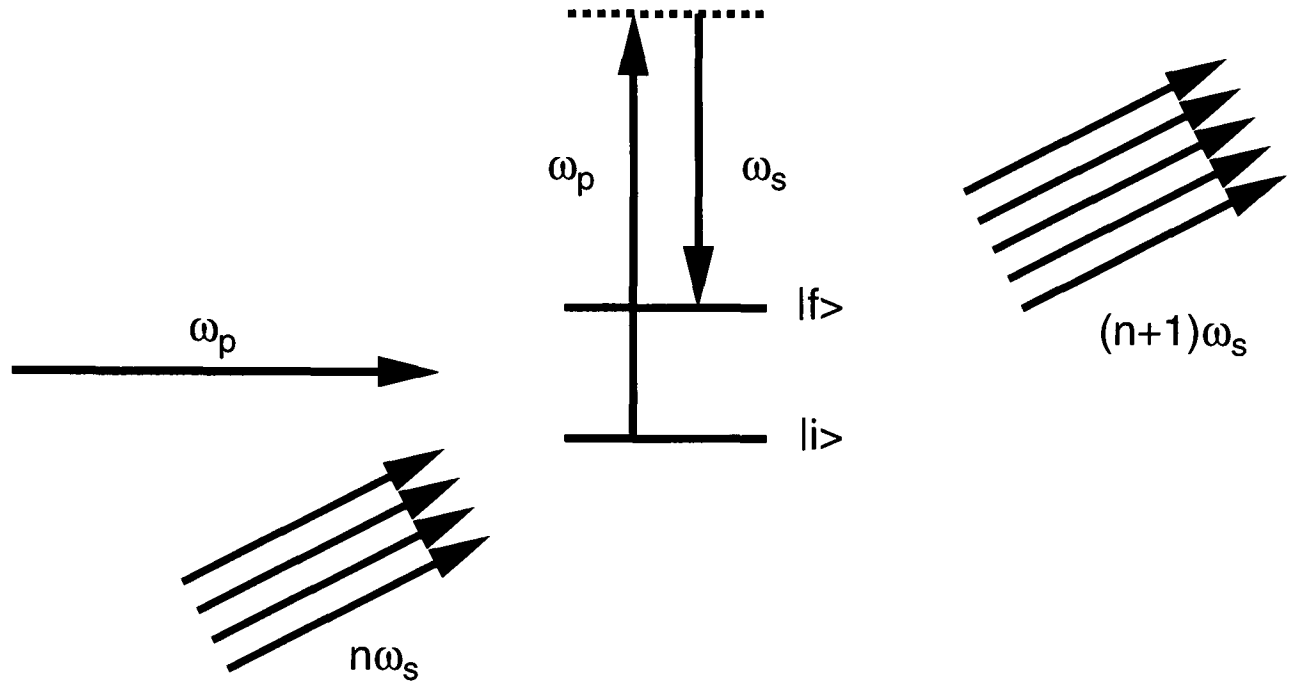

Figure 3.4: Schematic of stimulated Raman scattering (for the Stokes case).

where the Raman gain coefficient g_s is given by

$$g_s = 4\pi(\omega_s/n_s c)(-\chi''_{Raman})|E_p|^2. \tag{3.11}$$

At the same time there is an exponential loss at the pump frequency, described by

$$\frac{dE_p}{dz} = -2\pi(\omega_p/n_p c)(-\chi''_{Raman})|E_s|^2 E_p. \tag{3.12}$$

This is a consequence of the relationship

$$\chi^{(3)}(-\omega_s;\omega_p,-\omega_p,\omega_s) = \chi^{(3)*}(-\omega_p;\omega_s,-\omega_s,\omega_p), \tag{3.13}$$

which expresses the fact that the imaginary part of the susceptibility changes sign on the interchange of the frequencies ω_p and ω_s. The gain at ω_s is connected with a loss at ω_p, in agreement with the considerations of the quantum process described above.

For the same reasons one expects an exponential loss at the anti-Stokes frequency ω_{as}. One finds that $\mathrm{Im}\left[\chi^{(3)}(-\omega_{as};\omega_p,-\omega_p,\omega_{as})\right] > 0$. In fact, this quantity is nearly equal to $\mathrm{Im}\left[\chi^{(3)}(-\omega_p;\omega_s,-\omega_s,\omega_p)\right]$.

Apart from the individual Stokes and anti-Stokes processes there is also a coupling between the two. A third-order nonlinear polarisation at the anti-Stokes frequency

$\omega_{as} = 2\omega_p - \omega_s$ can be induced in the medium through mixing of the pump wave at ω_p and the Stokes wave at ω_s via the Raman resonance at $\omega_p - \omega_s = \omega_{as} - \omega_p$, i.e. $\chi^{(3)}(-\omega_s; \omega_p, -\omega_{as}, \omega_p)$. This is especially important near the phase matching condition for which $\Delta\mathbf{k} = \mathbf{k}_s + \mathbf{k}_{as} - 2\mathbf{k}_p$ is nearly zero. Solving the coupled wave equations [63, 64] shows that there can be considerable gain at the anti-Stokes frequency unlike in the uncoupled case far away from phase matching.

In the context of this thesis it is important to note that by using femtosecond pulses the bandwidth of the photon energies in the pulses can easily reach the LO-phonon energy in a semiconductor. Therefore stimulated Raman scattering can be seen in a single beam of ultrashort pulses.

3.5 Multi-photon absorption

At high optical intensity levels, nonlinear absorption processes become significant. These are especially interesting in a squeezing context, as they can both generate and destroy squeezed light.

In general, the propagation equation for an intensity $I(z)$ of a light beam travelling through a nonlinear medium is given by:

$$\frac{dI}{dz} = -\left[\alpha_1(\lambda) + \alpha_2(\lambda)I + \alpha_3(\lambda)I^2 + \cdots\right] I, \tag{3.14}$$

where α_1, α_2 and α_3 represent the coefficients for linear absorption, two-photon absorption (2PA) and three-photon absorption (3PA), respectively. These coefficients are directly linked to a positive imaginary part of the susceptibility tensor. A k-photon

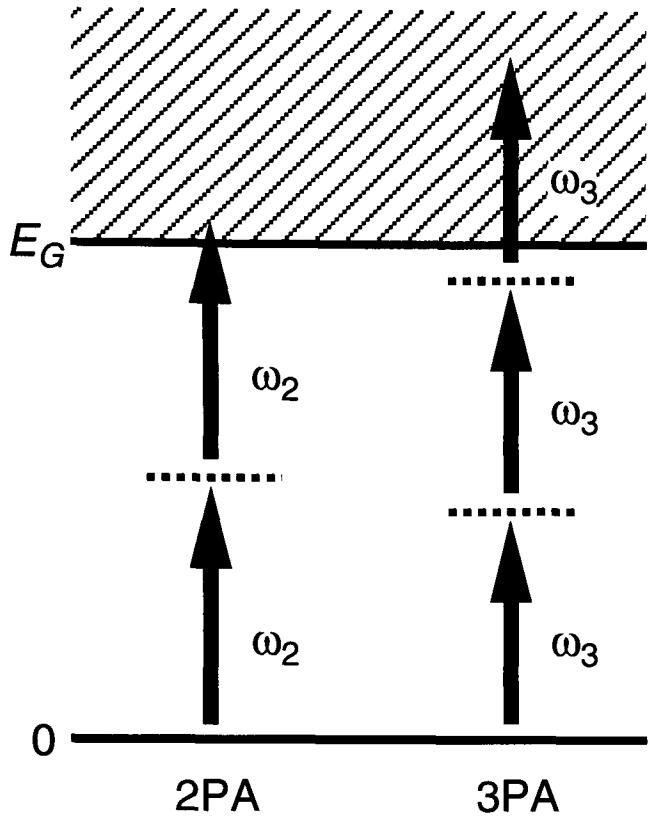

Figure 3.5: Schematic of two-photon absorption (2PA) and three-photon absorption (3PA) at photon energies near half the bandgap energy E_G of a semiconductor.

absorption coefficient α_k is proportional to Im $\chi^{(2k-1)}(-\omega; -\omega, \ldots, -\omega, \omega, \ldots, \omega)$, i.e.,

$$\begin{aligned} \alpha_1 &\propto \text{Im } \chi^{(1)}(-\omega; \omega), \\ \alpha_2 &\propto \text{Im } \chi^{(3)}(-\omega; -\omega, \omega, \omega), \\ \alpha_3 &\propto \text{Im } \chi^{(5)}(-\omega; -\omega, -\omega, \omega, \omega, \omega) \\ &\vdots \end{aligned} \tag{3.15}$$

These are the susceptibilities involved in degenerate multi-photon absorption (MPA), the relations are analogous for the non-degenerate case.

Fig. 3.5 shows a schematic of the 2PA and the 3PA processes at photon energies around half the bandgap energy of a semiconductor. The scaling rules of multi-photon absorption in semiconductors have been investigated in detail by Wherrett [57]. He finds that regardless of the value of k, the k-photon absorption coefficient α_k can be expressed by

$$\alpha_k = C_k F_k(k\hbar\omega/E_G)\hbar^{k-1}\frac{P^{2k-3}}{n_0^k E_G^{4k-5}}, \tag{3.16}$$

where C_k is a dimensionless factor, as is the function $F_k(k\hbar\omega/E_G)$ and P is the Kane momentum parameter [55]. The functional dependence on the radiation frequency is

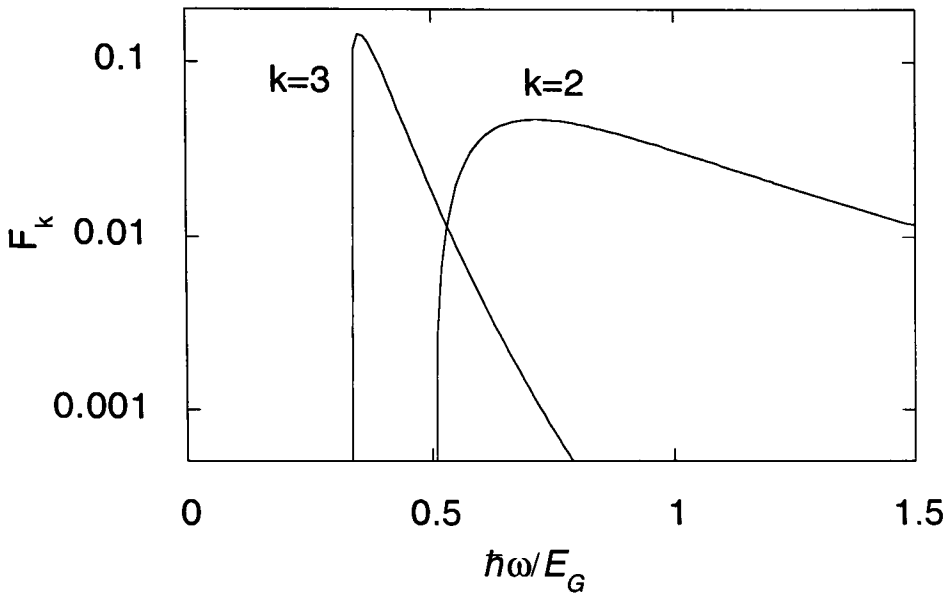

Figure 3.6: Functional dependence F_k of 2PA ($k = 2$) and 3PA ($k = 3$) on the photon energy to bandgap ratio $\hbar\omega/E_G$.

contained in $F_k(k\hbar\omega/E_G)$. For odd k-values, it becomes:

$$F_k(k\hbar\omega/E_G) = \frac{(k\hbar\omega/E_G - 1)^{1/2}}{(k\hbar\omega/E_G)^{4k-3}}, \tag{3.17}$$

whereas for even k-values, it is

$$F_k(k\hbar\omega/E_G) = \frac{(k\hbar\omega/E_G - 1)^{3/2}}{(k\hbar\omega/E_G)^{4k-3}}, \tag{3.18}$$

Fig. 3.6 shows the evaluation of (3.18) for F_2 and F_3. The plot illustrates why the midgap region is of particular interest. In the case where MPA is an unwanted effect a minimum can be found in the region just below the 2PA edge, i.e. just below halfgap. Note that the 2PA vanishes very sharply at halfgap, whereas the resonance of the nonlinear refractive index extends significantly below halfgap, as discussed in § 3.3.

If MPA is the desired effect (cf. Chapter 7), tuning the photon energy from below halfgap to above halfgap makes it possible to effectively select 2PA or 3PA as the dominant absorption process.

Chapter 4

Experimental apparatus and techniques

Contents

4.1 Laser system 39

4.2 Interferometric autocorrelator 42

4.3 Detection systems 43

In this chapter we describe the pulsed laser system used for most of the work in this thesis, the autocorrelator used to characterise the pulses, as well as the detection systems for squeezed light employed in the different experiments. The actual experimental setups are discussed in the corresponding chapters.

4.1 Laser system

The ultrashort pulses used in the experiments described in Chapters 5, 6, and 7 were all generated in an optical parametric oscillator (OPO) driven by a modelocked Ti:sapphire laser which was itself pumped by an argon ion laser.

4.1.1 Argon ion laser

The main pump laser for the whole system was a Spectra-Physics BeamLok 2080 Ar^+ laser. It has several spectral lines in the wavelength region from 450 nm to 514.5 nm, the line at 514.5 nm being the strongest. The laser operated in continuous wave (cw) mode. The typical output power was about 12 W in all-line operation.

4.1.2 Ti:sapphire laser

The Ti:sapphire laser is one of the most widely used short-pulse solid state lasers. The model used for this work was a Spectra-Physics Tsunami. The active medium is a 3-cm-rod of sapphire (Al_2O_3) doped with 0.05 % of Titanium such that Ti^{3+} ions replace some of the Al^{3+} ions. The laser is modelocked by a combination of passive modelocking based on Kerr lensing, and active modelocking by an acoustooptic modulator. It emits pulses of about 80 fs duration at a repetition rate of 81 MHz. The average output power is about 2 W. The tuning range is 720 nm to 960 nm. In order to pump the OPO the laser was operated at 810 nm. For a more detailed description see ref. [65].

4.1.3 Optical parametric oscillator

In order to access wavelengths beyond the range of Ti:sapphire an optical parametric oscillator (OPO) was used. The OPO operates on a very different principle to that of a laser. A laser derives its gain from stimulated emission generated by transitions between different atomic or molecular states. These transitions have inherent linewidths that govern the maximum tuning range of the laser. In contrast, an OPO derives its gain from a nonlinear frequency conversion process which can provide wavelength tunability greater than 1000 nm.

In an OPO, wavelength conversion is achieved through parametric down conversion in a nonlinear optical crystal. An input pump photon (ω_p) is split into lower energy signal (ω_s) and idler (ω_i) photons, such that energy is conserved, i.e.,

$$\omega_p = \omega_s + \omega_i, \qquad (\text{and } \omega_s > \omega_i) \tag{4.1}$$

or in terms of wavelength,

$$\frac{1}{\lambda_p} = \frac{1}{\lambda_s} + \frac{1}{\lambda_i}. \tag{4.2}$$

Momentum conservation,

$$k_p = k_s + k_i, \tag{4.3}$$

is achieved by using a birefringent nonlinear crystal and by satisfying the phase matching condition,

$$n_p\omega_p = n_s\omega_s + n_i\omega_i, \tag{4.4}$$

where n is the refractive index.

The process requires crystals with a high second-order nonlinear susceptibility, and can be viewed as the inverse of second-harmonic generation (SHG) or sum frequency mixing. Parametric down conversion has much lower efficiency, however, since both signal

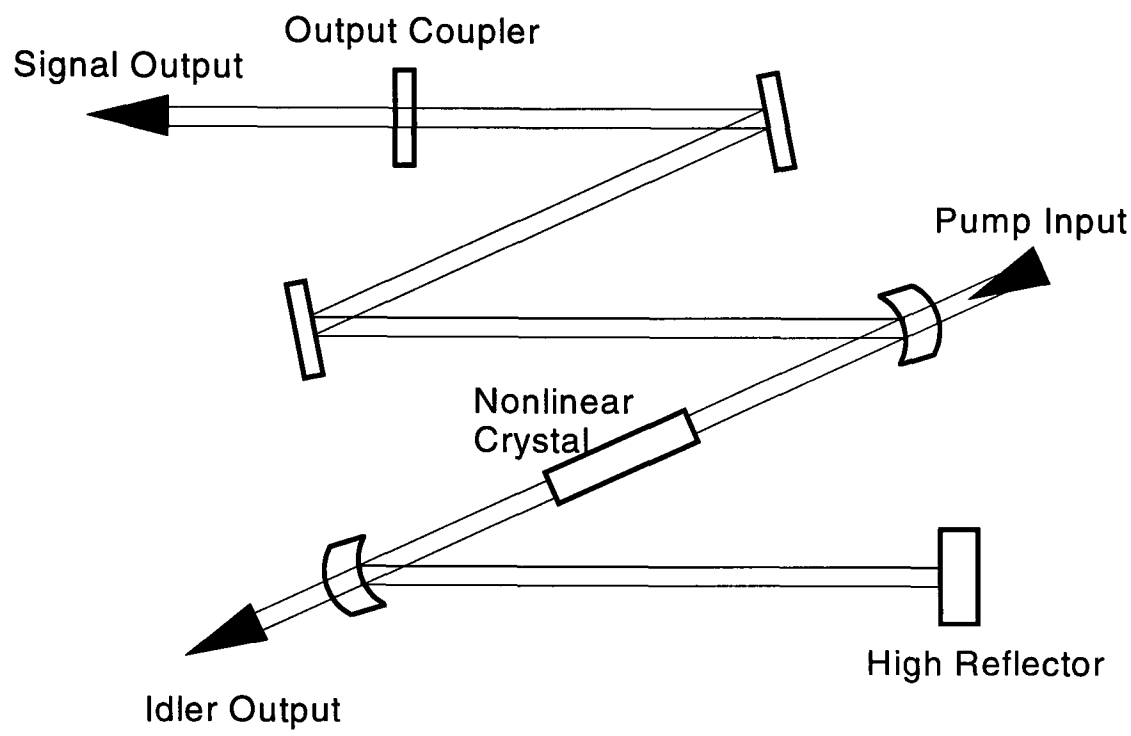

Figure 4.1: Typical configuration for an optical parametric oscillator.

and idler waves (as opposed to only the 2ω wave in SHG) must be built up. Therefore, high conversion efficiencies in OPOs are generally attained by resonating the signal wave (Fig. 4.1). Since gain is only available in the nonlinear crystal when the pump pulse is present, for femtosecond OPOs it is necessary to use a synchronous pumping scheme, i.e. to match the cavity length of the OPO to that of the Ti:sapphire pump laser, so that the signal and pump pulses are always present in the nonlinear crystal at the same time.

The pioneering work [66] on femtosecond synchronously pumped optical parametric oscillator systems was done using angle-tuned potassium titanyl phosphate (KTP) as the nonlinear gain medium. More recently, other groups have demonstrated Ti:sapphire-pumped systems [67, 68, 69].

The OPO used here was a Spectra-Physics Opal. Its gain medium is a 90° non-critically phase-matched, temperature-tuned LBO (LiB_3O_5, lithium triborate) nonlinear crystal. The cavity is actively stabilised to maintain the synchronous pumping. With the mirror set in use the signal wave is tunable from 1.35 μm to 1.6 μm, emitting pulses of durations between 70 and 160 fs, depending on the wavelength, at a repetition rate

of 81 MHz. The pulses emitted are found to be best described with a sech^2 intensity profile. In standard operation they were found to be transform limited according to the expected sech^2 time-bandwidth product $\Delta\nu\Delta\tau = 0.3148$ [70], e.g. a 100 fs pulse has a bandwidth of ≈ 25 nm. The average output power varies between 200 mW and 400 mW depending on the wavelength.

Measurements of the linearity of the noise versus power as well as comparison with a known shot noise limited source (a blackbody emitter) showed the OPO to produce shot noise limited light when properly aligned.

4.2 Interferometric autocorrelator

In the femtosecond range direct photoelectric detection of the pulse duration is not possible. Therefore a scanning interferometric autocorrelator was built to measure the pulse-length and to characterise the pulses in the temporal domain.

In the autocorrelation technique the optical pulses are used to measure themselves. The optical configuration is essentially that of a Michelson interferometer. The incoming pulse is split into two pulses of equal intensity and an adjustable delay is imparted to one. The two beams are then recombined in a nonlinear crystal for second-harmonic generation. The frequency-doubled light is subsequently detected with a photodetector. By adjusting the delay τ of one pulse with respect to the other, the signal $S(\tau)$ of the second-harmonic generation

$$S(\tau) \propto \int_{-\infty}^{+\infty} \left| [E(t) + E(t+\tau)]^2 \right|^2 dt. \tag{4.5}$$

can be recorded. This signal is equivalent to the second-order correlation function which allows the determination of the pulse duration and further characterisation of the pulse in the temporal domain (cf. Chapter 5), namely concerning the nonlinear chirp. Note that for laser pulses with a sech^2-intensity profile the ratio between the FWHM of the

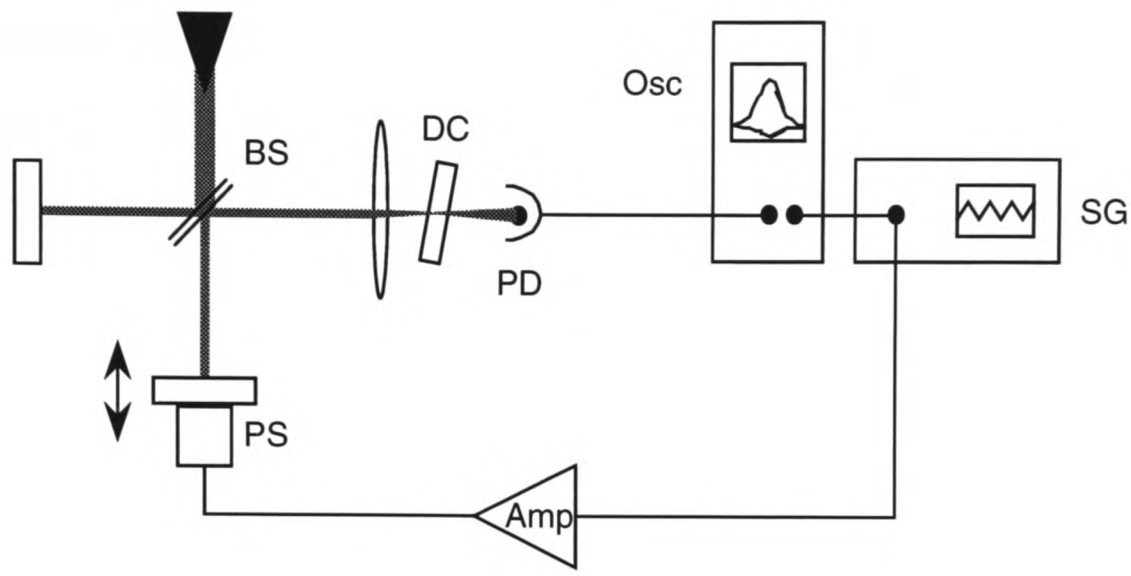

Figure 4.2: Schematic of the autocorrelator. BS, low-dispersion 50:50 beam splitter; PS, phase shifter; DC, doubling crystal; PD, Si-avalanche photodiode; Osc, digital oscilloscope; SG, signal generator; Amp, amplifier.

autocorrelation envelope and the actual pulse width is 1.55.

Fig. 4.2 shows the configuration of the interferometric autocorrelator. Because of the large spectral width of femtosecond pulses a low-dispersion beam splitter had to be used. The amplified triangular signal of a signal generator was used to drive the phase-shifter, consisting of a mirror mounted on a small loudspeaker. Its maximum travel was about 0.5 mm and it was typically operated at a few hundred Hz. The second-harmonic generation was done in a AR-coated BBO (BaB_2O_4, Beta Barium Borate) frequency-doubling crystal.[1] The frequency doubled light was subsequently detected in an Si-avalanche photodiode and the signal was stored on a digital oscilloscope.

4.3 Detection systems

The measurement of the quantum noise of light plays a crucial role in any experiment involving squeezed light. The most straightforward way to do this, is direct detection

[1] In the meantime we have modified the system to work with direct two-photon absorption in the photodetector (cf. [71]) which is sufficient for most applications and aligned more easily.

using a photodetector. Common photodetectors such as *p-i-n* photodiodes and photomultiplier tubes measure the total photon number. This is due to the fact that such devices produce an electrical current which effectively "counts" internal low energy to high energy transitions, each transition corresponding to the absorption of one photon. The absorbed photons have a probability, given by the internal quantum efficiency of the photodetector, of generating detector state transitions which are "counted" by the device. The current produced by a detector with constant quantum efficiency is thus proportional to the number of photons arriving at the detector per unit time [17]. After correction for losses, the current fluctuations therefore are a direct measure of the fluctuations in the number of photon arrivals per unit time.

For the photon-number squeezing experiments in LEDs described in Chapter 8 the noise was detected directly with a single photodiode, the current was then amplified and analysed using an rf spectrum analyser. For the squeezing measurements in Chapters 6 and 7, balanced detection systems were used to facilitate shot noise calibration and to eliminate classical noise. In balanced detection the squeezed beam is divided using a 50/50 beam splitter (which in our case is composed of a $\lambda/2$-plate and a polarising beam splitter) and directed onto two matched photodiodes. The two systems used for the detection of the quadrature squeezing in Chapter 6 and for the photon-number squeezing in Chapter 7 are now discussed in more detail.

4.3.1 Quadrature squeezing detection

For the detection of the quadrature squeezing in Chapter 6 a balanced homodyne detection system was used, as first proposed by Yuen and Shapiro [72] and Walls and Zoller [73]. In homodyne detection the signal to be detected is mixed with a strong coherent, and therefore shot noise limited signal, called the *local oscillator* (LO).

Fig. 4.3 shows the schematic arrangement of a homodyne detector. The field to

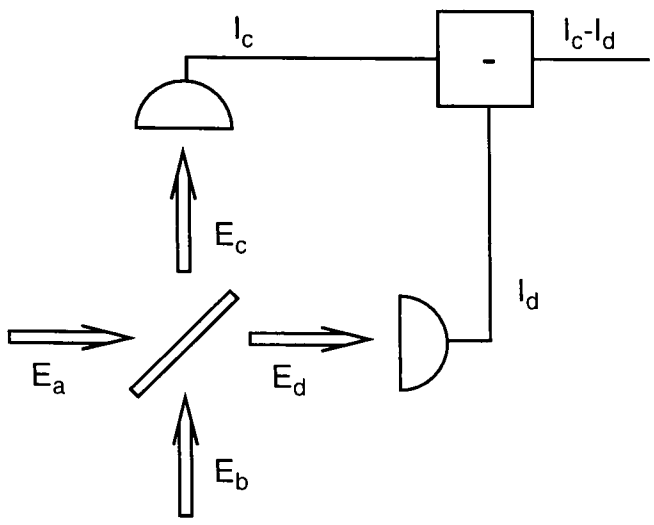

Figure 4.3: Schematic arrangement of a homodyne detector.

be measured (complex amplitude E_a) is incident onto a beam splitter, together with a coherent field (complex amplitude E_b) with the same frequency. Subsequently the intensities of the two beams emerging from the beam splitter (complex amplitudes E_c and E_d) are measured. The detection is said to be balanced when the beam splitter transmits 50% of the incident light.

Let r and t be the amplitude reflection and transmission coefficients of the beam splitter, respectively. We have

$$E_c = rE_a - tE_b, \qquad E_d = tE_a + rE_b, \tag{4.6}$$

or in matrix form,

$$\begin{pmatrix} E_c \\ E_d \end{pmatrix} = \begin{pmatrix} r & -t \\ t & r \end{pmatrix} \begin{pmatrix} E_a \\ E_b \end{pmatrix}. \tag{4.7}$$

Energy conservation implies that

$$|E_c|^2 + |E_d|^2 = |E_a|^2 + |E_b|^2. \tag{4.8}$$

From (4.7) and (4.8), we find

$$= 1, \qquad r^*t - rt^* = 0. \tag{4.9}$$

For l and equal to $1/\sqrt{2}$. Normalising the

intensity to the photon number, and introducing the annihilation operators through

$$E_a \rightarrow \hat{a}, E_b \rightarrow \hat{b},$$

$$E_c \rightarrow \hat{c}, E_d \rightarrow \hat{d},$$

we find

$$\hat{c} = \frac{1}{\sqrt{2}}(\hat{a} - \hat{b}),$$
$$\hat{d} = \frac{1}{\sqrt{2}}(\hat{a} + \hat{b}).$$

The difference in the intensities of the fields E_d and E_c is then given by

$$I = \hat{d}^\dagger\hat{d} - \hat{c}^\dagger\hat{c} = \hat{a}^\dagger\hat{b} + \hat{b}^\dagger\hat{a}. \tag{4.10}$$

Assuming that the field E_b can be described classically (as would be the case for a coherent state with large average photon number), we can replace $\hat{b}$ by $\beta = Be^{-i(\omega t+\theta)}$ and use $\hat{a} = \hat{a}_0 e^{-i(\omega t+\theta)}$, so that (4.10) becomes

$$I = B(\hat{a}_0 e^{i\theta} + \hat{a}_0^\dagger e^{-i\theta}). \tag{4.11}$$

This equation shows that the difference in intensity, measured by the method of homodyne detection, is directly proportional to the quadrature $\hat{X}(\theta)$ of the field E_a, defined by

$$\hat{X}(\theta) = \frac{1}{\sqrt{2}}(\hat{a}_0 e^{i\theta} + \hat{a}_0^\dagger e^{-i\theta}). \tag{4.12}$$

Therefore, by detecting the difference in intensity as the phase of the local oscillator E_b is changed, one can measure an arbitrary quadrature of the field E_a. More importantly for our purposes, the noise of the difference intensity I is proportional to the noise in the quadrature $\hat{X}(\theta)$, i.e. $\Delta X^2(\theta)$. By measuring $\Delta X^2(\theta)$ as a function of the LO phase θ we can deduce the uncertainty ellipse of the signal mode E_a, corresponding to a squeezed vacuum in our case. The shot noise level can be obtained by blocking the signal port.

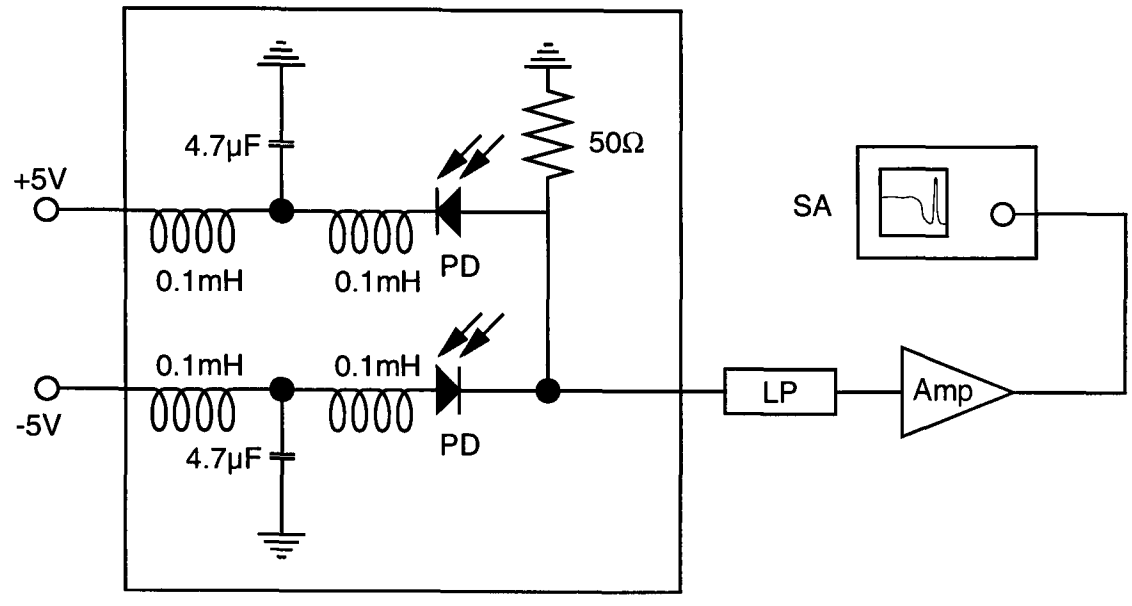

Figure 4.4: Circuit diagram of the balanced detection system used for quadrature squeezing. PD, InGaAs-photodetector; LP, 50 MHz low-pass filter; Amp, low-noise amplifier; SA, spectrum analyser.

Fig. 4.4 shows the circuit diagram of the detection system used for the quadrature squeezing measurements described in Chapter 6. We used two matched InGaAs photodetectors (Epitaxx ETX 500T) with a diameter of 500 μm, a quantum efficiency of 88% and a bandwidth of 140 MHz. The caps of the detectors were removed to avoid reflection losses from the front windows. A bias voltage of 5 V was applied to the detectors. A number of inductors and capacitors (see Fig. 4.4 for details) rejected the electrical noise from the power supply. The dc-photocurrents generated in the two photodiodes were monitored on separate current meters. The circuit was hard-wired to produce the difference-photocurrent at the output. A 50 MHz low-pass filter (Mini-Circuits SLP-50) rejected the large classical noise at the 81 MHz repetition frequency of the OPO in order to prevent the subsequent low-noise amplifier (Avantec UTC-101-1) from saturating. The amplified signal was then analysed using an rf spectrum analyser. The whole circuit was shielded by a metal box to avoid rf pick-up.

The total detection efficiency η_{det} of a homodyne detection system depends on three

ingredients,

$$\eta_{det} = \eta_{pd} \times \eta_{opt} \times \eta_{int}, \tag{4.13}$$

where η_{pd} is the quantum efficiency of the photodetectors, η_{opt} = [1−(optical losses)] is the optical efficiency of the system , and $\eta_{int} = V^2$ the interferometric overlap efficiency of the LO with the signal beam, with the fringe visibility V [17].

4.3.2 Photon-number squeezing detection

Balanced detection also provides significant advantages for detecting photon-number squeezed light. By adding and subtracting the photocurrents from the two photodetectors we obtain both the total photon-number fluctuations and the shot noise level.

The quantum-mechanical analysis of a balanced detector [74] shows that noise in the difference photocurrent is exactly equal to shot noise.[2] Adding the photocurrents evidently provides the total photon-number fluctuations as the detection with a single photodetector would.

Fig. 4.5 shows the circuit diagram of the detection system used for the photon-number squeezing measurements described in Chapter 7. We used two InGaAs photodetectors (EG&G C30641) with a diameter of 1 mm, an efficiency of 85% and a bandwidth of 75 MHz. The caps of the detectors were again removed to avoid reflection losses from the front windows. A bias voltage of 2 V was applied to the detectors. A number of inductors and capacitors (see Fig. 4.5 for details) rejected the electrical noise from the power supply. The sum of the dc-photocurrents generated in the two photodiodes was monitored on a current meter. Balancing was achieved by comparing the dc-photocurrents measured when one detector was blocked. The signals from the two detectors were then separately amplified in low noise amplifiers (Avantec UTC-101-1) after passing through 50 MHz

[2]This is equivalent to homodyne detection measuring vacuum fluctuations when the signal beam is blocked as in §§ 4.3.1.

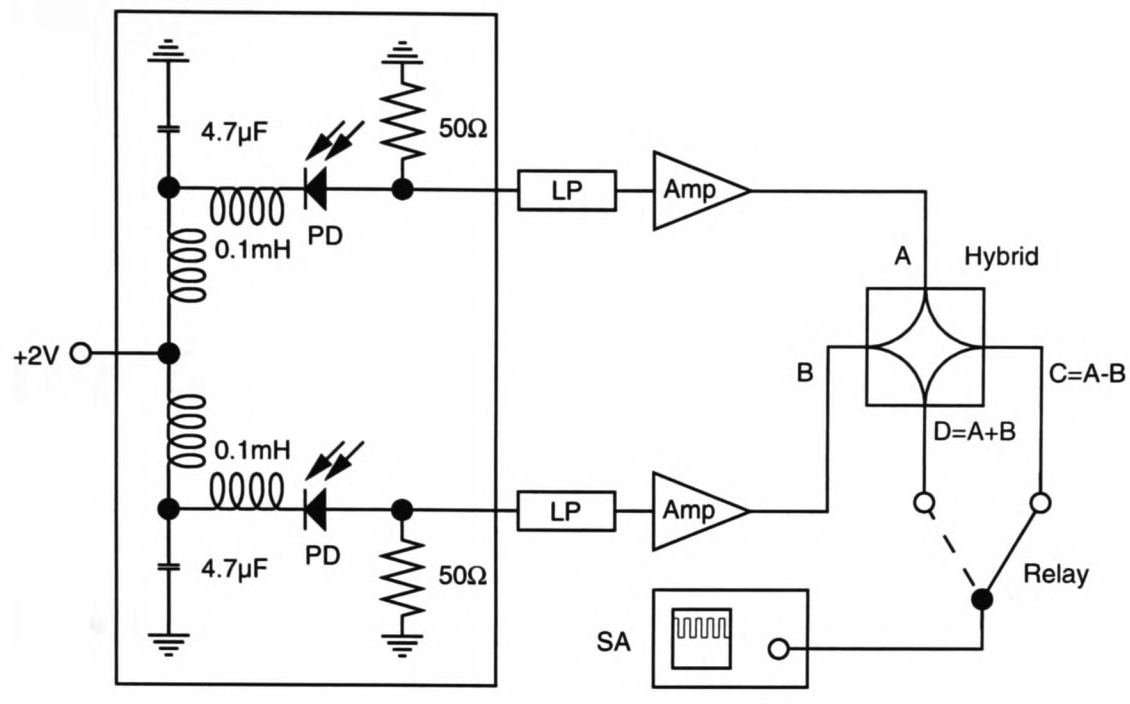

Figure 4.5: Circuit diagram of the balanced detection system used for photon-number squeezing. PD, photodetector; LP, 50 MHz low-pass filter; Amp, low-noise amplifier; SA, spectrum analyser.

low-pass filters (Mini-Circuits SLP-50). The two signals were then recombined in a rf hybrid junction (Macom HH-107). The sum and the difference rf noise components were then analysed using an rf spectrum analyser. The whole circuit was shielded by a metal box to avoid rf pick-up. Care has to be taken that the components in the two separate detection chains are phase-matched as the hybrid junction relies on this to provide exact addition and subtraction. This is achieved by adjusting the cable lengths between the amplifiers and the hybrid junction. A small gain mismatch (<20%), however, does not significantly modify the results [75].

Chapter 5

Ultrafast two-photon nonlinearities in CdSe

Contents

5.1 Introduction 51

5.2 Experimental setup 53

5.3 Nonlinear absorption 53

5.4 Autocorrelations 58

5.5 Nonlinear figure of merit 64

5.6 Spectra 65

5.7 Conclusions 67

5.1 Introduction

The optical nonlinearities of semiconductors in the spectral region close to midgap offer attractive properties for all-optical switching and other signal processing applications [49, 50, 51], as well as for the generation of squeezed light [8, 9] (cf. Chapter 6). At photon energies just below halfgap, the advantage of the broad two-photon resonance in the nonlinear refractive index is combined with very low absorption losses. AlGaAs waveguides have been studied extensively in the wavelength range around 1.5 μm, which is of prime interest for optical communications [76, 77]. In this chapter we present results on CdSe which show it to be a promising alternative material for this wavelength range due to its halfgap energy of 0.875 eV (1.417 μm) [78].

The nonlinear phenomena involved in the propagation of high intensity ultrashort pulses through a semiconductor crystal at photon energies just below the halfgap resonance (i.e. $< E_G/2$, where E_G is the bandgap energy) are complicated. The fundamental effect is self-phase modulation (SPM) in which the pulse induces a nonlinear phase shift $\Delta\Phi$ through the nonlinear refractive index n_2 of the medium. This produces spectral broadening, and one of the standard techniques for deducing $\Delta\Phi$ is to analyse the spectrum of the transmitted pulses [76, 77, 79, 80]. However, the analysis of the spectral broadening becomes increasingly complicated as the pulses get shorter and their spectra become wider. The spectra are sensitive to temporal asymmetry in the laser pulses [79, 52] and also to dispersion in the nonlinear coefficients [81]. Moreover, a number of other nonlinear phenomena can occur in addition to SPM, and these can also have a significant effect on the spectrum. Examples of these effects are free carrier nonlinearities associated with nonlinear absorption [82] and stimulated Raman scattering [83]. Because of these complications in analysing the spectra, we have adopted a different approach and have investigated the SPM effects in the time domain via interferometric autocorrelation measurements. Diels *et al.* have already pointed out that the autocorrelations are very

sensitive to the phase modulation associated with the nonlinear chirp due to SPM [84]. In our work we have studied the intensity dependence of the interferometric autocorrelations of the femtosecond pulses transmitted through a CdSe sample. We find that by combining the experimental measurements with numerical modelling, we are able to determine the nonlinear phase shifts with relative ease. Thus the use of time domain measurements provides a convenient alternative approach to study the nonlinear phenomena, especially for the femtosecond regime.

In § 5.2 we explain the experimental details, § 5.3 discusses the nonlinear absorption in the sample for wavelengths between 1.419 μm and 1.543 μm. In § 5.4 the measurements and simulations of the interferometric autocorrelations are presented and the value for the nonlinear refractive index is extracted. We concentrate our analysis on two representative wavelengths, namely 1.444 μm and 1.494 μm. The nonlinear behaviour at moderate intensities is similar at the two wavelengths, but at the highest intensities studied, we observe that the autocorrelations are qualitatively different. In order to explain this wavelength dependence, we develop a numerical model of the autocorrelations. The model includes the SPM effects due to the ultrafast n_2 nonlinearity, and also the free carrier nonlinearities associated with the electrons and holes generated by nonlinear absorption. By assuming that the effective free carrier cross-section depends on the wavelength, we achieve very good agreement between the numerical model and the experimental results. In § 5.5 the nonlinear figure of merit is discussed, and CdSe is shown to compare favourably with AlGaAs as a nonlinear optical material in this wavelength region. In § 5.6 the spectra of the transmitted pulses are presented and explained qualitatively. § 5.7 concludes the chapter.

The work presented in this chapter has been published in ref. [11].

5.2 Experimental setup

In our experiments we used a hexagonal single crystal of CdSe with thickness $L = 2$ mm, cut with the c-axis normal to the surface.[1] The high resistivity sample was confirmed to be of good structural quality by x-ray diffraction. The crystal was antireflection coated with a quarter wave Al_2O_3 coating to reduce Fresnel losses. Tunable femtosecond pulses in the wavelength range 1.419-1.543 μm were provided by the optical parametric oscillator described in §§ 4.1.3. The linearly polarised pump pulses were focused into the crystal along its c-axis with a 38.1 mm lens. The measured spot radius w_0 in the focal plane was 17 μm. This results in an effective optical length L_{eff} of 1.8 mm, where:

$$L_{\text{eff}} = 2z_R \tan^{-1}(L/2z_R), \tag{5.1}$$

and the confocal parameter z_R for a central wavelength λ and refractive index n_0:

$$z_R = \frac{\pi w_0^2 n_0}{\lambda}. \tag{5.2}$$

The transmitted light was measured with a power meter. We used the scanning interferometric autocorrelator described in § 4.2 to analyse the transmitted pulses in the time domain and a spectrometer to measure their spectra.

5.3 Nonlinear absorption

Fig. 5.1 shows the transmission as a function of the focussed intensity I_0 in the crystal at centre wavelengths of 1.419, 1.444, 1.494 and 1.543 μm and demonstrates the transition from 2PA- to 3PA-dominant nonlinear absorption. I_0 was determined from the peak pulse power P according to $I_0 = P/(\pi {w_0}^2)$. The circles show the measured values, and the lines are calculated curves discussed below. At all wavelengths we measured a transmission of ≈ 96 % at low intensities which then decreased as I_0 increased due to the

[1] sample supplied by Cleveland Crystals.

nonlinear absorption. Values of the nonlinear absorption coefficients of the sample can in principle be determined by analysing the intensity dependence of the transmission. The propagation equation for the intensity $I(z)$ of the beam travelling through the sample is:

$$\frac{dI}{dz} = -\left[\alpha_1(\lambda) + \alpha_2(\lambda)I + \alpha_3(\lambda)I^2 + \cdots\right] I, \tag{5.3}$$

where α_1, α_2 and α_3 represent the coefficients for linear absorption, two-photon absorption (2PA) and three-photon absorption (3PA), respectively. Throughout the wavelength range studied, the linear absorption is essentially negligible, and the low intensity transmission T_0 is determined by the residual reflection losses. Based on measurements in AlGaAs waveguides [77], a 2PA contribution is only expected for wavelengths close to or above the halfgap. In the case where the dominant absorption mechanism is 2PA, the transmission T through a thin sample of effective thickness L_{eff} is given by:

$$\frac{T_0}{T} = 1 + \alpha_2 L_{\text{eff}} I_0. \tag{5.4}$$

If the dominant absorption mechanism is 3PA, the relation takes the form:

$$\left(\frac{T_0}{T}\right)^2 = 1 + 2T_0\alpha_3 L_{\text{eff}} I_0^2. \tag{5.5}$$

The dotted lines in Fig. 5.1(a) and (b) were obtained by fitting the low intensity data using (5.4). This yields 2PA coefficients $\alpha_{2,\text{fit}}$ of 1.1 cmGW^{-1} (at 1.419 μm) and 0.2 cmGW^{-1} (at 1.444 μm). These are in good agreement with values found in AlGaAs [77] at the same photon energy/bandgap ratios (0.50 E_G and 0.49 E_G, respectively). At 1.419 μm the pure 2PA formula also provides a reasonable fit to the high intensity data, which is not the case at 1.444 μm. This indicates that at 1.444 μm higher order terms need to be included.

The solid lines in Figs. 5.1(a) and (b), which give a better fit to the experimental results, were obtained by parameterising the nonlinear absorption through an effective intensity-dependent 2PA coefficient of the form $\alpha_{2,\text{eff}} = \alpha_2 + \alpha_3 I_0$ which includes both the

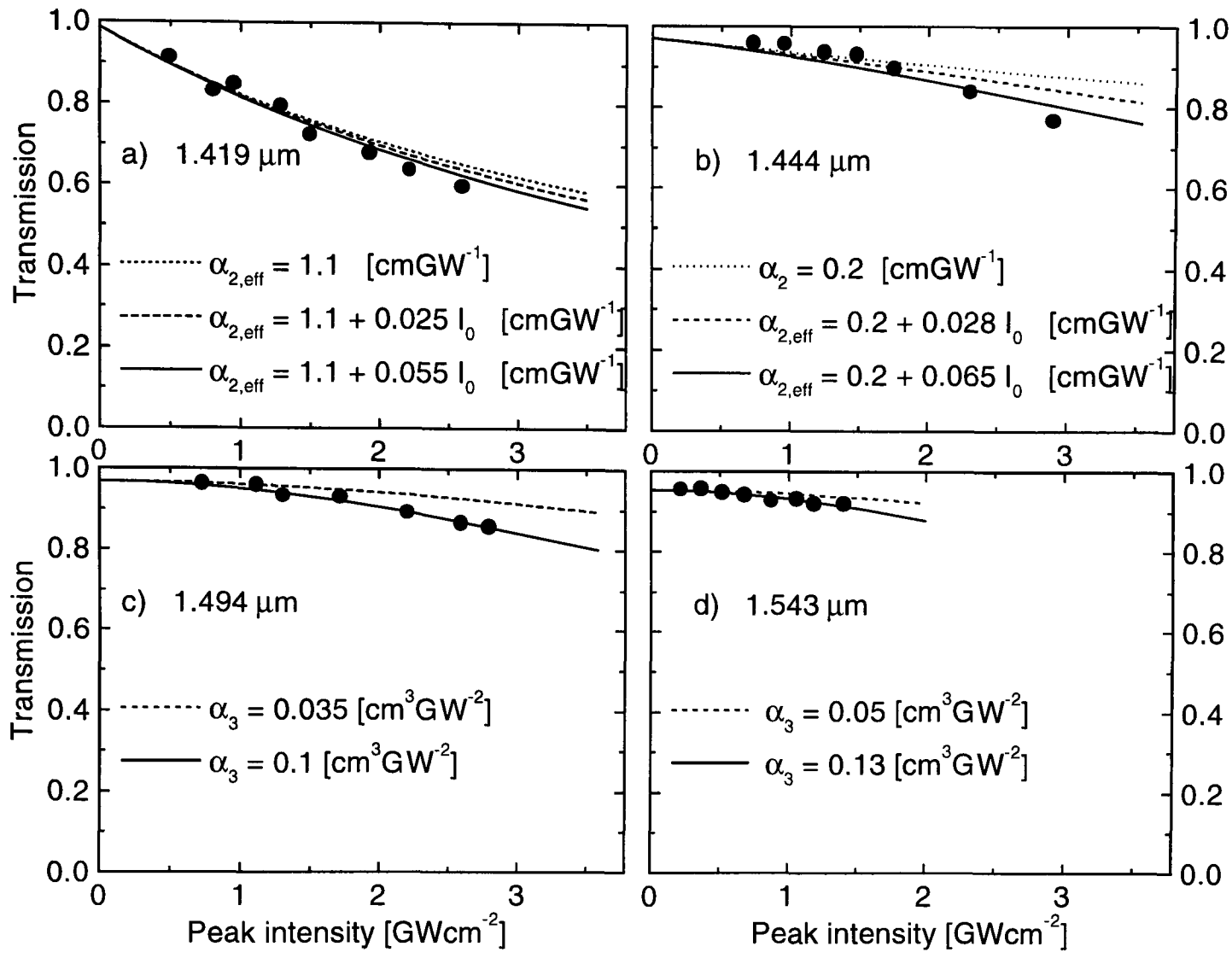

Figure 5.1: Transmission through the sample as a function of intensity I_0. The circles show the measured values. In (a) and (b) the dotted lines show the low intensity fits used to obtain α_2 from (5.4), the dashed and the solid lines are obtained from the parameterisation using an effective 2PA coefficient $\alpha_{2,\text{eff}}$ as discussed in the text. The solid lines represent the best fits, while the dashed lines use the theoretical value $\alpha_{3,\text{th}}$ from ref. [57]. (c) and (d) show a parameterisation purely based on 3PA for two different values of α_3. The solid lines represent the best fit to the data according to (5.5), while the dashed lines use the theoretical values $\alpha_{3,\text{th}}$ from ref. [57].

2PA- and 3PA-coefficients. The dashed lines use the $\alpha_{3,\text{th}}$ values obtained from a simple two-band model by Wherrett [57]. The values for these parameterisations are listed in

Table 5.1.

For the lower photon energies (1.494 μm and longer wavelengths), 2PA can be neglected and only 3PA needs to be considered. Values for $\alpha_{3,\text{fit}}$ at 1.494 μm and 1.543 μm have been obtained by fitting the data using (5.5). In Fig. 5.1(c) and (d) the solid lines represent the best fits to the data, whereas the dashed lines use the values $\alpha_{3,\text{th}}$ obtained from the model by Wherrett [57].

Table 5.1: Various nonlinear optical parameters for different wavelengths λ. $\alpha_{2,\text{fit}}$, $\alpha_{3,\text{fit}}$ are the 2PA and 3PA coefficient as obtained from the fits in Figure 1; $\alpha_{3,\text{th}}$ is the 3PA coefficient as obtained from [57]; $\alpha_{2,\text{eff}}$ is the effective nonlinear absorption for the intensity leading to a $\pi/2$ phase shift; $n_{2,\text{fit}}$, $n_{2,\text{th}}$ are the nonlinear refractive index obtained from our experiment and the theoretical value from [49]; T_{FOM} is the nonlinear figure of merit for the intensity leading to a $\pi/2$ phase shift

$\lambda[\mu\text{m}]$	1.419	1.444	1.494	1.543
$\alpha_{2,\text{fit}}[\text{cmGW}^{-1}]$	1.1	0.20	-	-
$\alpha_{3,\text{fit}}[\text{cm}^3\text{GW}^{-2}]$	0.055	0.065	0.10	0.13
$\alpha_{3,\text{th}}[\text{cm}^3\text{GW}^{-2}]$	0.025	0.028	0.035	0.050
$\alpha_{2,\text{eff}}[\text{cmGW}^{-1}]$	1.2	0.30	0.15	0.20
$n_{2,\text{fit}}[10^{-13}\text{cm}^2\text{W}^{-1}]$	1.3	1.3	1.3	1.3
$n_{2,\text{th}}[10^{-13}\text{cm}^2\text{W}^{-1}]$	2.9	2.4	1.9	1.7
T_{FOM}	2.6	0.66	0.34	0.47

In spite of the relatively large errors involved in these parameters, it is interesting to compare them with values from the literature. The values for the 3PA coefficient $\alpha_{3,\text{fit}}$ obtained by fitting the data are consistently larger than the theoretical values $\alpha_{3,\text{th}}$ obtained from the two-band model of Wherrett [57] but show the predicted wavelength

dependence. The discrepancy is most probably caused by the over-simplification of using only a two-band model for the theory. Picosecond measurements in AlGaAs [77] yielded very similar values to our CdSe-values for corresponding photon energies: At $0.46E_G$ (corresponding to 1.543 μm in CdSe and 1.634 μm in AlGaAs) we obtain 0.13 $\mathrm{cm^3GW^{-2}}$, as compared to 0.12 $\mathrm{cm^3GW^{-2}}$ in AlGaAs. At $0.49E_G$ (1.444 μm in CdSe, 1.535 μm in AlGaAs), our measurements yield 0.065 $\mathrm{cm^3GW^{-2}}$, while the measurement in AlGaAs gave 0.04 $\mathrm{cm^3GW^{-2}}$. The total nonlinear absorption is given as $\alpha_{2,\mathrm{eff}}$ for an intensity of 1.5 $\mathrm{GWcm^{-2}}$ which yields a $\pi/2$ phase shift. We see that $\alpha_{2,\mathrm{eff}}$ goes through a minimum at approximately 1.49 μm.

For intensities above 2.5 $\mathrm{GWcm^{-2}}$ at 1.444 μm, we observe that the transmission is smaller than predicted by (5.4) even after allowing for 3PA via $\alpha_{3,\mathrm{fit}}$. This implies an additional contribution to the nonlinear absorption. In contrast to most previously reported measurements of multi-photon absorption in semiconductors near halfgap, where pulse durations of 500 fs and longer were used, our measurements use 83 fs pulses. The input pulses therefore have a spectral bandwidth of about 0.03 μm. High intensity pulses are spectrally broadened by SPM to as much as 0.14 μm after passing through the sample (cf. § 5.6). If the centre wavelength is close to $E_G/2$ (as is the case at 1.444 μm), the blue part of the spectrum then extends above the halfgap energy at high intensity and experiences a much larger value of α_2, and the net result is that the effective 2PA for the pulse at high intensities is larger than at low intensities. Thus at a centre wavelength of 1.444 μm, which is only 0.027 μm above the halfgap wavelength, we expect that the increase of multi-photon absorption at high intensities is partly due to this power-dependent 2PA. For the longer wavelengths investigated (1.494 μm and 1.543 μm) this effect does not occur and the 3PA fit using (5.5) works very well even at high intensity.

5.4 Autocorrelations

5.4.1 Measurements

Fig. 5.2 shows the interferometric autocorrelations measured as a function of increasing intensity at 1.444 μm and 1.494 μm. The input pulses at the two wavelengths are shown in Figs. 5.2(a) and (e), respectively. Note that the input pulse duration varied as the wavelength was tuned, so that at 1.444 μm the input pulse width was 83 fs, while at 1.494 μm it was 117 fs. At both wavelengths we observe that the autocorrelation envelopes narrow as the intensity increases, even though the overall pulse duration remains constant. This is a clear signature of nonlinear chirp in the transmitted pulses. In the case of a pulse chirped by SPM a narrowing of the upper and lower envelopes is expected [84]. However, since the leading and trailing edges of the pulse remain coherent with each other, the interference in the wings of the interferometric autocorrelation will extend to delays as long as those for an unchirped pulse of the same duration. This is exactly what we observe. The narrowing of the upper and lower envelopes is a sensitive indication of phase modulation and can be used to extract values of the nonlinear phase shift as discussed in the next section.

At the highest intensities studied (Figs. 5.2(d) and (h)), we observe a striking qualitative difference in the shape of the autocorrelations for the two wavelengths. For a nonlinear chirp generated from a third-order nonlinearity, we would have expected to observe the development of crossings in the wings of the autocorrelations as the nonlinear phase shift increases [84]. This behaviour is clearly observed at 1.494 μm, but not at 1.444 μm. The suppression of the crossings in the wings was also observed at wavelengths shorter than 1.444 μm not shown in Fig. 5.2.

In the following subsection we will develop a model to account for the narrowing of the envelopes with increasing intensity and for the difference in behaviour at high intensities.

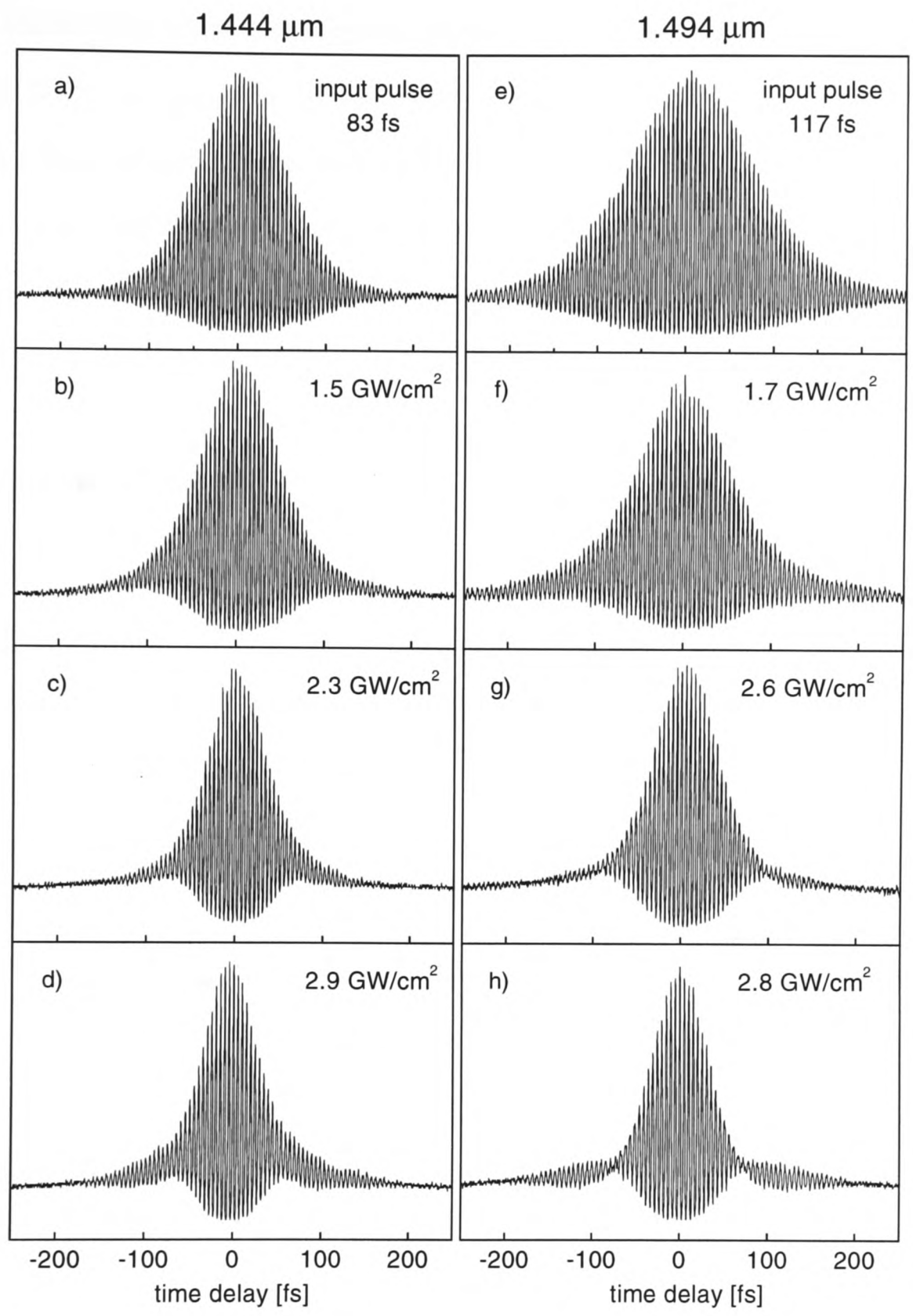

Figure 5.2: Experimental autocorrelations for increasing intensities at 1.444 μm (a–d) and 1.494 μm (e–h). The input pulses at the two wavelengths are shown in (a) and (e) respectively. The nonlinear phase shift at the maximum intensities is about π for both wavelengths.

The model shows that at the maximum intensities studied a phase shift of about π was obtained for both wavelengths. It also shows that the suppression of the wings can be attributed to free carrier effects following 2PA. These free carrier effects are expected to be much more significant at wavelengths close to the halfgap at 1.417 μm. We thus attribute the difference in behaviour observed at the two wavelengths at high intensities to the fact that 1.444 μm is much closer to the halfgap wavelength than 1.494 μm.

5.4.2 Calculations

In this subsection we describe how the values of the nonlinear phase shift, and thus the nonlinear refractive index n_2, can be extracted from the experimental results by numerical modelling of the autocorrelation. We assume that the intensity of the input pulses has a bandwidth-limited sech^2 time dependence with a full-width half-maximum duration of t_0 (cf. §§ 4.1.3). The electric field $E(t)$ for the optical pulse transmitted through the sample is then given by

$$\frac{E(t)}{E_0} = \text{sech}\left(1.76\frac{t}{t_0}\right) \exp i[\omega_0 t + \Delta\Phi(t)], \tag{5.6}$$

where E_0 is the peak electric field strength, ω_0 is the centre frequency and $\Delta\Phi(t)$ is the nonlinear phase shift.[2] We assume that there are two contributions to $\Delta\Phi(t)$:

$$\Delta\Phi(t) = \frac{2\pi L_{\text{eff}}}{\lambda}\left[n_2 I(t) + \sigma_{\text{eh}} N(t)\right]. \tag{5.7}$$

The first term arises from the instantaneous bound electronic nonlinearity, while the second originates from the phase shift due to the free carriers generated by nonlinear absorption. σ_{eh} denotes the real part of the free carrier nonlinear cross-section (i.e. the change in refractive index per excited carrier pair), and $N(t)$ is the density of the photogenerated carrier pairs. In the case where the carriers are generated by nonlinear

[2]Note that the linear dispersion over the spectral width of the pulses is negligible [85].

absorption, $N(t)$ can be approximated by:

$$N(t) = \frac{\alpha_{2,\text{eff}}}{2\hbar\omega_0} \int_{-\infty}^{t} I^2(t')dt', \tag{5.8}$$

where $\alpha_{2,\text{eff}}$ is taken from the solid line fits in Fig 5.1. The dispersion of n_2 and $\alpha_{2,\text{eff}}$ over the spectral width of the pulse is neglected.

We used these expressions to calculate the time-delay-dependent signal $S(\tau)$ of the second-harmonic generation in the interferometric autocorrelator:

$$S(\tau) \propto \int_{-\infty}^{+\infty} \left|[E(t) + E(t+\tau)]^2\right|^2 dt. \tag{5.9}$$

Fig. 5.3 shows the results of the simulations for intensities equal to the experimental values shown in Fig. 5.2. A constant value of n_2 of $1.3 \pm 0.3 \times 10^{-13}\ cm^2W^{-1}$ resulted in the best fits to the data at all the wavelengths, leading to a nonlinear phase shift of about π at the highest intensities considered. No significant dispersion in n_2 could be observed over the wavelength range studied. Table 5.1 compares our experimental values to the theoretical values obtained from the two-band model by Sheik-Bahae [49]. The model yields slightly higher values than our measurements. The values obtained in AlGaAs in this wavelength regime lie between 1.1×10^{-13} cm^{2}W^{-1} and 1.8×10^{-13} cm^{2}W^{-1} [77].

In the simulations for 1.444 μm we assumed a value of $\sigma_{\text{eh}} = -6.50 \times 10^{-21}\ cm^3$. This value was calculated from the Drude model [86]. For a centre wavelength of 1.444 μm which is very close to the halfgap wavelength most carriers are generated by 2PA, which results in a thermalised 300 K free carrier population close to the band edge. The resulting autocorrelation traces (Figs. 5.3(a–d)) agree very well with the measured data (Figs. 5.2(a–d)). Note that this free carrier term is negative and hence leads to a (temporally varying) small reduction of the nonlinear phase shift.

The effect of the free carrier term on the autocorrelations is shown more clearly in Fig. 5.4. In this Figure we show the simulations for $\lambda = 1.444$ μm and $I_0 = 2.9$ GWcm^{-2} for two different values of σ_{eh}. Fig. 5.4(a) shows the simulation for $\sigma_{\text{eh}} = 0$ (i.e. no

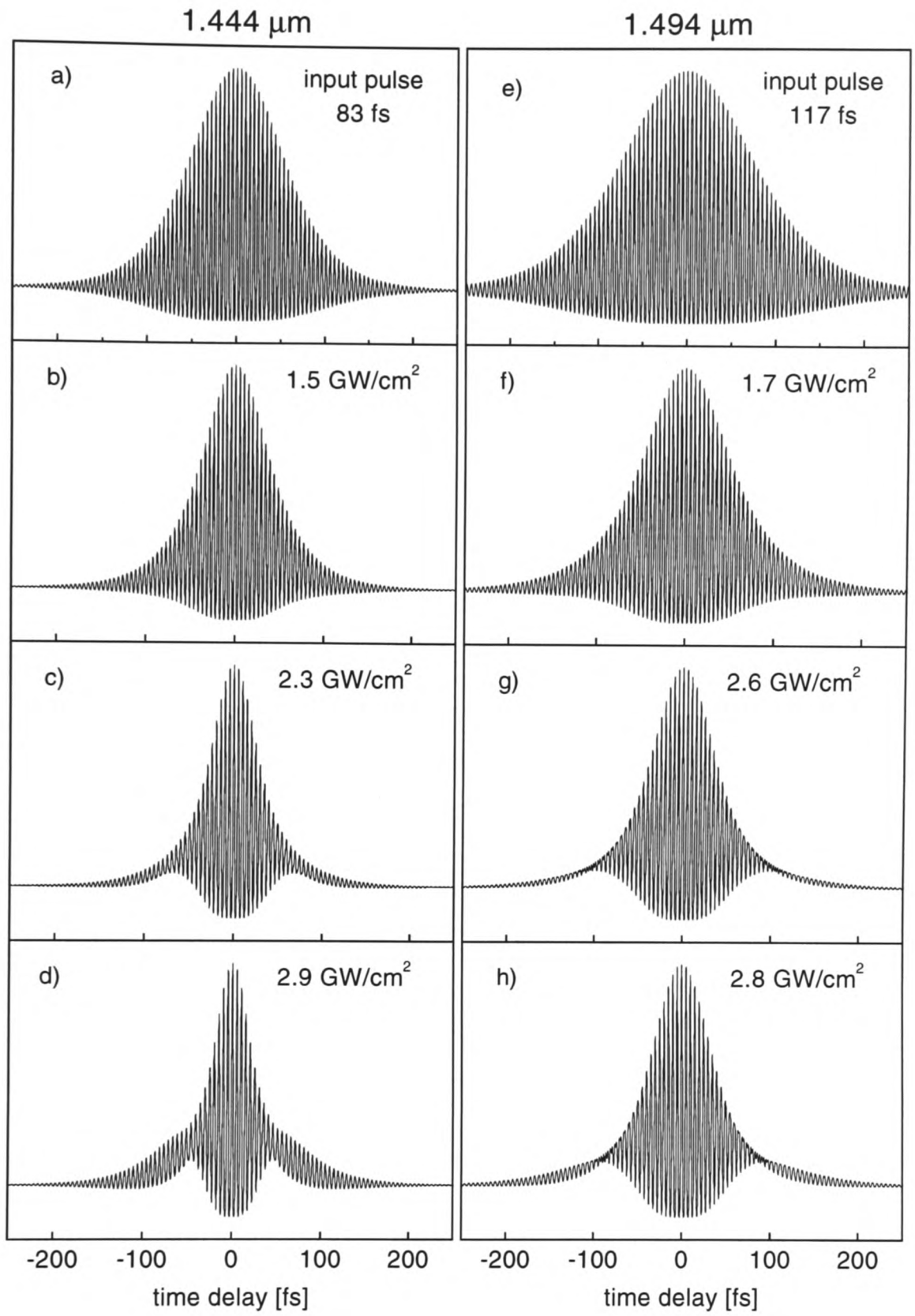

Figure 5.3: Calculated autocorrelations at the same wavelengths and intensities as for Fig. 5.2. A value of $n_2 = 1.3 \times 10^{-13}$ cm^{2}W^{-1} was assumed for both wavelengths. The simulations for 1.444 μm include a free carrier nonlinearity with cross-section $\sigma_{\mathrm{eh}} = -6.50 \times 10^{-21}$ cm^3, while the simulations at 1.494 μm assume $\sigma_{\mathrm{eh}} = 0$.

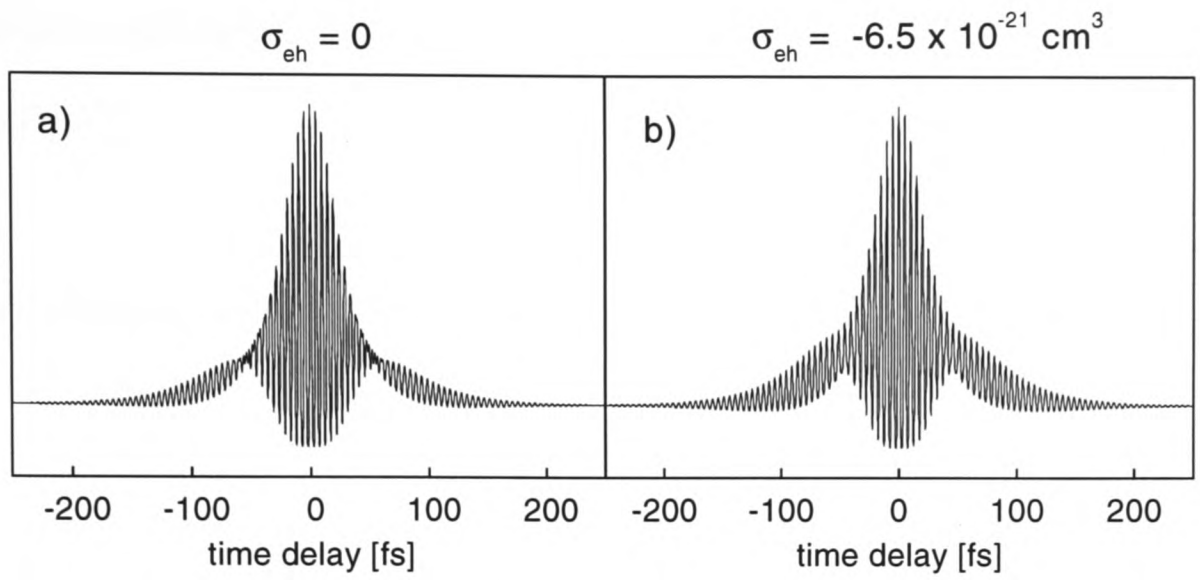

Figure 5.4: Effect of the free carrier term on the calculated autocorrelation at 1.444 μm for an intensity of $I_0 = 2.9$ GWcm^{-2}. (a) shows the result for pure SPM with $\sigma_{eh} = 0$, while (b) shows the result when a free carrier nonlinearity with $\sigma_{eh} = -6.50 \times 10^{-21}$ cm^3 is included.

free carrier effects), while Fig. 5.4(b) shows the simulation for $\sigma_{eh} = -6.50 \times 10^{-21}\ cm^3$ (i.e. the same as for Figs. 5.3(b–d)) and a free carrier density of about $10^{15}\ cm^{-3}$. It is clear that the free carrier nonlinearity accounts for the suppression of the crossings in the wings of the autocorrelation observed at 1.444 μm in the experimental data.

For the simulations at 1.494 μm shown in Figs. 5.3(e–h), we found that the best fit to the experimental data was obtained by neglecting the free carrier contribution to the nonlinear phase shift (i.e. by taking $\sigma_{eh} = 0$). This is a somewhat surprising conclusion, considering that Fig. 5.1 shows that the total nonlinear absorption at the two wavelengths is quite similar. We suggest that the reason why the free carrier effects are small at 1.494 μm is that most of the carriers produced at this wavelength arise from 3PA. They are therefore excited high into the conduction band, and do not have time to relax to the band edge within the duration of the ~100 fs pulse (Measurements in other II-VI materials [87] suggest a hot-carrier cooling time of the order of 2 ps, in GaAs and AlGaAs [88] cooling times of 1-2 ps have been measured). By the Kramers-Kronig

relation, their contribution to the change in the refractive index at the wavelength of interest is greatly reduced compared to 300 K carriers at the band edge.

5.5 Nonlinear figure of merit

In order to compare materials for their applicability in nonlinear optics, an important parameter is the amount of phase shift which can be accumulated over the sample length. The phase shift should be large, whereas the detrimental effects of linear and nonlinear absorption should be minimised. There have been various definitions for figures of merit to quantify this. Here we adopt the standard definition used in waveguide optics [89]

$$T_{\mathrm{FOM}} = \frac{2\alpha_2\lambda}{n_2}. \tag{5.10}$$

The general criterion for good nonlinear optical materials is $T_{\mathrm{FOM}} < 1$. To account for 2PA as well as 3PA, we use the $\alpha_{2,\mathrm{eff}}$ obtained from Fig. 5.1. This means that T_{FOM} deteriorates at high intensities. In Table 5.1 we show the values of T_{FOM} obtained at the two wavelengths studied in detail. We used the value of n_2 that we obtained from the fits described in § 5.4 ($1.3 \times 10^{-13} cm^2 W^{-1}$), and the values of $\alpha_{2,\mathrm{eff}}$ for intensities of ~ 1.5 GWcm^{-2}. This corresponds to a nonlinear phase shift of $\pi/2$, which means that the values of T_{FOM} are for realistic working conditions. The smallest value of T_{FOM} is found at 1.494 μm, where the 2PA has become negligible and the 3PA is still small. At shorter as well as longer wavelengths T_{FOM} increases again. The values of both n_2 and T_{FOM} found for CdSe compare favourably with those obtained in AlGaAs, and the figure of merit shows a similar wavelength dependence [77].

5.6 Spectra

We have also analysed the output pulses in the frequency domain by measuring their spectra. These spectra are shown in Fig. 5.5 for input pulses at the same centre wavelengths and pulse duration as in the previous sections, i.e. 1.419 μm (76 fs), 1.444 μm (83 fs), 1.494 μm (117 fs) and 1.543 μm (147 fs).

As discussed in Chapter 3 there are three main nonlinear effects determining the shape of the transmission spectra:

- Self-phase modulation (SPM)
- Nonlinear absorption
- Stimulated Raman scattering

In addition, the spectra are sensitive to temporal asymmetry in the laser pulses [79, 52] and also to dispersion in the nonlinear coefficients [81]. The combination of all these effects makes it a very difficult task to extract accurate values for the nonlinear refractive index. We can therefore only give a qualitative explanation of the effects observed.

The effect of SPM can be seen best at 1.494 μm (Fig. 5.5(c)). At this wavelength the asymmetry is thought to be due to stimulated Raman scattering. At shorter wavelengths this asymmetry is increased by the effect of 2PA. At 1.444 μm the effect of the power-dependent 2PA discussed in § 5.3 can be seen. As the SPM broadens the spectrum, 2PA in the short wavelength region of the spectrum above halfgap is increased. Note that the fringes in Figs. 5.5(a) and (b) originate from absorption by water vapour in the air.

With increasing intensity and photon-energy we also see narrow peaks appearing on either side of the spectra. These peaks are seeded by a very weak component of the pump-beam at between 35 meV and 50 meV from the fundamental originating from OPO. These peaks are amplified within the sample, most likely by stimulated Raman scattering. Their integrated intensity, however, remains very small.

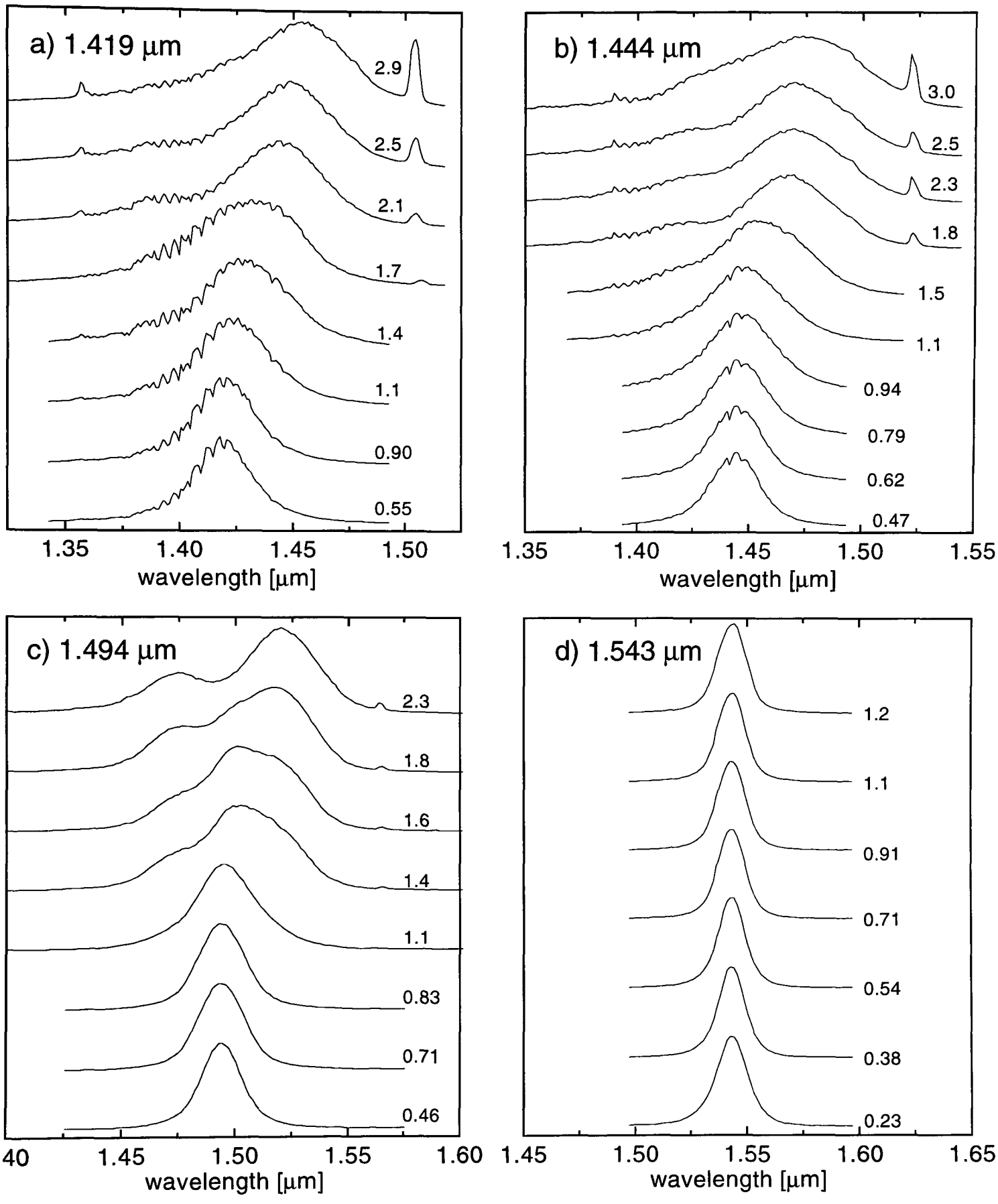

Figure 5.5: Spectra of pulses transmitted through the CdSe sample for different wavelengths. The numbers to the right of each curve are the respective intensities in [GWcm^{-2}].

5.7 Conclusions

- We have measured and modelled the intensity dependence of interferometric autocorrelations of fs-pulses transmitted through bulk CdSe at wavelengths near 1.5 μm, i.e. just below its halfgap energy. The simulations fit the measured data very well and allow an accurate determination of the nonlinear phase shift.

- Two-photon absorption produces a significant change in the autocorrelation signature through free carrier-induced changes in the nonlinear refractive index.

- The technique presented here is especially attractive for determining the nonlinear refractive index in the femtosecond-regime, where the determination by spectral analysis gets increasingly difficult.

- Ultrafast phase shifts of up to $\sim \pi$ were obtained and the nonlinear figure of merit at this wavelength was shown to compare favourably with that obtained for AlGaAs. This makes CdSe a promising alternative material for ultrafast nonlinear optical applications in this technologically important wavelength region.

- The spectra of the transmitted pulses are measured. The underlying SPM is seen to be strongly masked by 2PA and stimulated Raman scattering. This makes the autocorrelation technique a useful alternative to extract the nonlinear phase shift.

Chapter 6

Quadrature-squeezed light generation in CdSe

Contents

6.1 Introduction 69

6.2 Experimental setup 70

6.3 Results 72

6.4 Feasibility of extending the XPM-technique to waveguides 79

6.5 Conclusions and outlook 83

6.1 Introduction

The channel capacity and the error rates in coherent optical communication systems are expected to be improved by the use of squeezed light [90]. As optical communication systems chiefly operate at wavelengths of about 1.5 μm, a convenient source of squeezed light in this wavelength regime is of considerable interest. Because of their potential in integrated optics, semiconductors could form the basis of such a source. Fox *et al.* have demonstrated an inherently simple technique to obtain quadrature squeezing in a single pass of a laser pulse through a short semiconductor crystal at room temperature either by self-phase modulation (SPM) [8] or by cross-phase modulation (XPM) [9]. Making use of the ultrafast nonlinearities in CdSe described in the previous chapter, we have extended this technique to the spectral region near 1.5 μm. To our knowledge this is the first experimental demonstration of quadrature squeezing obtained from a semiconductor at this wavelength and also the first squeezing in a hexagonal semiconductor crystal.

The compact travelling-wave geometry of the experiment (described in § 6.2) and the use of a semiconductor offer several advantages over previous methods of femtosecond-pulsed quadrature squeezing at 1.55 μm in optical fibres [61, 62]. Using a tunable femtosecond-pulsed optical parametric oscillator (cf. §§ 4.1.3), we have investigated the wavelength as well as the intensity dependence of the squeezing using two different local oscillator arrangements. This is discussed in § 6.3. In § 6.4 we investigate the feasibility of extending the present technique to AlGaAs waveguides, where it could be possible to achieve squeezing at greatly reduced average powers. § 6.5 concludes the chapter.

Part of the work presented in this chapter has been published in refs. [10, 91].

6.2 Experimental setup

Our technique for quadrature squeezing in semiconductors uses the properties of the third-order nonlinear susceptibility $\chi^{(3)}$ at photon energies slightly below half the bandgap energy (E_G). There is a broad resonance in $\mathrm{Re}[\chi^{(3)}]$ near $E_G/2$ because of the two-photon contribution, whereas $\mathrm{Im}[\chi^{(3)}]$ falls to zero for photon energies below halfgap (cf. Chapters 2 and 3). The squeezed light is generated by parametric deamplification in travelling-wave geometry and can arise from both SPM and XPM (cf. Chapter 3). In the present experiment, we used XPM to produce squeezed vacuum polarised orthogonally to the pump. In this case we removed the pump light simply by using a polarising beam splitter (PBS), whereas in the SPM case the pump light had to be removed interferometrically [8].

Fig. 6.1 shows a schematic diagram of the apparatus. The sample was the same as the one examined in Chapter 5, i.e. a 2-mm-thick hexagonal CdSe single crystal (E_G = 1.75 eV), which we cut with the c axis normal to the surface and antireflection coated with a quarter-wave Al_2O_3 coating to reduce Fresnel losses. The pump was the optical parametric oscillator (OPO) described in §§ 4.1.3, tunable from 1.419 to 1.543 μm at 81-MHz repetition frequency. The pulse width varied from 75 to 160 fs, depending on the wavelength λ. After passing through a high-extinction polariser (10^{-5}) the vertically polarised pump pulses were focused into the crystal along its c axis by a 38.1-mm lens. The measured spot radius in the focal plane was 17 μm. A PBS split off the vertically polarised pump light emerging from the sample. As there is no birefringence along the c axis of a hexagonal structure, the beam transmitted though the PBS is the orthogonally polarised squeezed vacuum. There is also a small residual background signal that is due to the imperfect extinction ratio of the PBS and to scattered light. Care was taken to minimise this residual background signal by adjusting the polarisation optics in order to avoid interference with the squeezing measurement.

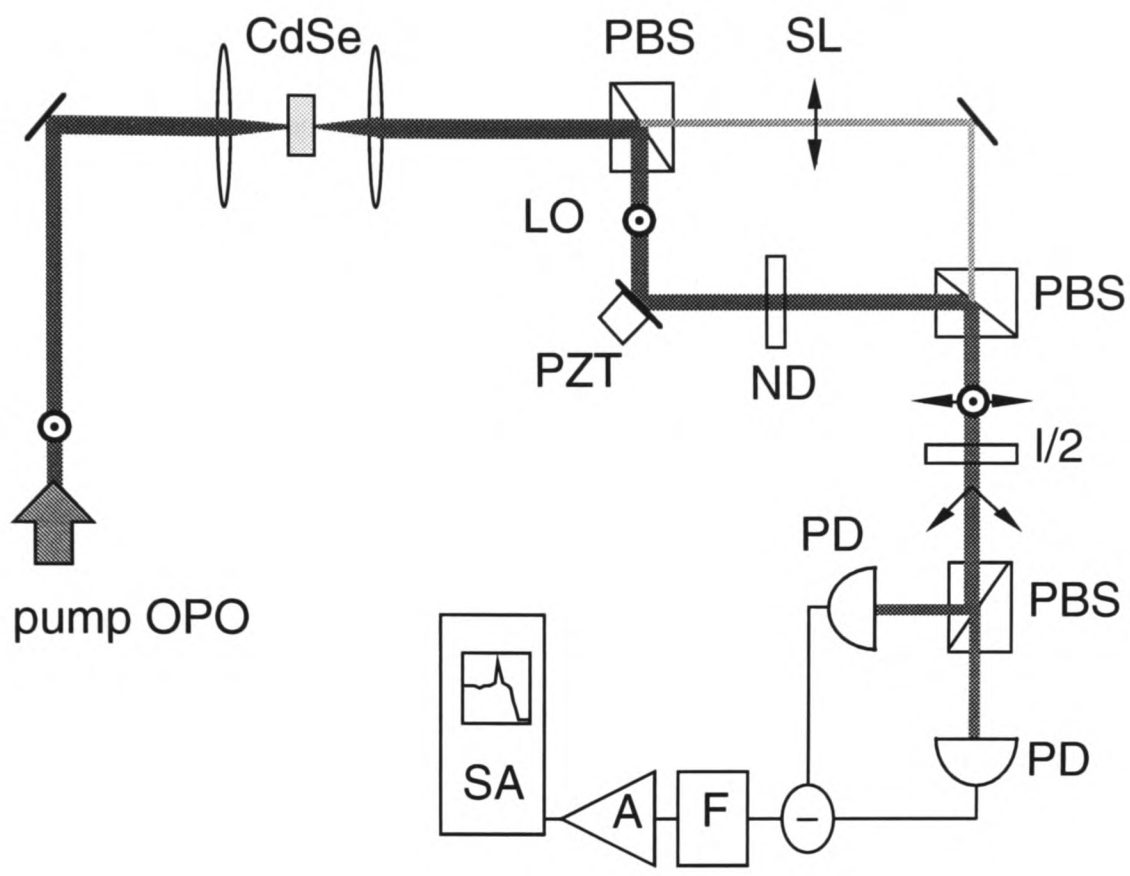

Figure 6.1: Experimental arrangement for cross-phase modulation squeezing using a recycled LO. PBS, polarising beam-splitter; PZT, piezo-electric transducer; $\lambda/2$, half-wave plate; ND, variable attenuator; LO, local oscillator; SL, squeezed light; PD, photodiode; F, rf filters; A, low-noise rf amplifier; SA, spectrum analyser.

The overall transmission of the pulses was measured to be 96% at low intensity, and the losses were due to imperfect AR coatings on the samples and the lenses. For higher intensity, residual two-photon as well as three-photon absorption reduced the transmission (cf. previous chapter). For the measurements presented in this chapter, the total transmission remains greater than 80%, apart from the measurements made at 1.419 μm, where it is reduced to less than 60% at high intensity because of the extension of the pulse spectrum above the halfgap energy and subsequent enhanced two-photon absorption. As seen in the previous chapter the pulses undergo substantial spectral broadening, but their overall pulse duration remains almost unchanged.

The squeezed light was measured with the balanced homodyne detection system de-

scribed in §§ 4.3.1. The photodetectors were 500 μm-wide InGaAs photodiodes (Epitaxx 500T). For most of the measurements we used a recycled pump local oscillator (LO) scheme (an alternative LO arrangement is discussed in §§ 6.3.2). We obtained the LO by attenuating the transmitted pump pulses strongly to restore them to the shot noise level. Typical LO powers were 3 mW per photodiode. We incorporated a variable delay into the LO path to adjust the temporal overlap in the detectors. We recombined the LO and the squeezed vacuum in a second PBS, followed by a half-wave plate ($\lambda/2$) and a further PBS, to obtain exact 50:50 beam splitting for the balanced detection [92]. The common mode rejection ratio was better than 30 dB. A piezoelectric transducer on one of the mirrors served as a phase shifter for the detection. The signal was filtered by a 50-MHz low-pass filter to prevent amplifier saturation by the strong signal at the 81-MHz OPO-repetition rate.

6.3 Results

Fig. 6.2 shows the frequency dependence of the phase-dependent noise measured in the range from 10 to 50 MHz at 1.470 μm. The light curve shows the noise level of the LO only (i.e. with the signal port of the homodyne detector blocked), whereas the dark curve shows the equivalent trace with the squeezed vacuum incident at the signal port. The cw-power incident upon the crystal was 100 mW at 1.470 μm, and the pulse duration was 103 fs, resulting in a peak intensity of 1.3 GWcm^{-2}. The drop of the LO noise at high frequencies stems from the 50-MHz low-pass filter used. We confirmed that the LO noise level corresponds to the shot noise level across the entire frequency range (except near half the repetition frequency, i.e. at 40.5 MHz) by checking the linearity of the spectrum analyser signal against the LO power and also by comparing it with a known shot-noise-limited source (a blackbody emitter). We obtained the signal trace shown in Fig. 6.2 by slowly sweeping the frequency while modulating the piezoelectric transducer.

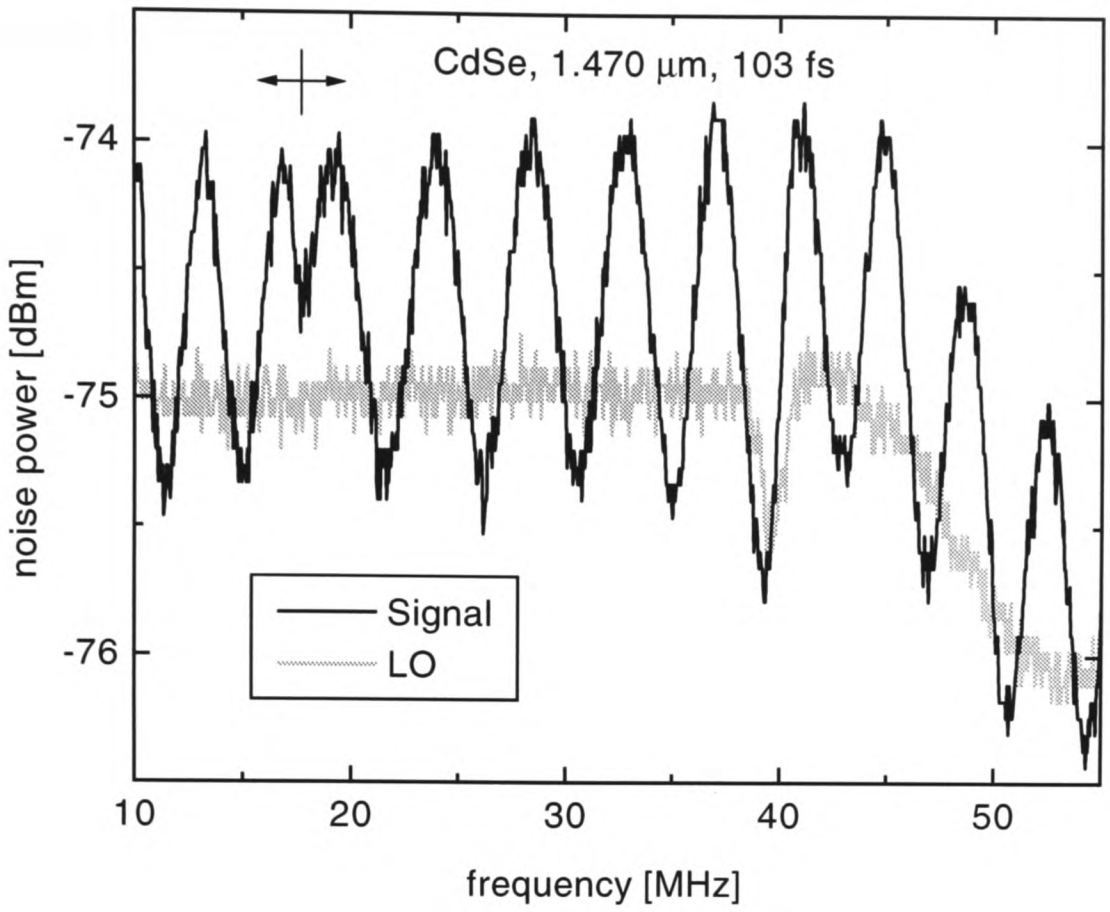

Figure 6.2: Frequency dependence of the LO noise power and the squeezed light signal between 10 and 55 MHz with 3 MHz resolution. The peak pump intensity was 1.3 GWcm^{-2}. The grey line shows the result with the signal port of the homodyne detector blocked (the dip at 40.5 MHz is caused by the repetition rate). The black line shows the equivalent trace with the squeezed light incident at the signal port. The double arrow indicates a reversal in the direction of the LO phase sweep.

It is evident that squeezing is obtained throughout the entire frequency range studied, except near 40.5 MHz. We detect squeezing of 0.4 dB (9%) below the shot noise level, whereas the maximum noise power rises to 0.9 dB above the LO noise. When allowance is made for the linear losses in the optics, the 88% efficiency of the photodiodes, and the measured interferometric overlap factor between the LO and the squeezed vacuum (less than 70%, leading to a reduction of the detection efficiency of about 50%, cf. §§ 4.3.1), we estimate that the total detection efficiency is 40% at best. This implies that the actual degree of squeezing is at least 1.1 dB (22%).

We also tested for the dependence of the squeezing on rotation of the sample about the c axis. In contrast with the experiments in cubic crystals studied previously [9], the squeezing in hexagonal CdSe does not show any angular dependence. As expected for a hexagonal material there is no anisotropy of the effective nonlinear susceptibility for four-wave mixing $\chi^{(3)}_{\text{eff}}$ for propagation along the c axis (cf. §§ 3.3.2). Furthermore, there is no induced birefringence along this axis, and hence $\chi^{(3)}_{\text{eff}}$ is independent of the polarisation [60].

6.3.1 Intensity and wavelength dependence

Making use of the tunability of the OPO we have investigated the wavelength as well as the pump intensity dependence of the squeezing. Fig. 6.3 shows the dependence of the minima and the maxima of the phase-dependent noise at 24 MHz versus the peak intensity of the pump pulse for a series of wavelengths from 1.419 to 1.543 μm. Note that 1.417 μm corresponds to a photon of half the bandgap energy and that the bandwidth of the pulses is greater than 20 nm. At all the wavelengths investigated a strikingly similar pattern is observed for both the minima and the maxima, apart from the case of 1.419 μm, where the pulse spectrum extends above halfgap into the region of strong two-photon absorption. The maxima show saturation at peak intensities that increase at longer wavelengths (at the longest wavelengths used the expected saturation intensity is not accessible in our experiment). This behaviour can be explained by a deterioration of the overlap factor as the intensity is increased: The pump undergoes SPM (producing a nonlinear phase shift of $\approx \pi$ at the saturation intensities), whereas the squeezed light is generated by XPM, so there is a substantial difference in the nonlinear phase shift of the two. In addition, two- and three-photon absorption affects the two components differently. These differences affect the temporal as well as the spectral overlap (cf. autocorrelations and spectra in the previous chapter) of the squeezed vacuum with the

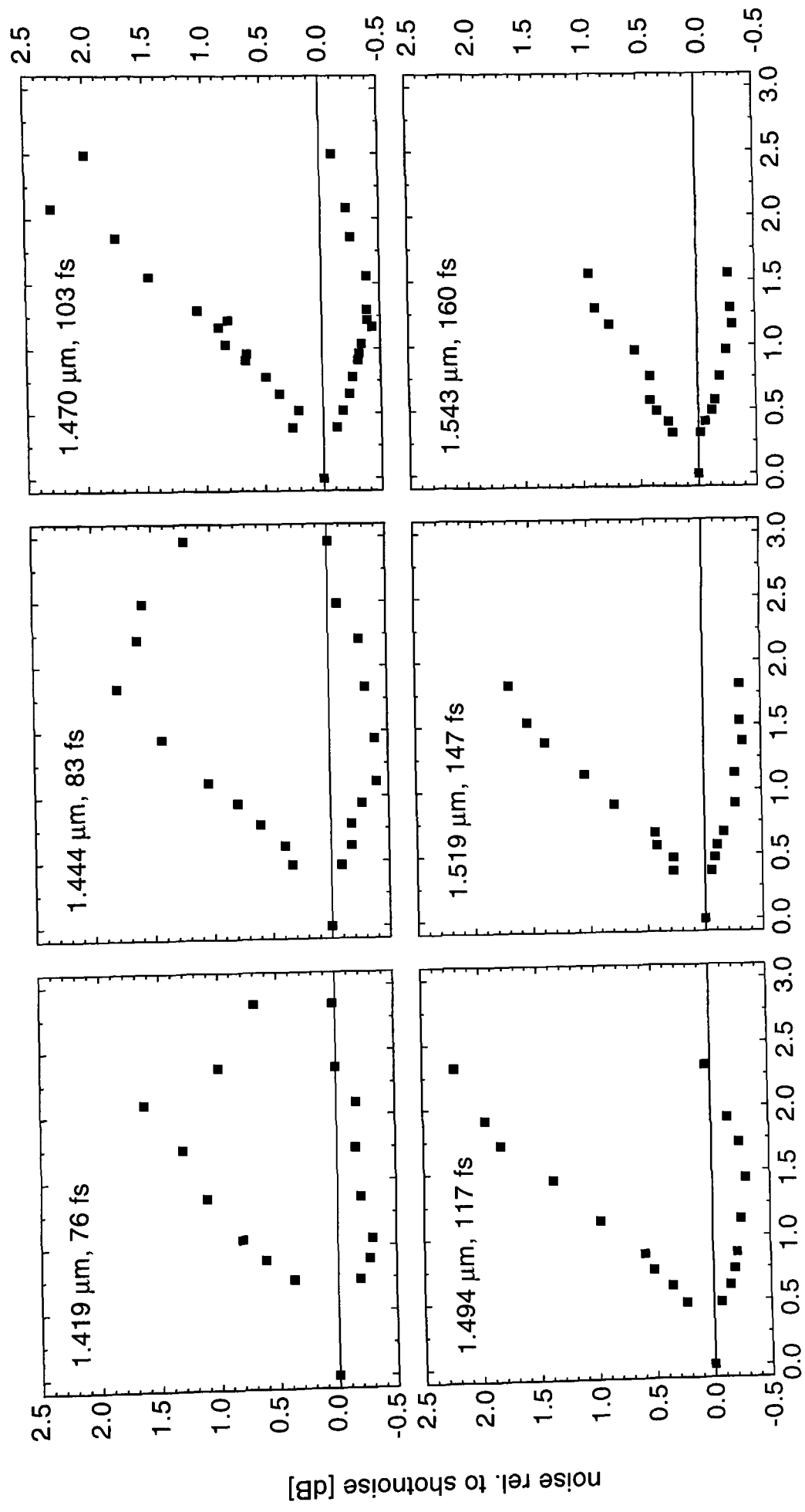

Figure 6.3: Maxima and minima of the phase-dependent noise at 24 MHz versus the peak pump intensity for different wavelengths, normalised to the shot noise power. The measurement error is of the order of ± 0.1 dB

LO leading to a saturation and subsequent reduction of the detectivity. The observed shift towards higher saturation intensities with increasing wavelength is consistent with this explanation.

The minima (i.e. the squeezing) also exhibit a saturation, but at a substantially lower peak intensity ($\approx$1.3 GWcm^{-2}, inducing a nonlinear phase shift of $\sim \pi/2$ in the pump pulses). At still higher intensity the squeezing decreases again. Unlike the maxima, the minima do not show a wavelength dependence within our measurement accuracy, which indicates that this saturation is caused not by the diminishing overlap factor but by an effective increase of the total noise above the minimum uncertainty limit.

6.3.2 Alternative local oscillator arrangement

We have also investigated an alternative LO arrangement by using the unmodified pump pulses as the LO. For this experiment, the setup shown in Fig. 6.1 had to be modified. The LO beam was now split off from the pump beam before the sample. The pump beam passed through the sample in the same way as in the other experiments. After the sample the pump beam was dumped using a PBS. The emerging squeezed vacuum was joined with the LO in a further PBS and subsequently analysed in the homodyne detector. Again, the polarisation optics had to be aligned carefully to minimise the background signal. However, the overall detectivity in this scheme is reduced to only about 20% due to the diminished interferometric overlap of the LO with the squeezed vacuum ($\lessapprox$ 50%, as opposed to $\lessapprox$ 70% with the previous LO configuration) [92, 53].

The results for 1.444 μm are shown in Fig. 6.4. The overall pattern is the same as that obtained in the other configuration. Namely, the maximum squeezing is obtained at a similar intensity level and the antisqueezing component continues to rise after saturation of the squeezing. Allowing for the reduced detectivity, the maximum squeezing is the same as that obtained using the recycled pump as a LO. This adds further support to

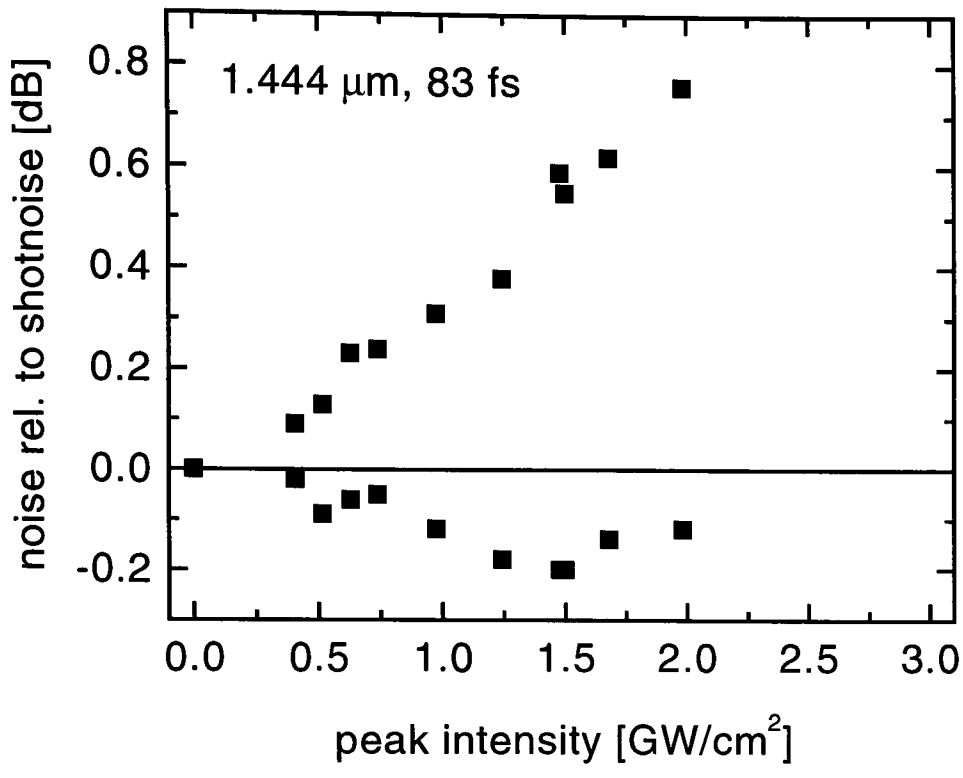

Figure 6.4: Maxima and minima of the phase-dependent noise at 24 MHz versus the peak pump intensity for 1.444 μm, measured with the unmodified pump pulse as the LO and normalised to the shot noise level. The measurement error is of the order of ± 0.1 dB

the conclusion that the saturation is in fact caused by an additional noise source rather than by the details of the LO configuration.

6.3.3 Discussion

In Fig. 6.5 we compare the squeezing measured at 1.470 μm with a simple model for squeezing by four-wave mixing, which includes the effect of inefficient detection, characterised by an effective efficiency η, but disregards nonlinearities other than 4WM as well as loss mechanisms. This model gives the following form for the dependence of the minima S_{min} and maxima S_{max} of the phase-dependent noise on the nonlinear phase shift $\Delta\Phi$ [93, 80, 17]:

$$S_{\substack{\mathrm{max}\\ \mathrm{min}}} = 1 - \eta(1 - e^{\pm\Delta\Phi}). \tag{6.1}$$

The solid lines plotted in Fig. 6.5 show the predictions of (6.1) with $\eta = 0.4$. With the assumption $\chi^{(3)}_{xxyy} = \chi^{(3)}_{xxxx}/3$ (cf. §§ 3.3.2, we take 1/3 of the phase shift measured in the autocorrelation experiments in § 5.4). We see that the agreement between the predicted and the measured squeezing is reasonable up to the saturation intensity of about

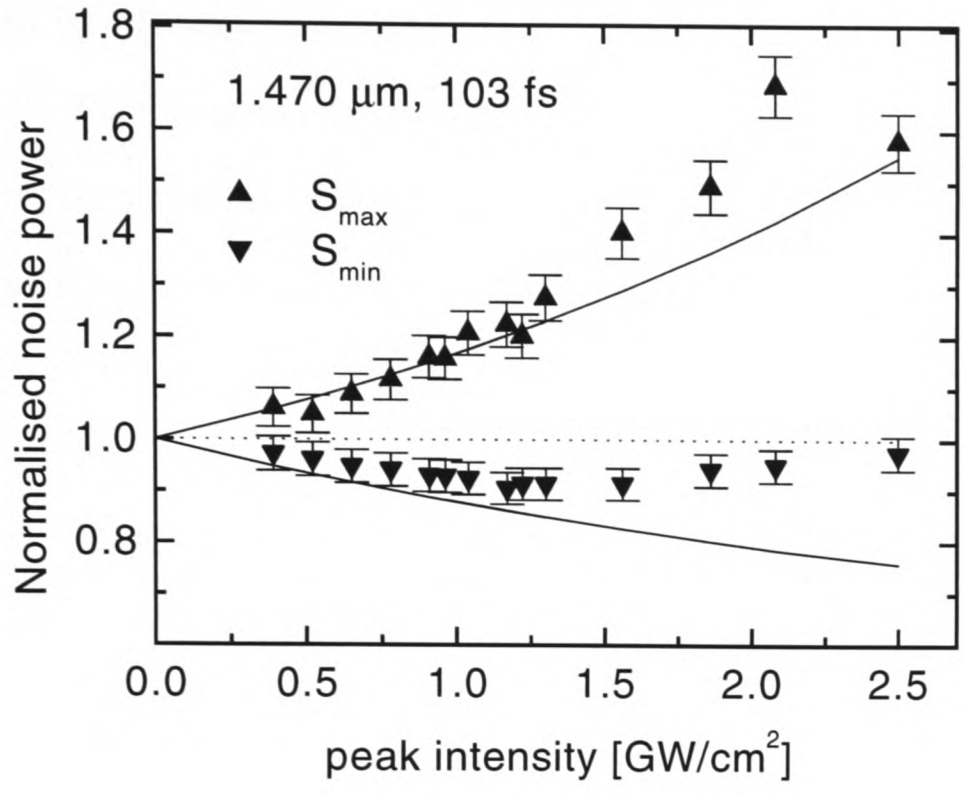

Figure 6.5: Maxima and minima of the phase-dependent noise at 24 MHz versus peak intensity at 1.470 μm. The noise powers have been normalised to the shot noise level. The solid lines show the predictions of the simple model discussed in the main text.

1.2 GWcm^{-2}. It is equally interesting to compare the predicted and the measured values for the antisqueezing phase. Again they agree reasonably well up to about 1.2 GWcm^{-2}. This confirms that above this intensity the light is no longer in a minimum uncertainty state.

As multi-photon absorption would force both the squeezing and the antisqueezing towards the shot noise level [94], and as the overall transmission is still greater than 80%, multi-photon absorption can be discounted as the main source of this increase in total noise. The weak wavelength dependence points to a wavelength-independent noise source with a relatively sharp onset as a function of peak intensity. With the spectrally broad ultrashort pulses used, a possible cause of the increase in total noise is stimulated Raman scattering. This effect was identified as a noise source for femtosecond squeezing in optical fibres, both theoretically [95, 96] and experimentally [61, 62, 36]. As we have seen in § 5.6, stimulated Raman scattering shows up strongly in the transmission spectra. Further work will be needed to confirm this possibility. However, the phase-integrated photon-number noise in our experiment is still far lower than that observed in comparable femtosecond experiments at 1.55 μm in optical fibres [61, 62] where an excess noise of up

to 20 dB was observed.

The intensity dependence of the squeezing at 1.470 μm in CdSe can be compared directly to earlier measurements at 960 nm in ZnSe [9], as both experiments were performed at photon energies of $\approx 0.48E_G$. In accordance with the $n_0 E_G^{-4}$ dependence of the nonlinear refractive index [49], maximum squeezing in CdSe is obtained at peak intensities that are lower by a factor of ≈ 6 than the ones required in ZnSe. The reduction of squeezing at still-higher intensity was not seen in the ZnSe measurements, which probably was due to the limited power range that was accessible.

6.4 Feasibility of extending the XPM-technique to waveguides

In a further experiment we have studied the feasibility of extending the XPM-technique to an AlGaAs waveguide. Due to the reduced cross-sectional area of waveguides and their increased nonlinear interaction length, it should be possible to achieve squeezing at substantially lower peak powers than in bulk material. Furthermore by using $Al_xGa_{1-x}As$, waveguides can be optimised for operation at 1.55 μm by varying the aluminium content. Waveguides could therefore be an important building block towards the construction of integrated sources of squeezed light. Theoretical studies predicted as much as 85% (8.2 dB) of quadrature squeezing to be obtainable by this technique [53].

The waveguide sample consisted of a 1 μm thick high-index waveguiding layer, composed of $Al_{0.21}Ga_{0.79}As$ and grown on a 4 μm thick $Al_{0.4}Ga_{0.6}As$ cladding layer. A 1.5 μm thick and 4–6 μm wide $Al_{0.3}Ga_{0.7}As$ rib etched on top provides the lateral confinement. This results in a calculated active area of about 6 μm^2 [97]. The sample was 2 mm long and both faces were anti-reflection coated. For a more detailed description of the sample see Appendix A.1.

6.4.1 Self-phase modulation

We first assessed the waveguide for its suitability to the XPM-squeezing technique by characterising the SPM of the transmitted pulses.[1]

Fig. 6.6 shows the spectra for various optical powers and wavelengths. As in the case of CdSe (cf. Chapter 5) we observed a maximum phase shift of $\simeq \pi$, but, due to the smaller effective area of the waveguide at output powers of only 7–9 mW (corresponding powers in the case of CdSe were about 150 mW). Again as in the case of CdSe, we see a strong asymmetry of the spectra at high powers. The asymmetry is strongest close to halfgap, where two-photon absorption starts to play a significant role. In addition, stimulated Raman and free carrier absorption influence this spectral asymmetry.

Another interesting comparison lies in the temporal behaviour, as shown by the interferometric autocorrelations in Fig. 6.7. The Figure shows a pulse of a duration of about 200 fs both at the input and at the output of the waveguide. We observe a significant amount of nonlinear chirping, in line with the equivalent measurements in CdSe, again at greatly reduced optical power. It was therefore not possible to resolve the individual fringes of the interferometric autocorrelation as in the case of CdSe. The envelopes, however, could be clearly measured. Again we deduced a maximum phase shift of $\simeq \pi$.

This amount of nonlinear phase shift has proved to be sufficient for the production of squeezed light in the previous XPM-experiments in CdSe (cf. above) and ZnSe [9].

6.4.2 XPM-squeezing

We then attempted to generate squeezed light using a similar setup to the one used above in §§ 6.3.2, i.e. with an external LO. A number of reasons prevented the experiment from

[1]These measurements were done before the OPO was properly characterised and while its operation was still fairly unstable. Thus we do not attempt to give adequate estimates of the peak intensity produced, but only give the actual optical powers measured.

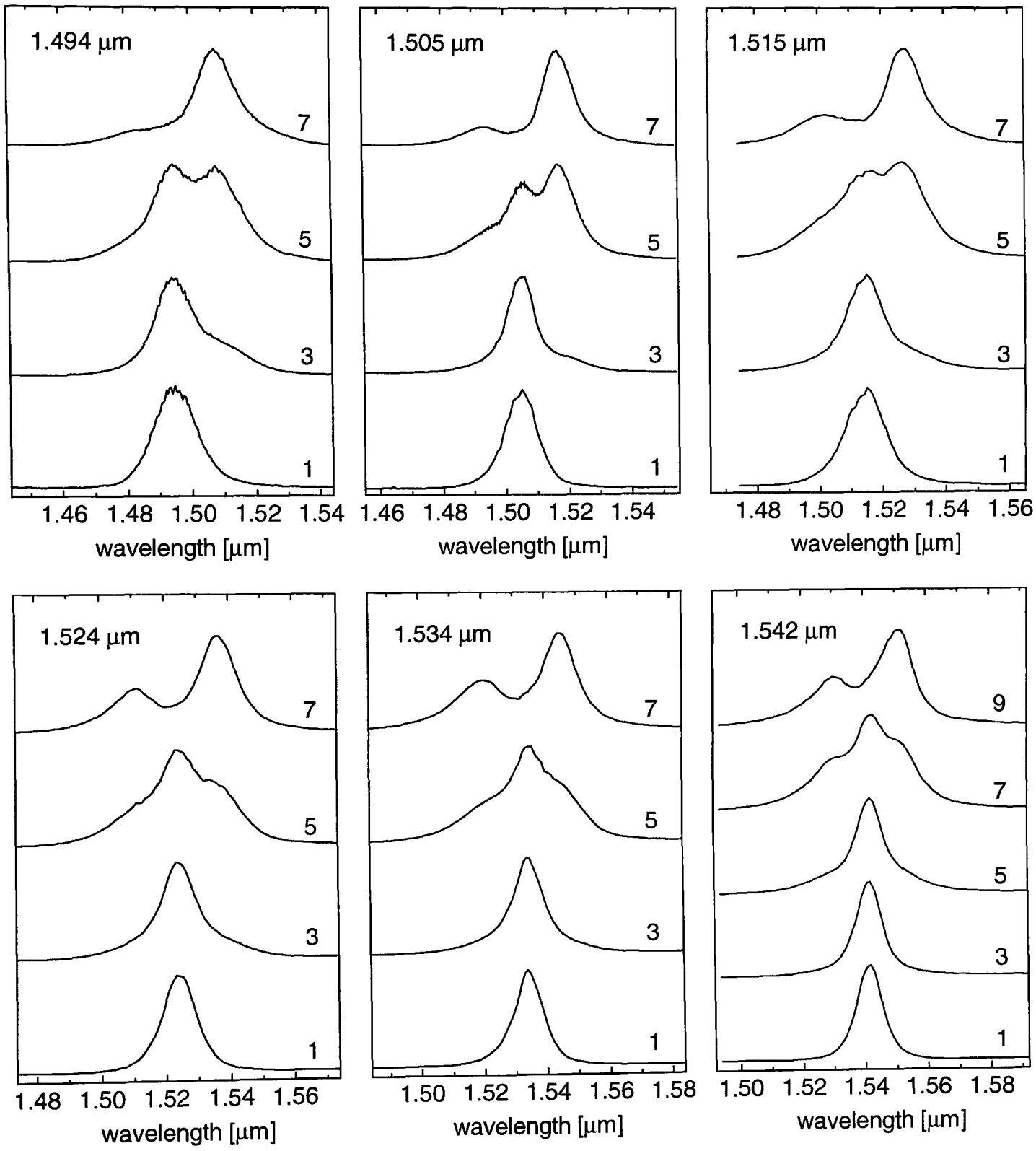

Figure 6.6: Power dependence of output spectra from the AlGaAs waveguide for different wavelengths. The numbers to the right of each curve denote output power in mW. At the maximum powers we deduced a nonlinear phase shift of $\simeq \pi$. The spectra also show a significant asymmetry, strongest at short wavelengths, i.e. close to halfgap.

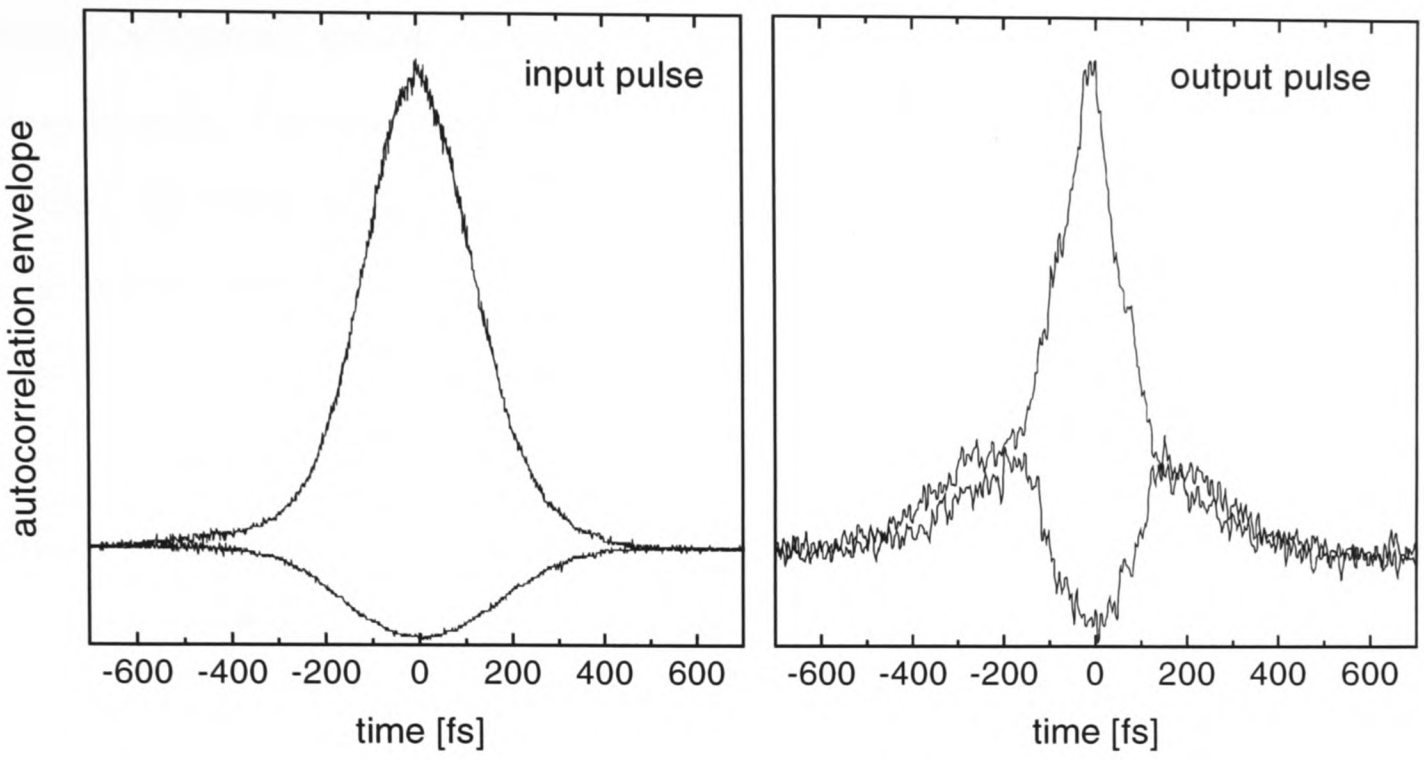

Figure 6.7: Envelope of interferometric autocorrelations of an input pulse of about 200 fs duration, at a centre wavelength of 1.542 μm (left) and the corresponding transmitted pulse (right) at 9 mW output power. The transmitted pulse shows a strong nonlinear chirp.

succeeding. A significant birefringence was identified as the main cause. It amounted to about $n_{\mathrm{TE}} - n_{\mathrm{TM}} = +0.001$, corresponding to a phase difference of $\frac{5}{2}\pi$ over the sample length of 2 mm.

The birefringence needs to be significantly reduced in order to produce squeezed light in this system. This could be achieved by compensating the inherent waveguide birefringence with stress induced effects by appropriate etching [98]. Alternatively, the waveguide could be built within a *p-i-n* junction, so that strong electric fields could be used to compensate for the birefringence electro-optically. In addition, the waveguide should only allow a single mode and have low losses.

Because the detection efficiency depends on the square of the fringe visibility in the detection interferometer (cf. §§ 4.3.1), mode-matching between the LO and the squeezed vacuum is another important issue. As the output beam shape of a rectangular waveguide

is strongly elliptical, spatial mode-matching is difficult to achieve if an external local oscillator is used. The best mode-matching we obtained led to a fringe visibility of about 50%. Our attempts using cylindrical lenses did not yield a significant improvement. Alternatively an anamorphic prism pair could be used, but it would have to be matched accurately.

A more promising approach is to use the recycled pump as a LO, as in the CdSe experiment above. As the pump powers are much lower for waveguides than they are for the experiments in bulk, the system would have to be operated at significantly lower LO-powers. This, however, would require an improved signal-to-noise ratio in the detection system.[2] Using the internal LO has the additional advantage of providing better temporal mode-matching [53]. Combined with the difficulties of the spatial mode-matching, we believe that an external LO scheme using compressed pulses as proposed by Ho *et al.* [53] would be impractical.

If these two problems, i.e. birefringence and mode-matching, can be brought under control, waveguides seem to provide ideal circumstances to exploit the XPM-squeezing technique. Apart from their potential for integration, the waveguides would also provide an ideal system to study the limitations to XPM-squeezing observed in the bulk experiments. Because of the reduced peak powers needed, longer pulses could be employed, for which, due to their decreased bandwidth, the influence of stimulated Raman scattering is reduced.

6.5 Conclusions and outlook

- We have produced femtosecond-pulsed quadrature squeezing in a straightforward single-pass experiment using cross-phase modulation in a hexagonal CdSe crystal

[2] By using transimpedance amplifiers in the detection system the signal-to-noise ratio could be increased considerably from the present configuration.

at ≈ 1.5 μm.

- Maximum squeezing of 0.4 dB (1.1 dB is inferred at the crystal) is measured at 1.444 μm and at 1.470 μm.

- We have measured the wavelengths dependence of the squeezing between 1.419 and 1.543 μm as well as its intensity dependence.

- Above a peak intensity of about 1.2 GWcm^{-2} the squeezing saturates and the total photon-number noise exceeds the minimum uncertainty limit.

- The same behaviour is seen for two distinct local oscillator configurations. One configuration uses the recycled pump beam as the LO, the other uses an unmodified input pulse.

- We propose stimulated Raman scattering as the most likely cause for this increased total noise at high intensities.

- Similar experiments in an AlGaAs waveguide were as yet not successful. The problems encountered are discussed and possible solutions are proposed.

To obtain further clarity on the reasons for the saturation of the squeezing, the temperature dependence of the squeezing would add useful information. It would also be interesting to investigate the behaviour of the squeezing with increasing pulse duration to reduce the effect of the stimulated Raman scattering. Suitable waveguides could provide an ideal system to study these effects.

Chapter 7

Photon-number squeezing by multi-photon absorption

Contents

7.1 Introduction 86

7.2 Experimental setup 88

7.3 Experimental results for AlGaAs-waveguide 89

7.4 Theoretical considerations 92

7.5 MPA-squeezing in organic semiconductor 96

7.6 Conclusions and outlook 100

7.1 Introduction

Since the original demonstration of the sub-Poissonian nature of resonance fluorescence by Short and Mandel [31], a number of different methods for the generation of photon-number squeezed light have been demonstrated. For example, photon-number squeezing was observed in constant-current driven semiconductor lasers [37] and light-emitting diodes [4], it has been observed in second-harmonic generation (SHG), both in the fundamental [32] and in the frequency-doubled light [33], as well as in parametric deamplification [34]. Most recently Friberg *et al.* have demonstrated soliton photon-number squeezing by spectral filtering in optical fibres [35].

However, one of the most conceptually direct methods of reducing photon-number fluctuations in a light beam is that of two-photon absorption (2PA), which gave rise to the earliest theoretical predictions of squeezed state generation [14, 15, 99, 100]. This squeezing mechanism is qualitatively different in that the quantum states are produced by an *incoherent* light-matter interaction. In this chapter we present the first experimental demonstration of photon-number squeezing by multi-photon absorption (MPA). Here we will describe results obtained using femtosecond pulses in a straightforward travelling wave geometry through a semiconductor optical waveguide. We also show the generality of the effect, by demonstrating the same mechanism to produce squeezing in the organic semiconductor p-toluene sulphonate polydiacetylene (PTS-PDA). This latter experiment constitutes the first experimental demonstration of squeezed light generation in any organic material.

The sub-Poissonian nature of photon-number fluctuations in a beam of light undergoing MPA can easily be understood using a qualitative photon-statistical argument: bunched photons are more likely to be absorbed, and so the absorber acts as a filter preferentially transmitting antibunched photons. The filter becomes increasingly selective as the order of the absorption process increases. Over 30 years ago Y. R. Shen [101] was

the first to raise the issue of the photon statistics being influenced by 2PA. Squeezing by 2PA was first predicted in 1974 [14, 15], and subsequently extended to the general case of k-photon absorption [99]. Closely related are the investigations of quadrature squeezing by 2PA initiated by Loudon [100]. However, the experimental implementation has been prevented so far by the high intensity required to obtain sufficient nonlinear absorption. To obtain the necessary amount of nonlinear absorption without the detrimental effects of linear absorption, we chose an AlGaAs semiconductor waveguide as the nonlinear medium because of its extended interaction length and worked at energies far below the linear absorption edge of the material. Large nonlinear effects were obtained by using femtosecond pulses with a photon energy tunable through the half-bandgap energy which allowed us to select two- or three-photon absorption. To extend the technique to organic semiconductors, PTS-PDA was chosen, as it has one of the largest known optical nonlinearities of any material.

In § 7.2 we describe the experimental setup. In § 7.3 the experimental results for the AlGaAs waveguide are presented, demonstrating the relation between nonlinear absorption and photon-number squeezing. Squeezing by two- and three-photon absorption can be distinguished clearly. We found good agreement with longstanding theoretical predictions, which are described in § 7.4. § 7.4 also contains a discussion of the influence of using pulsed light in such experiments. In § 7.5 we describe the extension of the technique to the organic semiconductor PTS-PDA which led to the first experimental observation of squeezing in an organic material, and confirmed the generality of squeezing by multi-photon absorption. § 7.6 concludes the chapter and gives an outlook on the wide variety of opportunities this new technique might entail.

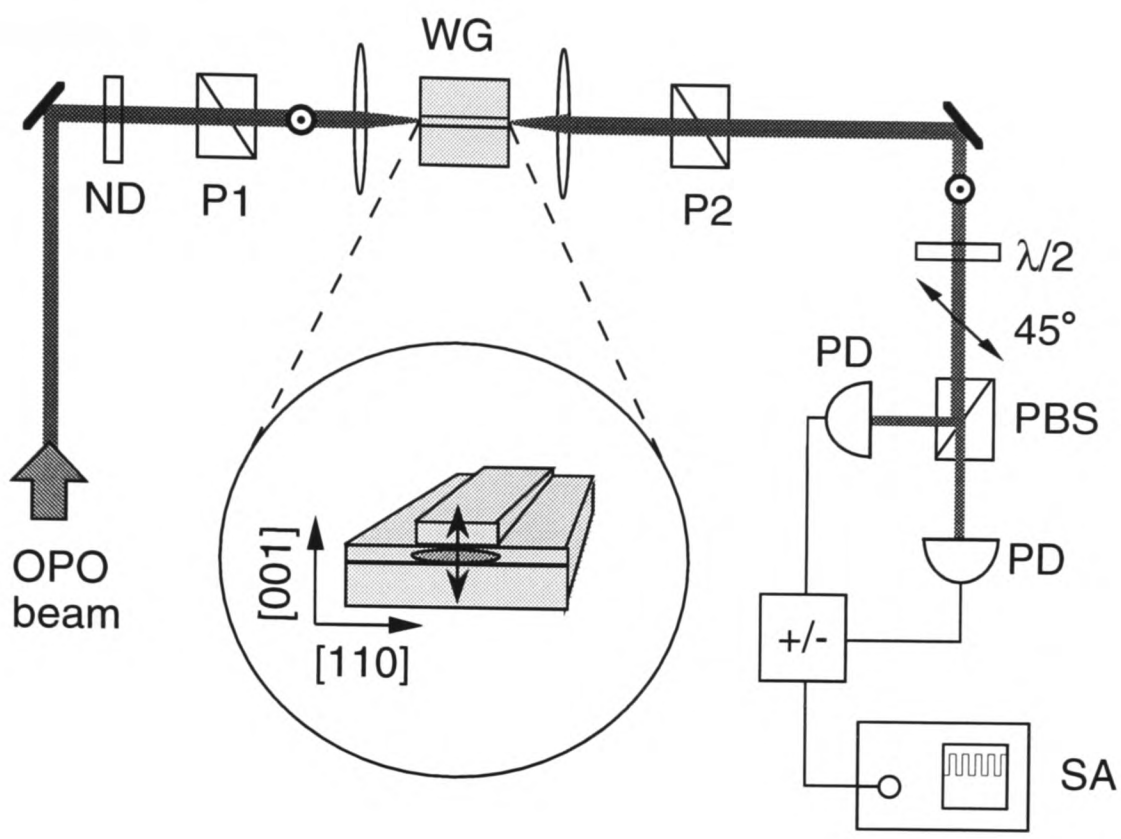

Figure 7.1: Experimental arrangement for multi-photon absorption squeezing: ND, attenuator; P1, P2, polarisers; WG, waveguide; $\lambda/2$, half-wave plate; PBS, polarising beam splitter; PD's, photodiodes; SA, spectrum analyser. The inset shows the geometry and the orientation of the waveguide.

7.2 Experimental setup

The waveguide sample consisted of a 1 μm thick, high index waveguiding layer, composed of $Al_{0.21}Ga_{0.79}As$ on a $Al_{0.4}Ga_{0.6}As$ cladding layer, grown on a [001]-GaAs-substrate. A 1.5 μm thick and 5 μm wide $Al_{0.3}Ga_{0.7}As$ rib on top provided the lateral confinement (see Appendix A.1 for a schematic of the sample). The calculated effective area is about 6 μm^2. The sample described here was 2 mm long and both faces were anti-reflection coated. Photoluminescence measurements confirmed the expected core bandgap energy of 1.69 eV (corresponding to a halfgap resonance wavelength of 1.47 μm). Linear losses were small (0.7 dB/cm $\pm$0.5 dB/cm) [97].

Fig. 7.1 shows the experimental setup. The source was an optical parametric oscillator (OPO) pumped by a modelocked Ti:Sapphire laser and tunable from 1.45 to 1.55 μm

at 81 MHz repetition frequency (cf. §§ 4.1.3). The pulse width varied from 75 to 160 fs, depending on the wavelength λ. The light was polarised along the [001] direction of the crystal (i.e. in a TM mode) and coupled into and out of the waveguide using microscope objectives. The emerging beam was passed through a polariser (P2) to ensure that only TM light was detected. The beam was subsequently analysed using a direct balanced detection system with two InGaAs *p-i-n*-photodiodes (EG&G C30641). Balancing was obtained by combining a half-wave plate ($\lambda/2$) and a polarising beam splitter (PBS) to form a 50/50 beam splitter. The photocurrents from the two detectors were separately amplified and then added or subtracted using a RF-hybrid junction. The sum and the difference photocurrent noise powers were then measured using a RF-spectrum analyser. The sum photocurrent noise power measures the total photon-number fluctuations, whereas the difference noise power provides the shot noise calibration (cf. §§ 4.3.2 for the details of the electronics in use). The common mode rejection ratio was better than 20 dB. We confirmed that the OPO beam was at the shot noise limit by ensuring that the sum and difference photocurrent noise powers were identical when the sample was removed, as well as by comparison to a known shot noise limited source (a blackbody emitter).

7.3 Experimental results for AlGaAs-waveguide

7.3.1 Nonlinear transmission

We first measured the nonlinear transmission through the sample. Care had to be taken that the adjustment of the input power did not influence the coupling efficiency into the waveguide. Coupling was therefore reoptimised for each individual input power. The results for different wavelengths are shown in Fig. 7.2. There is a clear qualitative difference in the behaviour of the nonlinear transmission above (1.45 μm) and below

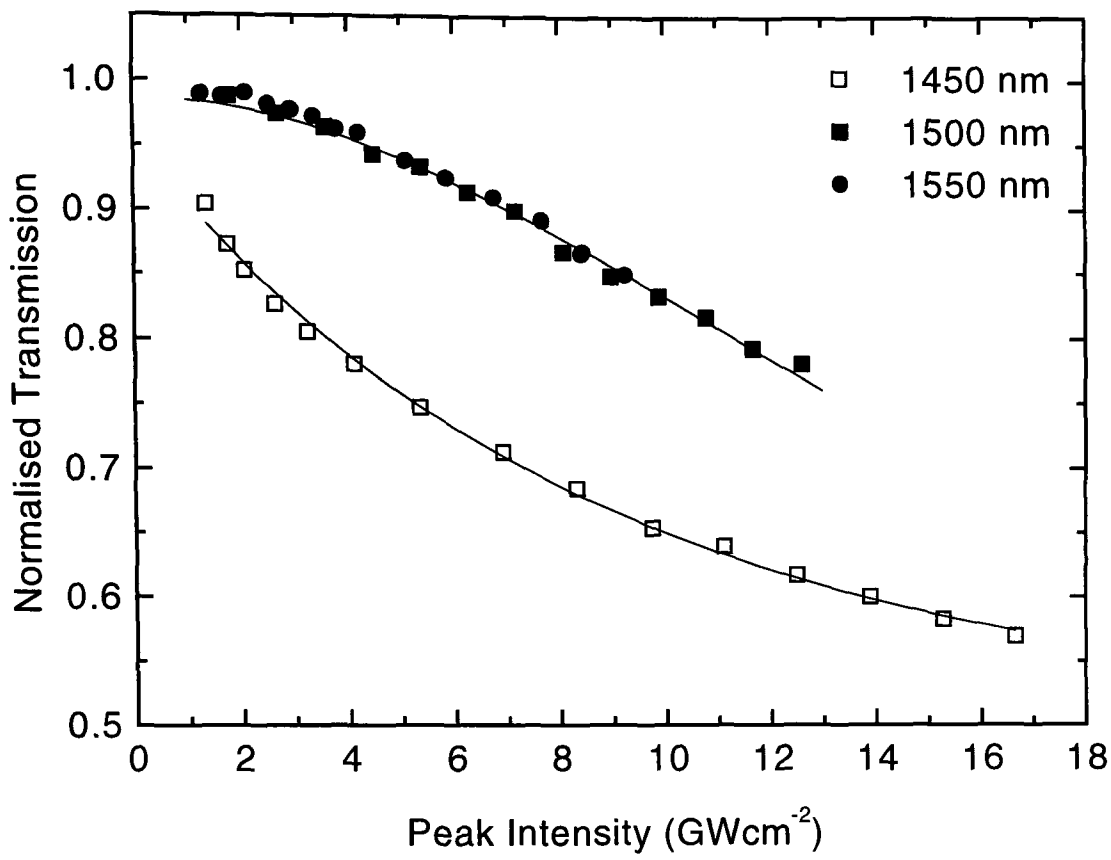

Figure 7.2: Nonlinear transmission as a function of input intensity for different wavelengths. The lines are best fits for pure 2PA at 1.45 μm and for pure 3PA at the longer wavelengths.

(1.50 μm and 1.55 μm) the halfgap energy ($\hat{=}$1.47 μm).

The propagation equation for the intensity $I(z)$ of the beam travelling through the sample is

$$\frac{dI}{dz} = -\left[\alpha_1(\lambda) + \alpha_2(\lambda)I + \alpha_3(\lambda)I^2\right] I, \tag{7.1}$$

where α_1, α_2 and α_3 represent the coefficients for linear absorption, two-photon absorption (2PA) and three-photon absorption (3PA), respectively. Integrating (7.1) for the cases of either pure 2PA or pure 3PA shows that pure 2PA leads to a positive initial curvature of the transmission curve, whereas 3PA leads to a negative initial curvature. The lines in Fig. 7.2 show the best fits to the data using a pure 2PA fitting function for 1.45 μm and a pure 3PA fitting function for the longer wavelengths. The 2PA fitting function at 1.45 μm includes the effect of self-phase modulation spectrally broadening the pulses (cf. §§ 6.4.1) into the energy region below halfgap, leading to a small reduc-

tion in the predicted 2PA with increasing power. The values of $\alpha_2 = 0.2$ cmGW^{-1} at 1.45 μm and of $\alpha_3 = 0.01$ cm^{3}GW^{-2} at 1.50 μm and 1.55 μm correspond well with the values found for TM-modes in similar AlGaAs waveguides [77].

Considering that harmonic generation with subsequent linear absorption of the generated light could lead to a similar effect on the photon statistics, we have to ensure that MPA is the dominant loss mechanism. We therefore investigated the emission from the sample at the relevant wavelengths. We observed only pure bandgap luminescence and found the expected quadratic and cubic power dependence for the 2PA- and the 3PA-case, respectively. SHG is forbidden for TM-modes in the chosen crystal geometry [77] and was indeed not observed even when the energy of the frequency-doubled light would have been below the bandgap energy. No third-harmonic generation (THG) was observed. Due to the short absorption length ($\simeq$100 nm) [102] of the frequency tripled light in the waveguide, most of this light would be reabsorbed. From our measurement sensitivity, however, we can infer an upper limit of 1% of the nonlinear losses to be caused by THG, which can therefore be regarded as negligible.

7.3.2 Squeezing

Fig. 7.3 shows the squeezing results (expressed in terms of the Fano factor F, which is the ratio of the measured noise to the shot noise) as a function of normalised transmission for the different wavelengths. As with the nonlinear transmission data, we find a striking difference between the 2PA- and the 3PA-behaviour. As expected intuitively, 3PA leads to stronger squeezing for the same transmission. The maximum measured squeezing is 11% (0.5 dB) and occurs for the 3PA case at 1500 nm, with a normalised transmission of 0.77 and a peak intensity of 12 GWcm^{-2}. When allowance is made for linear losses in the optics ($\simeq$20% measured), and the 85% quantum efficiency of the photodetectors, we estimate that the total detection efficiency is $\eta_{\text{det}} = 0.68$ at best. Correcting for these

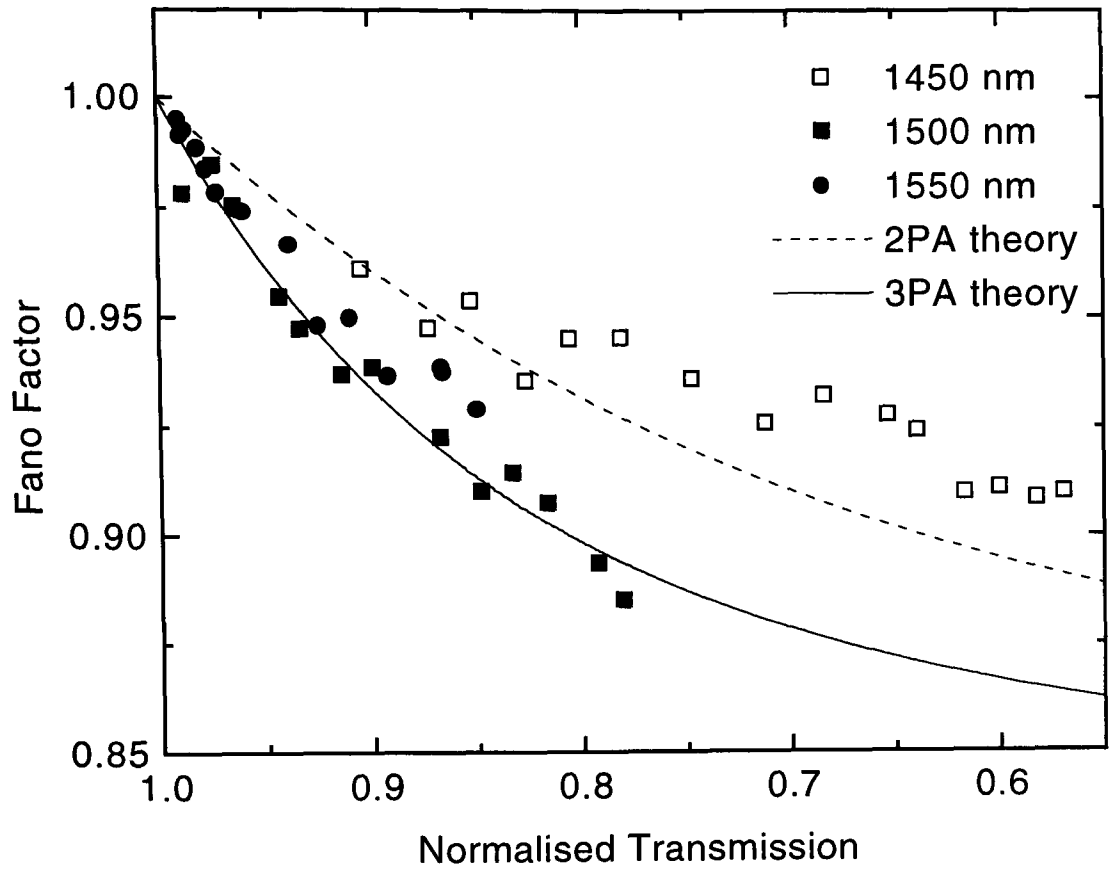

Figure 7.3: Fano-factor as a function of nonlinear transmission for different wavelengths. The lines are the results obtained from the model described in the text for 2PA (dashed line) and 3PA (solid line), both evaluated for an effective detection efficiency of 45%. The measured data for 1.45 μm follows the model for the 2PA, whereas the longer wavelengths (1.50 μm, 1.55 μm) follow the 3PA-model.

losses we can infer a maximum squeezing of 16% (0.8 dB) by 3PA.

For the 2PA-case at 1450 nm the maximum squeezing is 9% (0.4 dB), but now at the substantially lower normalised transmission of 0.6 and at an intensity of 12 GWcm^{-2}. Allowing for the detection efficiency, this implies 13% (0.7 dB) squeezing by 2PA.

7.4 Theoretical considerations

For the theoretical treatment, consider a coupled system of field and N non-interacting two-level atoms. An atom makes a transition from the state $|1\rangle$ to the state $|2\rangle$ by ab-

sorbing k photons, one in each of the modes $m_1, m_2, \ldots m_k$. The interaction Hamiltonian is then [101]

$$H_I = \sum_{i=1}^{N} \left\{ \eta_k \hat{c}_{2i}^{\dagger} \hat{c}_{1i} \hat{\mathbf{E}}_{m_1}^{\dagger}(\mathbf{r}_i) \cdots \hat{\mathbf{E}}_{m_k}^{\dagger}(\mathbf{r}_i) + \text{H.c.} \right\}, \tag{7.2}$$

where $\hat{c}_{1i}, \hat{c}_{2i}, \hat{c}_{1i}^{\dagger}$, and $\hat{c}_{2i}^{\dagger}$ are the annihilation and creation operators for the ith atom in the ground state $|1_i\rangle$ and the excited state $|2_i\rangle$. η_k is the matrix element for k-photon absorption and $\hat{\mathbf{E}}_{m_i}^{\dagger}(\mathbf{r}_i)$ is the positive frequency part of the electric field at the ith atom which is proportional to the mode function of the m_i-th mode at the position $\mathbf{r}_i$ and to the photon annihilation operator $\hat{a}_{m_i}$ [101, 103]. By means of projection techniques from this interaction Hamiltonian [14] and for the limit of large mean photon numbers $\bar{n}$ and unsaturated absorption, Paul *et al.* [99] find the following equation of motion for the probability p_n of n photons being present:

$$\frac{\mathrm{d}p_n}{\mathrm{d}t} = -\gamma_k \left[\frac{n!}{(n-k)!} p_n - \frac{(n+k)!}{n!} p_{n+k} \right], \tag{7.3}$$

where γ_k is the k-photon absorption rate which contains the details of the light-matter interaction. Noting that the probability for k photons being absorbed simultaneously from an n-photon state is proportional to $n(n-1)\cdots(n-(k-1))$, we can easily interpret (7.3) as a set of rate equations. As time evolves, k-photon absorption lowers the mean photon number of the system $\bar{n}(t)$, leading to a transmission $T = \bar{n}(t)/\bar{n}(0)$ and the characteristics of the distribution p are modified. From (7.3) Paul *et al.* [99] found the following expression for the Fano factor $F_k(T)$ for squeezing by k-photon absorption as a function of T:

$$F_k(T) = \left(F_0 - \frac{k}{2k-1} \right) T^{2k-1} + \frac{k}{2k-1}, \tag{7.4}$$

where F_0 is the Fano factor at the input ($F_0 = 1$ in the case of a coherent input). The noise suppression through k-photon absorption is therefore limited to $F_k \geq k/(2k-1)$,

i.e. to 2/3 for 2PA, and to 3/5 for 3PA. For $k \gg 1$, the minimum F_k becomes 1/2. The absolute limit for photon-number squeezing by higher order MPA is therefore 50%.

(7.4) is valid for cw light and its results have therefore to be corrected to account for the use of pulsed light. We applied the following correction formula from the cw Fano factor F_{cw} to the Fano factor for modelocked pulsed light F_p:

$$F_p(T) = N \int_{-\infty}^{+\infty} F_{cw}\left\{T\left[I(t)\right]\right\} \operatorname{sech}^2 t \, dt, \tag{7.5}$$

where t_0 is the pulse width, $I(t) = I_0 \operatorname{sech}^2 t$ is the temporal intensity profile of a modelocked pulse with a peak intensity of I_0 and $N = 1/\int_{-\infty}^{+\infty} \operatorname{sech}^2 t \, dt$ the normalisation factor. Note that for a given pulse shape, (7.5) has the same effect on the averaged Fano factor irrespective of its duration.

The lines in Fig. 7.3 are the theoretical predictions of this model, corrected for the same effective efficiency $\eta_{\text{eff}} = 0.45$ for both the 2PA- and the 3PA-case. We see a good agreement for both cases, but the effective efficiency is somewhat lower than the estimated detection efficiency $\eta_{\text{det}} = 0.68$. Considering that the model only takes into account the basic process of MPA, but completely neglects competing nonlinear processes, the agreement is remarkable. A detailed quantitative study would have to include a number of additional effects, such as self-phase modulation, stimulated Raman scattering, spontaneous emission, as well as free-carrier effects, which can produce additional noise or attenuation.

It is interesting to investigate the effect of using pulsed light in more detail, as in practice only pulsed light makes it possible to achieve the peak intensity necessary to obtain significant squeezing by MPA. Fig. 7.4 shows the Fano factors as a function of transmission for three values of k, both for cw-light (solid curves) and for pulsed light with a sech^2 pulse shape (dashed curves). Since the effect of all the intensities from zero to the peak intensity has to be integrated, the use of pulses has a detrimental effect on the squeezing. The maximum difference between the pulsed and the cw-case is growing

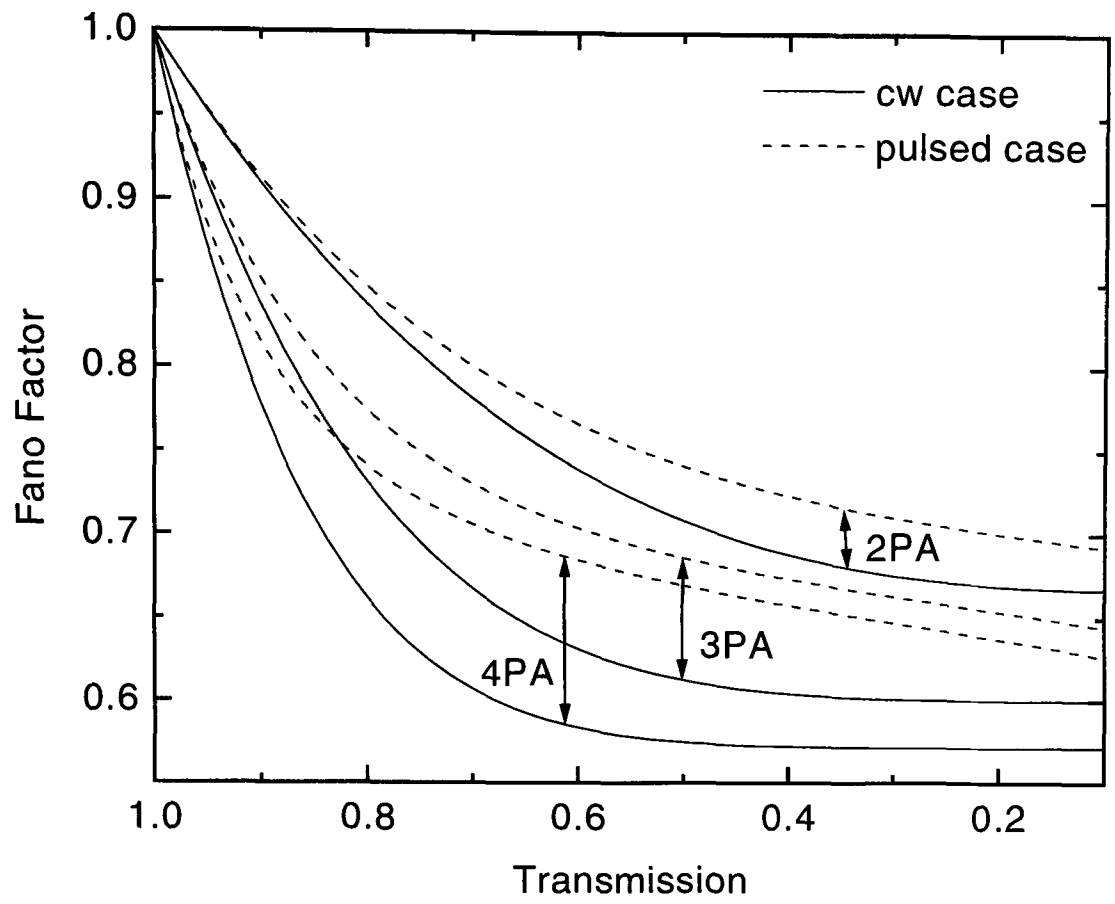

Figure 7.4: Theoretical Fano-factors for squeezing by 2PA, 3PA and 4PA as a function of transmission. The solid lines represent the cw case, the dashed lines represent the sech^2-pulse case. The double arrows indicate the situation where using pulsed light yields the maximum detrimental effect to the squeezing.

with increasing order k of MPA, but also moving towards higher transmission values. For the limiting case of $k \to \infty$, the effect of using pulsed light vanishes as $F_p(T) = F_{cw}(T)$ for any $T < 1$. From a more practical point of view it is worth noting that, in a pulsed regime, there is not much to be gained by going from 3PA to 4PA. However, employing pulse shaping techniques [104] the detrimental effects of using pulses could be reduced and ultimately suppressed for square-shaped pulses.

7.5 MPA-squeezing in organic semiconductor

In order to produce appreciable squeezing in a small sample without using prohibitively high light intensities a very high nonlinear optical susceptibility is required. In this respect organic polymers are important as they are known to possess remarkable nonlinear properties [105]: for example, p-toluene sulphonate polydiacetylene (PTS-PDA) exhibits strong π-electron delocalisation which gives rise to an extremely high nonlinear susceptibility and nonlinear optical absorption [106]. Crucial to the preservation of squeezed states is the exclusion of linear absorption processes, which, because of their purely random nature, drive the photon distribution back towards the initial Poissonian form. We have achieved photon-number squeezing by MPA in a PTS-PDA single crystal by using femtosecond laser pulses at a wavelength of 1.45 μm where the linear optical absorption is negligibly small.

The experimental setup was very similar to that described in § 7.2. The light source was again a shot-noise limited OPO (cf. §§ 4.1.3). After passing through a variable attenuator and polarisation selector, linearly polarised light was focused into the sample to produce peak intensities up to 0.8 GWcm^{-2}. By varying the incident polarisation with respect to the sample, we were able to investigate the nonlinear optical anisotropy of the polymer crystal. The transmitted light was collimated and passed to a balanced detector comprising two identical InGaAs photodiodes (cf. §§ 4.3.2 for the details of the electronics in use). Each photocurrent was amplified, and then the two were either added or subtracted. This detector system allowed us to determine both the actual noise level (corresponding to the sum of photocurrents) and the shot noise level (corresponding to the current difference) by measuring the signal with a radio frequency spectrum analyser. A detection frequency of 25 MHz was selected since this was free of interference from external sources. The quantum efficiency of our detection system was measured to be 74%. This is slightly higher than in the experiments using the AlGaAs waveguide due to

the use of better quality optical components.

PTS-PDA single crystals were produced by K. J. Donovan at the University of London using a well-established growth process [107]. Synthesis of the toluene sulphonate monomer was achieved in two steps, beginning with an oxidative coupling step to synthesise 2.4-hexadiyne-1.6-diol, followed by tosylation of the diol to 2.4-hexadiyne-1.6-ditosyl. Monomer crystals were then grown by temperature-controlled evaporation from acetone, under conditions which prevent both thermal and UV polymerisation. High quality cleaved monomer crystals were then thermally polymerised in vacuum at 60–70°C. The resultant polymer crystals have flat mirror-like (100) facets which contain the chain direction. The thickness of the sample used in our experiments was 400 μm. For more details on the sample, in particular the chemical structure of PTS-PDA, see Appendix A.2.

The linear absorption spectrum of PTS-PDA shows a strong excitonic feature at

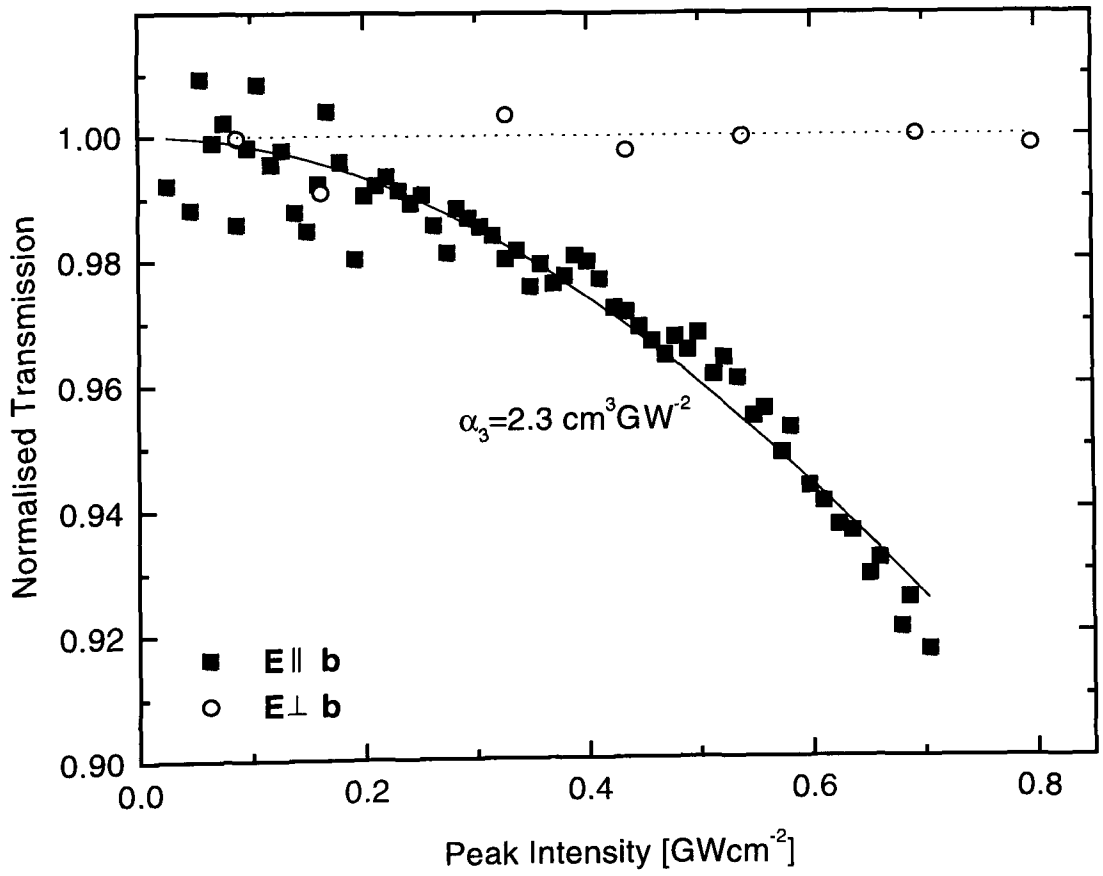

Figure 7.5: Normalised nonlinear transmission of PTS-PDA at 1.45μm showing strong anisotropy with respect to the chain direction. The solid curve gives the theoretical result for 3PA.

620 nm (2.0 eV), with vibronic sidebands extending to higher energy. The absorption is highly anisotropic, with allowed transitions occurring for polarisation parallel to the chain direction **b**. The onset of optical transitions to the electron-hole continuum is estimated to occur at 515 nm ($\sim$ 2.4 eV) [108]. Two-photon and three-photon absorption transitions were identified recently by Lawrence et al., especially in the energy range near 2.7 eV [106]. The nonlinear transmission measured at 1.45 μm (0.87 eV) is shown in Fig. 7.5. As in the case of linear absorption the nonlinear absorption is highly anisotropic (cf. [109]). For light polarised orthogonally to **b** no nonlinear loss is seen, whereas for light polarised in parallel we see significant nonlinear loss. Furthermore, in the parallel case the data agree accurately with the theoretical prediction for 3PA with a coefficient $\alpha_3 = 2.3\ \mathrm{cm^3GW^{-2}}$. At the very highest intensities the transmission appears to drop below the level predicted for 3PA, and may indicate that four-photon absorption is occurring [110].

In Fig. 7.6 we demonstrate the existence of a large squeezing effect, and also, through the polarisation anisotropy, link the effect directly to the nonlinear susceptibility. The inset displays the actual and shot noise levels as measured by the sum and difference photocurrents respectively for an incident peak intensity of 0.54 $\mathrm{GWcm^{-2}}$, showing that the transmitted light is squeezed 11% below the shot noise. The data show that squeezing occurs with the incident polarisation parallel to **b**, but that it is negligibly small when the polarisation is orthogonal to **b**. While the squeezing observed is smaller than that obtained in optical fibres (41% [35] or 52% [36]) its magnitude is quite remarkable for such a small interaction length. In order to compare our result with previous measurements we use a figure of merit ξ which includes the interaction length L : $\xi = \frac{1-F}{L}$. For the present case we obtain $\xi_{\mathrm{PDA}} = 2.7\ \mathrm{cm^{-1}}$, whereas for soliton squeezing in silica optical fibre the figure of merit is $\xi_{\mathrm{fibre}} \approx 5 \times 10^{-4}\ \mathrm{cm^{-1}}$ [35, 36]. Photon number squeezing in AlGaAs semiconductor waveguides is found to have $\xi_{\mathrm{AlGaAs}} = 0.6\ \mathrm{cm^{-1}}$ [12], and in $LiNbO_3$ waveguides $\xi_{\mathrm{LiNbO_3}} = 0.07\ \mathrm{cm^{-1}}$ [111].

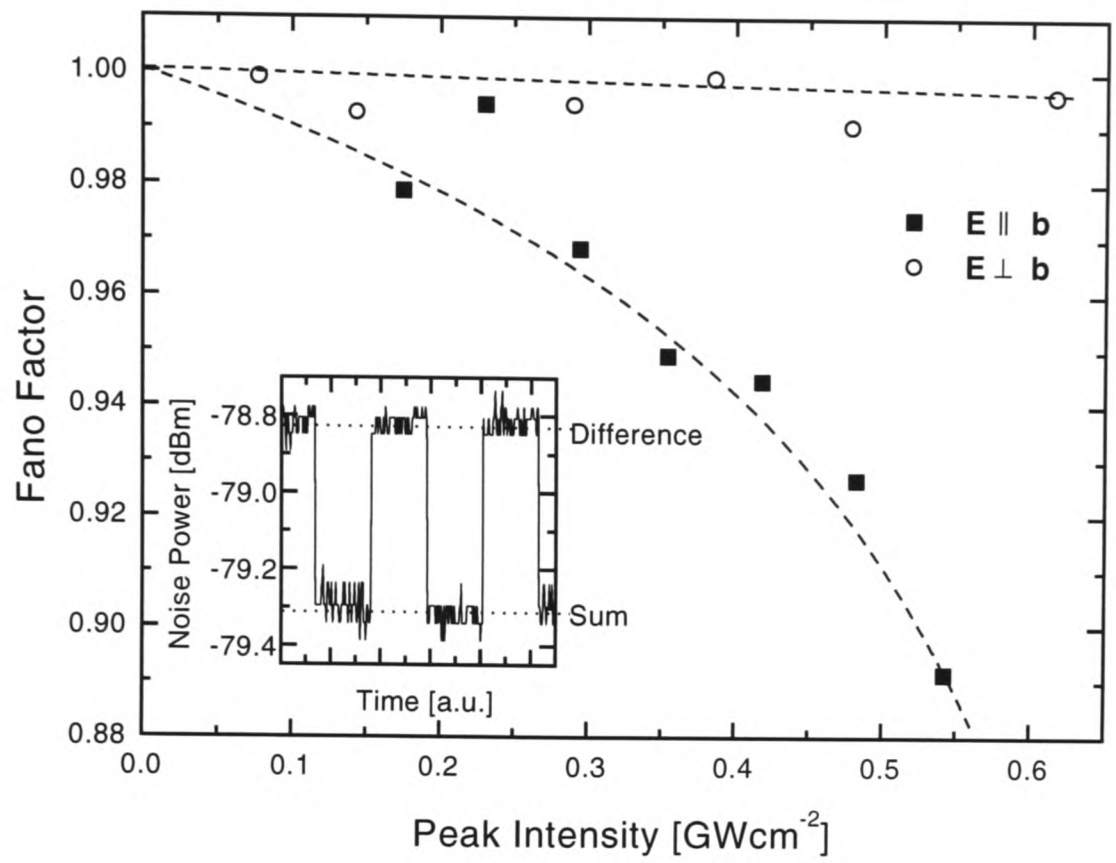

Figure 7.6: Measured Fano factors as a function of intensity for light polarised parallel to and perpendicular to the polymer chains. The dashed lines are guides to the eye. The inset shows the sum and difference photocurrents, which yield the actual noise and shot noise levels respectively, when the intensity is 0.54 GWcm^{-2}.

The measured Fano factors are plotted in Fig. 7.7 as a function of transmission, and compared with predictions of the model for pulsed light described in § 7.4 for two-, three- and four-photon absorption, scaled by the measured detection efficiency of 0.74. The data are seen to fit closely to the predicted three-photon behaviour, except possibly for the lowest transmission (i.e. highest intensity) where the data are closer to the four-photon prediction, which is consistent with the nonlinear transmission data presented in Fig. 7.5.

Organic polymers are now important materials for photonic device applications, including light emitters [112, 113] and optical switches [114], and they can be fabricated into a wide range of architectures [115] for use in the wavelength range of interest for optical communications [116]. The results presented here suggest potentially important

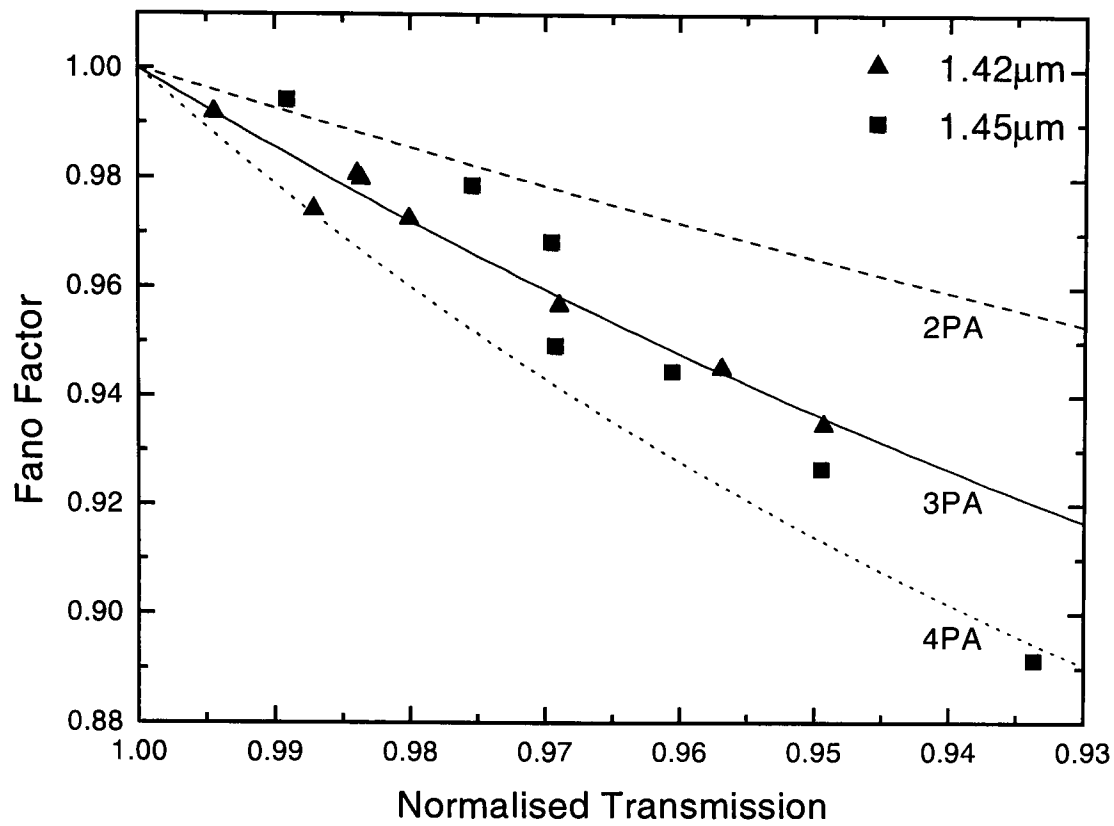

Figure 7.7: The experimentally determined dependence of squeezing on transmission. The theoretical results for two-, three- and four-photon absorption (2PA, 3PA and 4PA respectively) are also shown for comparison. Agreement between experiment and the 3PA prediction is excellent.

new applications in quantum photonics: calculations show that squeezing by 3PA can approach the theoretical limit of 40% with PTS-PDA incorporated in an optical waveguide structure [117].

7.6 Conclusions and outlook

- We have observed for the first time photon-number squeezing by multi-photon absorption (MPA), confirming long-standing theoretical predictions.

- We were using ultrashort pulses in a single pass through an AlGaAs waveguide at photon energies near half the bandgap energy. By tuning the pump light from one side of the halfgap to the other we were able to select between two- and three-photon

absorption. Squeezing by these two processes could be clearly distinguished.

- The theoretical background is reviewed and the effect of using pulsed light in MPA-squeezing is discussed.

- This is the first technique that has been experimentally demonstrated to allow generation of bright squeezed ultrashort pulses in semiconductors.

- We also demonstrate MPA-squeezing in organic semiconductors (namely PTS-PDA). This constitutes the first observation of squeezed light in any organic material, and at the same time shows the general applicability of MPA-squeezing.

The MPA-technique opens up a wide variety of possibilities in the generation of bright squeezed light. MPA is an incoherent mechanism, hence no phase-matching is required. Furthermore it is a broadband effect and suitable squeezing materials could hence be found for any optical wavelength, possibly even beyond. These two factors make MPA-squeezing an extremely versatile technique.

The use of bulk semiconductors required relatively high intensities in the experiments presented in this chapter. These intensity requirements were already significantly reduced when organic polymers were used, even in the non-resonant regime. Using MPA-resonances, the intensity could be reduced further still. Namely, MPA-interaction could be enhanced by employing excitonic features in low-dimensional structures. Likewise the interaction length could be increased by using cavities.

Chapter 8

Photon-number squeezing in light emitting diodes

Contents

8.1 Introduction 103

8.2 Experimental setup 104

8.3 Results 106

8.4 Conclusions and outlook 110

8.1 Introduction

The use of high-efficiency semiconductor light emitters for the generation of photon-number squeezed light directly at source has a number of attractive features. Other than in nonlinear optical methods where costly state-of-the-art lasers and often complex experimental setups are required, this direct conversion method is very simple and inexpensive to implement. Again in contrast with nonlinear optical methods, it allows the generation of strongly squeezed light a very low light intensities where the effect of quantum noise becomes most apparent. In addition, a number of interesting devices based on this method have been demonstrated, such as noiseless taps, amplifiers and optical beam splitters [118, 6]. These devices rely on strongly squeezed light to be effective.

The technique is based on the direct conversion of sub-Poissonian electrical current statistics into sub-Poissonian photon statistics by means of a solid state emitter. When the device is driven through a series resistor R_S, the fluctuations in the stream of interacting electrons are given by the Johnson thermal noise $(\Delta I_{dr})^2 = 4k_BTB/R_S$, where B is the bandwidth of the measurement. Comparing this to a shot noise limited electrical current with $(\Delta I_{sn})^2 = 2e\langle I\rangle B$, the condition for sub-Poissonian electrical current is that the voltage drop in the series resistor ($\langle I\rangle R_S$) should be greater than $2k_BT/e \approx 50$ mV. Hence, by simply combining a constant-voltage source with a sufficiently high series resistance R_S one can easily produce low-noise electrical current which is typically about 20 dB below the shot noise level. The fact that the thermal noise in an electrical circuit can be significantly lower than the shot noise level, is a direct consequence of Coulomb effects experienced by the electrons as the Coulomb repulsion between the electrons favours antibunching. The noise reduction is usually expressed by the Fano-factor F, which is the ratio of the current fluctuations to the shot noise level $F = (\Delta I)^2/(\Delta I_{sn})^2$. Hence a Fano-factor of $F = 1$ denotes Poissonian current and $F < 1$ stands for sub-Poissonian current.

The transfer of electron statistics to photon statistics is limited primarily by the quantum efficiency of the light emitter and is restricted to frequencies below the reciprocal of the average time required for an electron to generate a photon. For the Fano-factor F_{ph} of a *photo*current generated by photon-number squeezed light the following equation can be derived [40]:

$$F_{ph} = \eta F_{dr} + (1 - \eta). \tag{8.1}$$

Here η denotes the overall current-to-current efficiency considering both light emitter and photodetector efficiencies, and F_{dr} is the Fano-factor of the driving current. The first term on the right hand side of (8.1) represents the transfer of noise from the electrical driving current to the photon statistics while the second term stands for the random detection noise due to inefficient photon generation and detection. A Poissonian electrical driving current with $F_{dr} = 1$ therefore leads to a Poissonian photocurrent with $F_{ph} = 1$. In the limit of negligible noise in the driving current, F_{dr} approaches 0 and (8.1) becomes

$$F_{ph} = 1 - \eta. \tag{8.2}$$

High quantum efficiency light emitters hence provide a straightforward method of generating photon-number squeezed light with Fano-factors substantially below unity.

In this chapter we report photon-number squeezing using commercially available infrared light-emitting diodes. The experimental setup is described in § 8.2. We discuss the results on photon-number squeezing as well as correlation effects in series-connected emitters in § 8.3 and conclude in § 8.4.

The work presented in this chapter has been published in ref. [7].

8.2 Experimental setup

The circuit layout for the squeezing measurements is shown in Fig. 8.1. We tested several infrared AlGaAs light-emitting diodes (LEDs), among which the best results were ob-

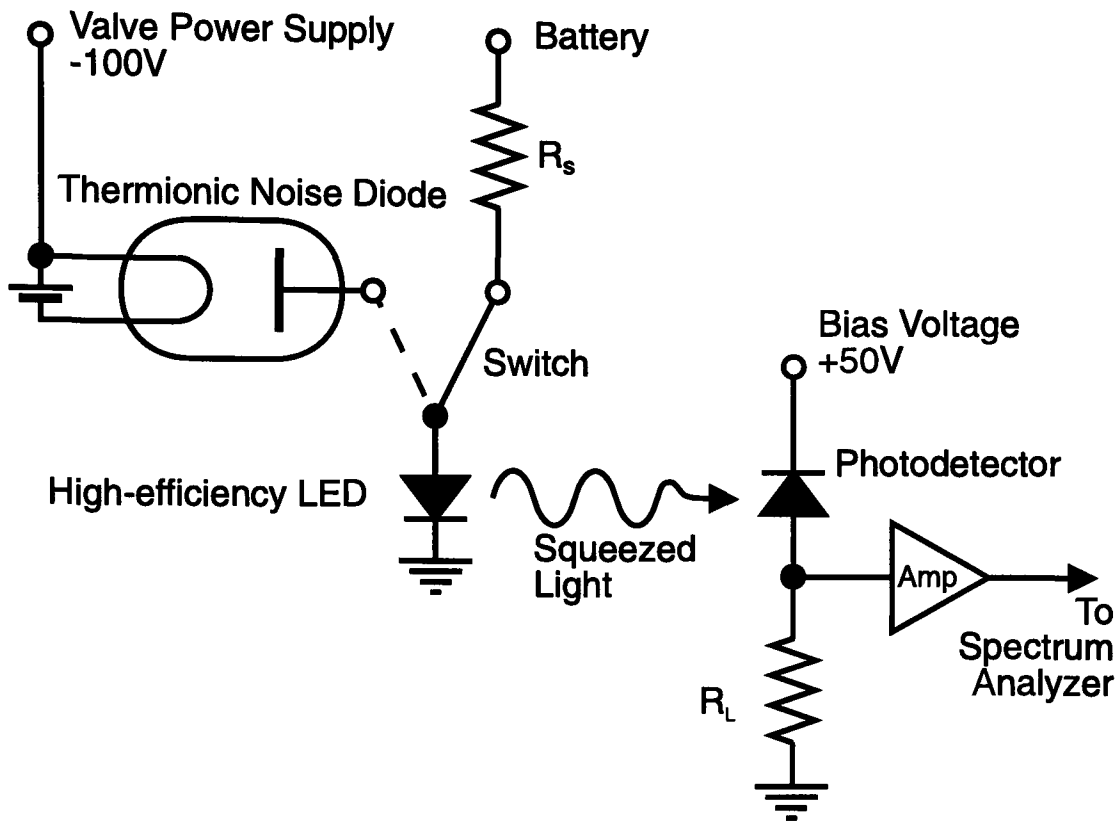

Figure 8.1: Experimental setup: By switching from the high-impedance constant-current source (right) to the thermionic valve (left), the arrangement could be operated in sub-Poissonian or Poissonian mode. The series resistance R_S was typically 500 Ω, the load resistance R_L was 1 kΩ.

tained for the Hewlett Packard HSDL 4220 LED. This is a Transparent Substrate Double Heterojunction diode, which operates at a wavelength of 875 nm at room temperature. The LEDs could be driven either by a high-impedance constant-current source or by a calibrated shot noise source. The constant-current source consisted of a 12-V-battery combined with an appropriate series resistance R_S, while the shot noise level could be verified by switching to a thermionic noise diode (CV172). The emission of electrons from the valve's filament is Poissonian, but space charge effects may result in sub-Poissonian electron arrival statistics at the anode [119]. This was overcome by applying a sufficiently high electron acceleration voltage of at least 100 V in order to operate the thermionic noise diode in the saturated anode-current regime. Measurements of the power fluctuations in the driving current showed a linear dependence on the mean value of the driving

current and thus confirmed the suitability of the thermionic noise diode as a Poissonian current source. The mean current in the driving circuit was determined by measuring the voltage drop across a 100-Ω-high-precision resistor.

The light was captured by a close-coupled *Si-pin*-diode (Hamamatsu S3994) of large area (100 mm^2) and high quantum efficiency (> 0.9), which was held at a reverse bias voltage of up to 50 V. A characterisation of this photodiode can be found in ref. [120]. The AC-noise current was then decoupled by a 0.022 μF-capacitor, followed by a commercial low-noise amplifier. The current fluctuations were finally detected by a swept-frequency spectrum analyser. The two driving currents had to be adjusted to deliver the same mean value of photocurrent before comparing the corresponding noise spectra. The entire experimental setup was shielded in order to avoid rf-pickup in the circuits.

To determine the photocurrent correlations, the light of up to three LEDs in series was coupled into one S3994-photodetector.

8.3 Results

8.3.1 Photon-number squeezing in single LED

A typical noise spectrum for the HSDL 4220 LED is shown in Fig. 8.2. The LED was operated at room temperature with $\langle I_{dr} \rangle = 18.9$ mA, $\langle I_{ph} \rangle = 4.7$ mA and a total current-to-current efficiency $\eta = 25\%$, resulting in a noise reduction below the shot noise of 1.1 dB (22%) at low frequencies, which is in good agreement with the theoretically predicted squeezing value of 1.2 dB (24%) derived from (8.2). Similar measurement carried out at 77 K in a liquid nitrogen cryostat with $\langle I_{dr} \rangle = 22.8$ mA, $\langle I_{ph} \rangle = 9.1$ mA and $\eta = 40\%$ led to an observed squeezing of 2.0 dB (37%), which again is quite close to the theoretical value of 2.25 dB (40%). The small difference between these values might be due to neglecting the effect of differential quantum efficiency [121]. At higher

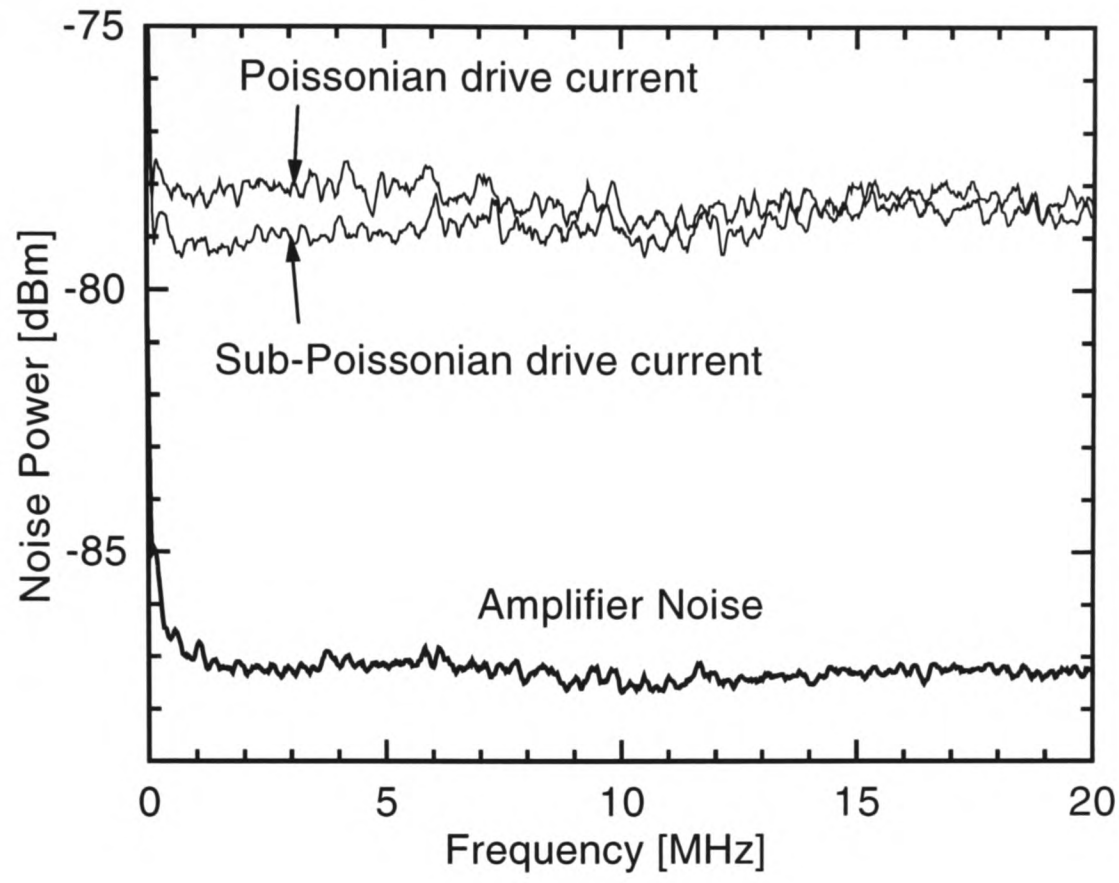

Figure 8.2: Typical noise spectrum of the HP HSDL 4220 LED at room temperature. The curves represent the average of 64 measurements. The spectrum analyser resolution bandwidth was 30 kHz.

frequencies the noise reduction decreases, resulting in a squeezing bandwidth of 8 MHz. This is a considerable improvement over the squeezing bandwidth of about 500 kHz of the Hamamatsu L2656 LED, a device frequently used in recent work on photon-number squeezing (e.g. ref. [5]).

8.3.2 Correlation effects in multiple LEDs in series

The measurements were repeated with LEDs connected in series to investigate correlation effects. According to ref. [5], the normalised correlation coefficient C between the intensity noise of two LEDs in series is equal to

$$C = \frac{\eta F_{dr}}{\eta F_{dr} + (1 - \eta)}. \tag{8.3}$$

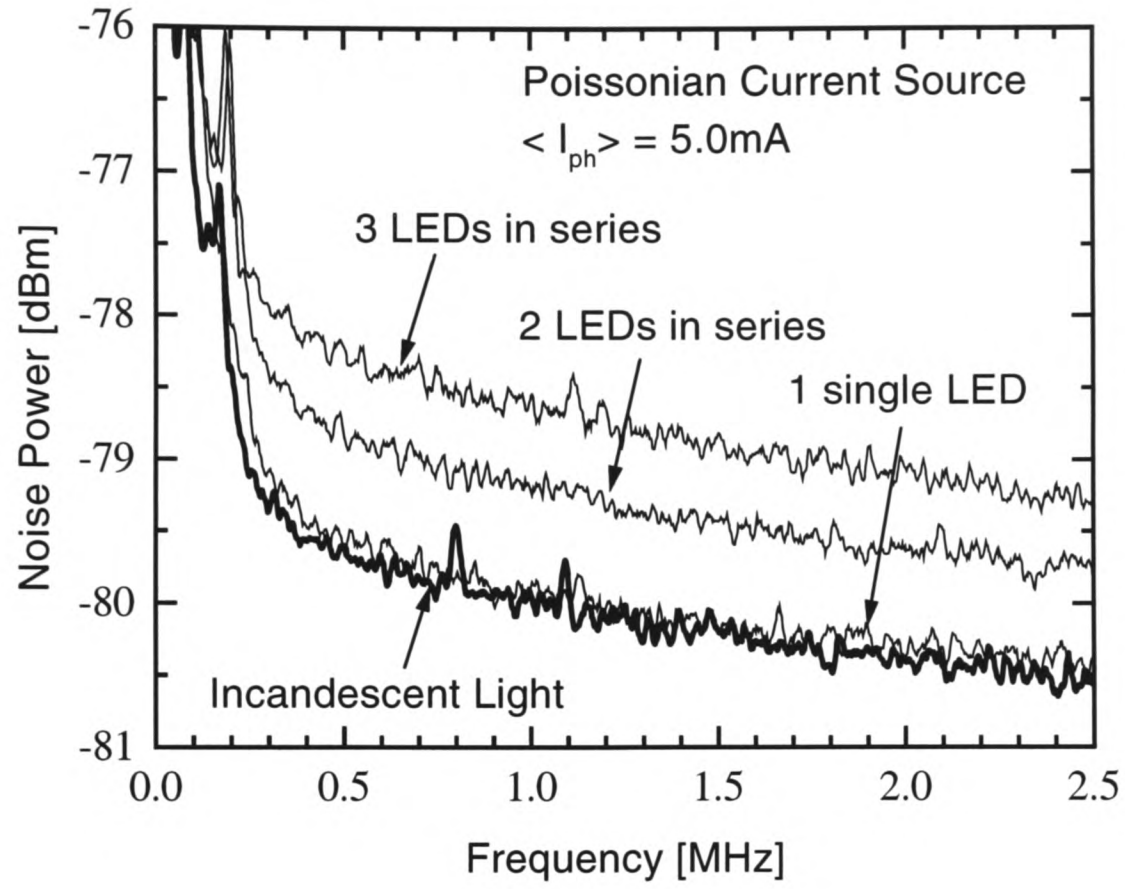

Figure 8.3: Noise spectrum of one single LED compared to two and three LEDs in series. The thicker line represents the noise spectrum of a white tungsten bulb as a shot noise reference. In this case the Poissonian driving current was applied. The mean value of the total photocurrent was 5.0 mA in all cases. The curves represent the average of 64 measurements. The spectrum analyser resolution bandwidth was 30 kHz.

This implies that in the case of applying a Poissonian driving current ($F_{dr} = 1$), the correlation C is equal to the efficiency η, whereas it is approximately zero when operating the diode with the high-impedance constant-current source ($F_{dr} \approx 0$).

Up to three LEDs were connected in series, coupling into the same large-area photodetector to investigate noise correlations between the LEDs. In Figs. 8.3 and 8.4 the noise spectra of one single diode and of two and three LEDs in series are shown. As shot noise reference the noise spectrum of an incandescent tungsten bulb was taken, represented by the thicker line. By choosing an appropriate series resistance R_S, the driving current was adjusted in such a way that the *total* photocurrent was the same in all cases.

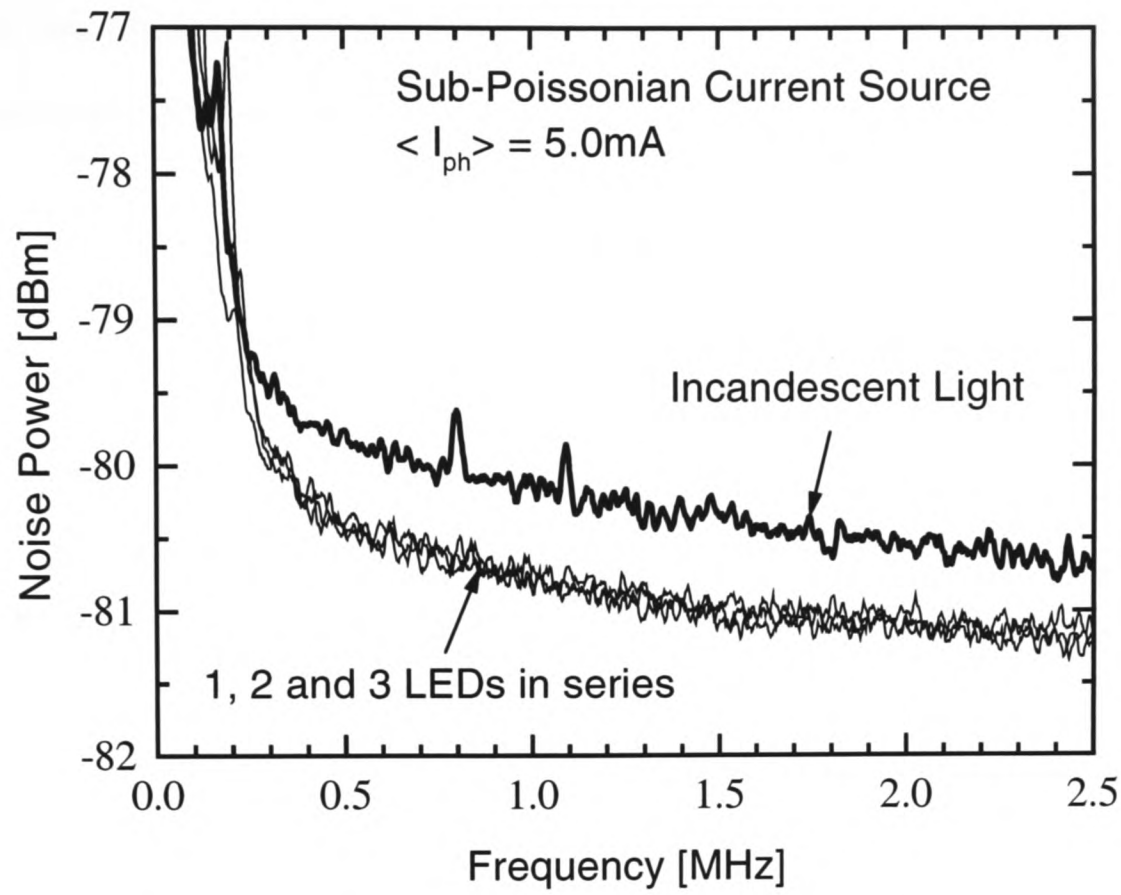

Figure 8.4: Corresponding noise spectrum when running the LEDs from the sub-Poissonian current source. The fact that the three curves coincide indicates that the photocurrent correlation is zero. Other conditions as in Fig. 8.3.

In the case of operating the LEDs with the Poissonian current source (Fig. 8.3), the spectra of one single LED and of two and three diodes in series differ by an equal value of about 0.7 dB, which is due to a non-zero normalised correlation coefficient $C \approx \eta \approx 0.25$, according to (8.3). As expected, the noise spectrum of one single light-emitting diode matches that of the tungsten bulb (This confirms that the electrical current through the thermionic noise diode is shot noise limited.). For more than one LED in series, the correlations cause the total photocurrent to be super-Poissonian. Identical measurements at 77 K show a corresponding correlation coefficient of $C \approx 0.40$, reflecting the higher quantum efficiency of the LEDs at low temperature.

When applying the high-impedance constant-current source, however, the corresponding noise spectra coincide, all lying equally below the shot noise level (Fig. 8.4). This

indicates that the photocurrent correlation coefficient is zero, in agreement with (8.3).

For N identical LEDs of efficiency η in series, the following formula can be derived readily:

$$(\Delta I_{ph})^2 = (1-\eta)2e\langle I_{dr}\rangle B(1+\underbrace{(N-1)C}_{\text{additional noise due to correlation}}). \tag{8.4}$$

In the case of operating the LEDs with the high-impedance constant-current source (sub-Poissonian mode), $F_{dr} \approx 0 \Rightarrow C \approx 0$, so that

$$(\Delta I_{ph})^2 = (1-\eta)2e\langle I_{dr}\rangle B, \tag{8.5}$$

which is identical to the photocurrent fluctuations of a single device. When running the LEDs from the Poissonian current source, $F = 1 \Rightarrow C = \eta$ and (8.4) becomes

$$(\Delta I_{ph})^2 = 2e\langle I_{dr}\rangle B(1+(N-1)\eta). \tag{8.6}$$

On a logarithmic scale this results in a difference d in noise power in dB when switching between the two different current sources:

$$d = 10\log\left(1+\frac{N\eta}{1-\eta}\right) \quad [\text{dB}]. \tag{8.7}$$

For $N = 1$ this formula reduces to (8.2). Measured and theoretical values showed very good agreement for $N = 2$. For $N = 3$ the experimental value was usually about 0.2–0.3 dB smaller than the theoretical value. It has to be taken into account, however, that the coupling efficiency per single device decreases when trying to collect the light from three LEDs with one single photodetector.

8.4 Conclusions and outlook

- We investigated the photon-number squeezing properties of a new type of low-cost commercially available, high-efficiency double heterojunction AlGaAs infrared

LEDs. Using these devices, squeezed light can be generated very easily and at low intensity levels, where the quantum noise is most apparent.

- The overall current-to-current efficiency of 25% at room temperature and 40% at 77 K led to an observed photon-number squeezing below the SQL of 1.1 dB and 2.0 dB, respectively which is amongst the highest measured in LEDs to date.

- In addition, measurements of several light-emitting diodes in series revealed effects that are explained by a strong photocurrent correlation. A normalised correlation coefficient of about 0.25 at room temperature and 0.40 at 77 K was observed.

The devices used in the present study showed perfect "textbook"-behaviour, and provided an ideal system to investigate correlation effects. In the future it is planned to study more complex structures, e.g. high-efficiency microcavity LEDs and organic LEDs. Furthermore it would be interesting to investigate similar effects in novel laser structures, such as quantum wire and quantum dot lasers. On the one hand, this could lead to higher squeezing. On the other hand, squeezing measurements could contribute — e.g. through the understanding gained with the correlation experiments on simpler devices discussed here — to the characterisation of such devices and could provide more insight into the underlying processes.

Appendix A

Sample descriptions

This appendix contains descriptions of the waveguide sample used in Chapter 7 and § 6.4, as well as of the PTS-PDA sample used in Chapter 7.

A.1 AlGaAs-waveguide

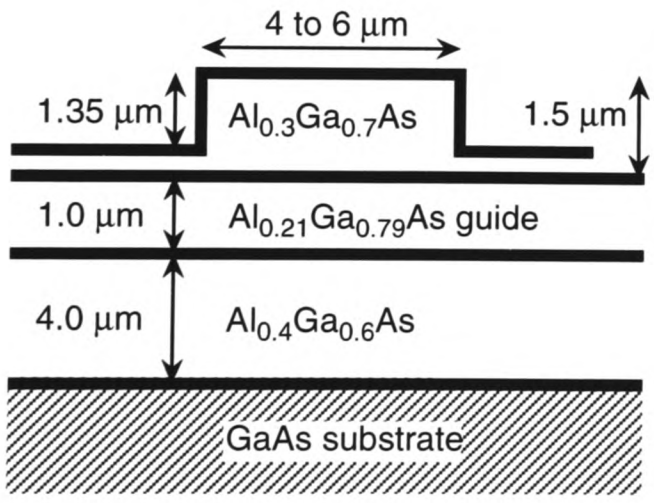

Figure A.1: Schematic diagram of cross-section of the AlGaAs-waveguide structure.

The AlGaAs waveguide sample was grown by Molecular Beam Epitaxy at the University of Glasgow. Fig. A.1 shows a schematic of the sample. It consists of a 1 μm thick, high-index waveguiding layer, composed of $Al_{0.21}Ga_{0.79}As$ and grown on a 4 μm thick $Al_{0.4}Ga_{0.6}As$ cladding layer, which itself is grown on a [001]-oriented GaAs substrate. A 1.5 μm thick and 4–6 μm wide $Al_{0.3}Ga_{0.7}As$ rib etched on top provides the lateral

confinement. This results in a calculated active area of about 6 μm^2 [97].

The sample was 2 mm long and both faces were anti-reflection coated. Linear losses were estimated to be 0.16 cm^{-1} or 0.7 dB/cm ($\pm$0.5 dB/cm). For a more detailed description of a similar waveguide, see [97].

A.2 PTS-PDA sample

The chemical structure of *p*-toluene sulphonate polydiacetylene (PTS-PDA) is shown in Fig. A.2 [109]. The upper part of the Figure shows a diacetylene unit which is repeated n times to form a polymer chain. It has got organic side groups R_1 and R_2 which, in the case of PTS-PDA, are both PTS-groups as depicted in the lower part of the Figure.

Our sample was a 400 μm thick PTS-PDA single crystal produced by K. J. Donovan at the University of London using a well-established growth process [107]. Synthesis of the toluene sulphonate monomer was achieved in two steps, beginning with an oxidative coupling step to synthesise 2.4-hexadiyne-1.6-diol, followed by tosylation of the diol to 2.4-hexadiyne-1.6-ditosyl. The resultant monomer was purified by successive re-

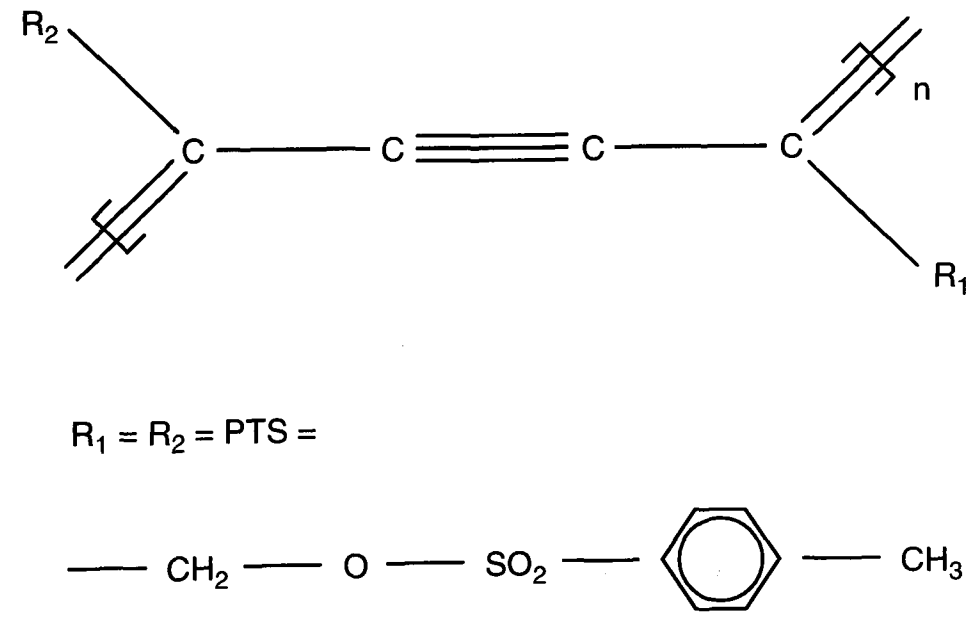

Figure A.2: Structural formula of PDA and the organic side groups (R_1, R_2) of the symmetrically substituted PTS.

crystallisations from acetone. Purity was also checked by NMR and FTIR spectroscopy. Monomer crystals were then grown by temperature-controlled evaporation from acetone, under conditions which prevent both thermal and UV polymerisation. High quality cleaved monomer crystals were then thermally polymerised in vacuum at 60–70°C. The resultant polymer crystals have flat mirror-like (100) facets which contain the chain direction.

Bibliography

[1] R. E. Slusher, L. W. Hollberg, B. Yurke, J. C. Mertz, and J. F. Valley. Observation of squeezed states generated by 4-wave mixing in an optical cavity. Phys. Rev. Lett. **55**, 2409 (1985).

[2] M. C. Teich and B. E. A. Saleh. Observation of sub-Poisson Franck-Hertz light at 253.5 nm. J. Opt. Soc. Am. B **2**, 275 (1985).

[3] S. Machida, Y. Yamamoto, and Y. Itaya. Observation of amplitude squeezing in a constant-current driven semiconductor laser. Phys. Rev. Lett. **58**, 1000 (1987).

[4] P. R. Tapster, J. G. Rarity, and J. S. Satchell. Generation of sub-Poissonian light by high-efficiency light-emitting diodes. Europhys. Lett. **4**, 293 (1987).

[5] E. Goobar, A. Karlsson, G. Björk, and P.-J. Rigole. Quantum correlated light beams and sub-Poissonian electrical partition noise in parallel and series coupled semiconductor light emitters. Phys. Rev. Lett. **70**, 437 (1993).

[6] J.-F. Roch, J.-P. Poizat, and P. Grangier. Sub-shot-noise manipulation of light using semiconductor emitters and recievers. Phys. Rev. Lett. **71**, 2006 (1993).

[7] F. Wölfl, G.-M. Schucan, A. M. Fox, and J. F. Ryan. Improved photon-number squeezing in light-emitting diodes. J. Mod. Opt. **45**, 1147 (1998).

[8] A. M. Fox, J. J. Baumberg, M. Dabbicco, B. Huttner, and J. F. Ryan. Squeezed light generation in semiconductors. Phys. Rev. Lett. **74**, 1728 (1995).

[9] A. M. Fox, M. Dabbicco, G. von Plessen, and J. F. Ryan. Quadrature squeezed light generation by cross-phase modulation in semiconductors. Opt. Lett. **20**, 2523 (1995).

[10] G.-M. Schucan, A. M. Fox, and J. F. Ryan. Femtosecond quadrature squeezed light generation in CdSe at 1.55 μm. Opt. Lett. **23**, 712 (1998).

[11] G.-M. Schucan, R. G. Ispasoiu, A. M. Fox, and J. F. Ryan. Ultrafast two-photon nonlinearities in CdSe near 1.5 μm studied by interferometric autocorrelation. IEEE J. Quantum Electron. **34**, 1374 (1998).

[12] G.-M. Schucan, M. B. Ward, K. Turner, T. Goodson III, A. M. Fox, J. F. Ryan, J. S. Aitchison, and C. N. Ironside. Bright squeezed light generation by multi-photon absorption. Submitted to Phys. Rev. Lett. (1998).

[13] T. Goodson III, M. B. Ward, K. Turner, G.-M. Schucan, K. J. Donovan, A. M. Fox, and J. F. Ryan. Generation of bright squeezed light in organic polymers. Submitted to Science (1998).

[14] N. Tornau and A. Bach. Quantum statistics of two-photon absorption. Opt. Comm. **11**, 46 (1974).

[15] K. J. McNeil and D. F. Walls. A master equation approach to nonlinear optics. J. Phys. A **7**, 617 (1974).

[16] L. Davidovich. Sub-poissonian processes in quantum optics. Rev. Mod. Phys. **68**, 127 (1996).

[17] H.-A. Bachor. A guide to experiments in quantum optics. WILEY-VCH, Weinheim, 1998.

[18] L. I. Schiff. Quantum mechanics. McGraw-Hill, New York, 3rd edition, 1968.

[19] R. J. Glauber. Coherent and incoherent states of the radiation field. Phys. Rev. **131**, 2766 (1963).

[20] C. M. Caves. Quantum-mechanical noise in an interferometer. Phys. Rev. D **23**, 1693 (1981).

[21] P. A. M. Dirac. The quantum theory of emission and absorption of radiation. Prog. Roy. Soc. A **114**, 243 (1927).

[22] L. Susskind and J. Glogower. Quantum mechanical phase and time operator. Physics **1**, 49 (1964).

[23] D. T. Pegg and S. M. Barnett. Unitary phase operator in quantum mechanics. Europhys. Lett. **6**, 483 (1988).

[24] D. T. Pegg and S. M. Barnett. Phase properties of the quantized single-mode electromagnetic field. Phys. Rev. A **39**, 1665 (1989).

[25] S. M. Barnett and D. T. Pegg. On the hermitian optical-phase operator. J. Mod. Opt. **36**, 7 (1989).

[26] G. Leuchs. Squeezing the quantum fluctuations of light. Contemp. Phys. **29**, 299 (1988).

[27] H. P. Yuen. Generalized coherent states and the statistics of two-photon lasers. Phys. Lett. **51A**, 1 (1975).

[28] H. P. Yuen. Two-photon coherent states of the radiation field. Phys. Rev. A **13**, 2226 (1976).

[29] L.-A. Wu, H. J. Kimble, J. L. Hall, and H. Wu. Generation of squeezed states by parametric down conversion. Phys. Rev. Lett. **57**, 2520 (1986).

[30] E. S. Polzik, J. Carri, and H. J. Kimble. Atomic spectroscopy with squeezed light for sensitivity beyond the vacuum-state limit. Appl. Phys. B **55**, 279 (1992).

[31] R. Short and L. Mandel. Observation of sub-Poissonian photon statistics. Phys. Rev. Lett. **51**, 384 (1983).

[32] S. F. Pereira, M. Xiao, H. J. Kimble, and J. L. Hall. Generation of squeezed light by intercavity frequency doubling. Phys. Rev. A **38**, 4931 (1988).

[33] A. Sizmann, R. J. Horowicz, E. Wagner, and G. Leuchs. Observation of amplitude squeezing of the up-converted mode in second harmonic generation. Opt. Comm. **80**, 138 (1990).

[34] R. D. Li, S. K. Choi, C. Kim, and P. Kumar. Generation of sub-Poissonian pulses of light. Phys. Rev. A **51**, R3429 (1995).

[35] S. R. Friberg, S. Machida, M. J. Werner, A. Levanon, and T. Mukai. Observation of optical soliton photon-number squeezing. Phys. Rev. Lett. **77**, 3775 (1996).

[36] S. Spälter, M. Burk, U. Strössner, M. Böhm, A. Sizmann, and G. Leuchs. Photon number squeezing of spectrally filtered sub-picosecond optical solitons. Europhys. Lett. **38**, 335 (1997).

[37] Y. Yamamoto, S. Machida, and O. Nilsson. Amplitude squeezing in a pump-noise-suppressed laser oscillator. Phys. Rev. A **34**, 4025 (1986).

[38] Y. Yamamoto and S. Machida. High-impedance suppression of pump fluctuation and amplitude squeezing in semiconductor lasers. Phys. Rev. A **35**, 5114 (1987).

[39] W. H. Richardson, S. Machida, and Y. Yamamoto. Squeezed photon-number noise and sub-Poissonian electrical partition noise in a semiconductor laser. Phys. Rev. Lett. **66**, 2867 (1991).

[40] H.-A. Bachor, P. Rottengatter, and C. M. Savage. Correlation effects in light sources with high quantum efficiency. Appl. Phys. B **55**, 258 (1992).

[41] P. J. Edwards and G. H. Pollard. Quantum noise-correlated operation of electrically coupled semiconductor light emitters. Phys. Rev. Lett. **69**, 1757 (1992).

[42] T. Hirano and T. Kuga. Generation of weak sub-Poissonian light by a high-efficiency light-emitting diode. IEEE J. Quantum Electron. **31**, 2236 (1995).

[43] J. P. Poizat and P. Grangier. Experimental realization of a quantum optical tap. Phys. Rev. Lett. **70**, 271 (1993).

[44] G. Shinozaki, J. Abe, T. Hirano, T. Kuga, and M. Yamanishi. 3 dB wideband squeezing in photon number fluctuations from a light emitting diode. Jpn. J. Appl. Phys. **36, Part 1**, 6350 (1997).

[45] Y. R. Shen. The principles of nonlinear optics. John Wiley & Sons, New York, 1984.

[46] P. N. Butcher and D. Cotter. The elements of nonlinear optics, vol. 9 of *Cambdridge Studies in Modern Optics*. Cambridge University Press, Cambridge, 1990.

[47] D. S. Chemla and J. Jerphagnon. Nonlinear optical properties. In T. S. Moss, editor, *Handbook of Semiconductors*, vol. 2, pp. 545–598. North-Holland, 1980.

[48] M. Sheik-Bahae, D. G. Hagan, and E. W. Van Stryland. Dispersion and band-gap scaling of the electronic Kerr effect in solids associated with two-photon absorption. Phys. Rev. Lett. **65**, 96 (1990).

[49] M. Sheik-Bahae, D. C. Hutchings, D. G. Hagan, and E. W. Van Stryland. Dispersion of bound electronic nonlinear refraction in solids. IEEE J. Quantum Electron. **27**, 1296 (1991).

[50] C. N. Ironside. Ultra-fast all-optical switching. Contemp. Phys. **34**, 1 (1993).

[51] G. I. Stegeman and W. E. Torruellas. Nonlinear materials for information processing and communications. Phil. Trans. R. Soc. Lond. A **354**, 745 (1996).

[52] R. H. Stolen and C. Lin. Self-phase-modulation in silica optical fibers. Phys. Rev. A **17**, 1448 (1978).

[53] S.-T. Ho, X. Zhang, and M. K. Udo. Single-beam squeezed-state generation in semiconductor waveguides with $\chi^{(3)}$ nonlinearity at below half-band gap. J. Opt. Soc. Am. B **12**, 1537 (1995).

[54] M. D. Levenson, R. M. Shelby, and S. L. Perlmutter. Squeezing of classical noise by non degenerate four wave mixing in an optical fiber. Opt. Lett. **10**, 514 (1985).

[55] E. O. Kane. Band structure of indium antimonide. J. Chem. Phys. Solids **1**, 249 (1957).

[56] E. W. Van Stryland, M. A. Woodall, H. Vanherzeele, and M. J. Soileau. Energy band-gap dependence of two-photon absorption. Opt. Lett. **10**, 490 (1985).

[57] B. S. Wherrett. Scaling rules for multiphoton interband absorption in semiconductors. J. Opt. Soc. Am. B **1**, 67 (1984).

[58] M. D. Dvorak, W. A. Schroeder, D. R. Andersen, A. L. Smirl, and B. S. Wherrett. Measurement of the anisotropy of two-photon absorption coefficients in zincblende semiconductors. IEEE J. Quantum Electron. **30**, 256 (1994).

[59] W. A. Schroeder, D. S. McCallum, D. R. Harken, M. D. Dvorak, D. R. Anderson, and A. L. Smirl. Intrinsic and induced anisotropy of nonlinear absorption and refraction in zinc blende semiconductors. J. Opt. Soc. Am. B **12**, 401 (1995).

[60] D. Hutchings and B. S. Wherrett. Theory of the anisotropy of ultrafast nonlinear refraction in zinc-blende semiconductors. Phys. Rev. B **52**, 8150 (1995).

[61] M. Rosenbluh and R. M. Shelby. Squeezed optical solitons. Phys. Rev. Lett. **66**, 153 (1991).

[62] P. D. Drummond, R. M. Shelby, S. R. Friberg, and Y. Yamamoto. Quantum solitons in optical fibres. Nature **365**, 307 (1993).

[63] N. Bloembergen and Y. R. Shen. Coupling between vibrations and light waves Raman laser media. Phys. Rev. Lett. **12**, 504 (1964).

[64] Y. R. Shen and N. Bloembergen. Theory of stimulated Brillouin and Raman scattering. Phys. Rev. **137**, A1787 (1965).

[65] K. Turner. Hot carrier relaxation in GaAs quantum wells and v-groove quantum wires. D.Phil. thesis, University of Oxford, 1995.

[66] D. C. Edelstein, E. S. Wachman, and C. L. Tang. Broadly tunable high repetition rate femtosecond optical parametric oscillator. Appl. Phys. Lett. **54**, 1728 (1989).

[67] Q. Fu, G. Mak, and H. M. van Driel. High-power, 62-fs infrared optical parametric oscillator synchronously pumped by a 76 MHz Ti-sapphire laser. Opt. Lett. **17**, 1006 (1992).

[68] A. Nebel, C. Fallnich, R. Beigang, and R. Wallenstein. Noncritically phase-matched continuous-wave mode-locked singly resonant optical parametric oscillator synchronously pumped by a Ti-sapphire laser. J. Opt. Soc. Am. B **10**, 2195 (1993).

[69] T. J. Driscoll, G. M. Gale, and F. Hache. Ti sapphire 2nd-harmonic-pumped visible range femtosecond optical parametric oscillator. Opt. Comm. **110**, 638 (1994).

[70] K. L. Sala, G. A. Kenney-Wallace, and G. E. Hall. CW autocorrelation measurements of picosecond laser pulses. IEEE J. Quantum Electron. **QE-16**, 990 (1980).

[71] D. T. Reid, M. Padgett, C. McGowan, W. E. Sleat, and W. Sibbett. Light-emitting diodes as measurement devices for femtosecond laser pulses. Opt. Lett. **22**, 233 (1997).

[72] H. P. Yuen and J. H. Shapiro. Optical communication with two-photon coherent states — part III: Quantum measurements realizable with photoemissive detectors. IEEE Trans. Inf. Theory **IT-26**, 78 (1980).

[73] D. F. Walls and P. Zoller. Reduced quantum fluctuations in resonance fluorescence. Phys. Rev. Lett. **47**, 709 (1981).

[74] H. P. Yuen and V. W. S. Chan. Noise in homodyne and heterodyne detection. Opt. Lett. **8**, 177 (1983).

[75] M. J. Freeman. Amplitude squeezed light generation in semiconductor diode lasers. Ph.D. thesis, University of Michigan, 1994.

[76] S. T. Ho, C. E. Soccolich, M. N. Islam, W. S. Hobson, A. F. Levi, and R. E. Slusher. Large nonlinear phase shifts in low-loss Algaas waveguides near half-gap. Appl. Phys. Lett. **59**, 2558 (1991).

[77] J. S. Aitchison, D. C. Hutchings, J. U. Kang, G. I. Stegeman, and A. Villeneuve. The nonlinear optical properties of AlGaAs at the half band gap. IEEE J. Quantum Electron. **33**, 341 (1997).

[78] O. Madelung, editor. Semiconductors - Basic Data. Springer, Berlin, 2nd edition, 1996.

[79] A. Villeneuve, C. C. Yang, G. I. Stegeman, C.-H. Lin, and H.-H. Lin. Nonlinear refractive-index and two photon-absorption near half the band gap in AlGaAs. Appl. Phys. Lett. **62**, 2465 (1993).

[80] M. Dabbicco, A. M. Fox, G. von Plessen, and J. F. Ryan. Role of $\chi^{(3)}$ anisotropy in the generation of squeezed light in semiconductors. Phys. Rev. B **53**, 4479 (1996).

[81] C. C. Yang, A. Villeneuve, G. I. Stegeman, C.-H. Lin, and H.-H. Lin. Effects of dispersive two-photon transitions on femtosecond pulse propagation in semiconductor waveguides. Appl. Phys. Lett. **63**, 1304 (1996).

[82] I. E. Day, P. A. Snow, R. V. Penty, I. H. White, R. S. Grant, G. T. Kennedy, W. Sibbett, D. A. O. Davies, M. A. Fisher, and M. J. Adams. Bias dependent recovery time of all-optical resonant nonlinearity in an InGaAsP/InGaAsP multiquantum well waveguide. Appl. Phys. Lett. **65**, 2657 (1994).

[83] Y.-H. Kao, M. N. Islam, J. M. Saylor, R. E. Slusher, and W. S. Hobson. Raman effect in AlGaAs waveguides for subpicosecond pulses. J. Appl Phys. **78**, 2198 (1995).

[84] J.-C. M. Diels, J. J. Fontaine, I. C. McMichael, and F. Simoni. Control and measurement of ultrashort pulse shapes (in amplitude and phase) with femtosecond accuracy. Appl. Opt. **24**, 1270 (1985).

[85] O. Madelung, editor. Landolt-Börnstein Numerical Data and Functional Relationships in Science and Technology, New Series, vol. III 17b. Springer-Verlag, Berlin, 1982.

[86] J. A. Bolger, I. Galbraith, A. K. Kar, J. Simpson, S. Y. Wang, K. A. Prior, B. C. Cavenett, and B. S. Wherrett. Band-edge refractive optical nonlinearities in molecular beam-grown ZnSe epilayers. Appl. Phys. Lett. **63**, 709 (1993).

[87] D. H. Auston, S. McAffee, C. V. Shank, E. P. Ippen, and O. Teschke. Picosecond spectroscopy of semiconductors. Solid State Electron. **21**, 147 (1978).

[88] W. Z. Lin, R. W. Schoenlein, J. G. Fujimoto, and E. P. Ippen. Femtosecond absorption saturation studies of hot carriers in GaAs and AlGaAs. IEEE J. Quantum Electron. **24**, 267 (1988).

[89] V. Mizrahi, K. W. DeLong, G. I. Stegeman, M. A. Saifi, and M. J. Andrejco. Two-photon absorption as a limitation for all-optical switching. Opt. Lett. **14**, 1140 (1989).

[90] R. E. Slusher and B. Yurke. Squeezed light for coherent communications. J. of Lightwave Technol. **8**, 466 (1990).

[91] G.-M. Schucan, M. Dabbicco, A. M. Fox, G. von Plessen, and J. F. Ryan. Nonlinear semiconductor waveguides for quantum communication systems. In M. Scheffler and R. Zimmermann, editors, *The Proceedings of the 23rd International Conference on the Physics of Semiconductors*, vol. 4, pp. 3235–3238. World Scientific Press, Singapore, 1996.

[92] C. Kim and P. Kumar. Quadrature-squeezed light detection using a self-generated matched local oscillator. Phys. Rev. Lett. **73**, 1605 (1994).

[93] J. J. Baumberg. Coherent Nonlinear Optical Processes in Semiconductors. D.Phil. thesis, University of Oxford, 1992.

[94] M. E. Anderson, D. F. McAlister, M. G. Raymer, and M. C. Gupta. Pulsed squeezed-light generation in $\chi^{(2)}$ nonlinear waveguides. J. Opt. Soc. Am. B **14**, 3180 (1997).

[95] F. X. Kärtner, D. J. Dougherty, H. A. Haus, and E. P. Ippen. Raman noise and soliton squeezing. J. Opt. Soc. Am. B **11**, 1267 (1994).

[96] J. H. Shapiro and L. Boivin. Raman-noise limit on squeezing in continuous-wave four-wave mixing. Opt. Lett. **20**, 925 (1995).

[97] A. Villeneuve, J. S. Aitchison, B. Vögele, R. Tapella, J. U. Kang, C. Trevino, and G. I. Stegeman. Waveguide design for minimum nonlinear effective area and switching energy in AlGaAs at half the bandgap. Europhys. Lett. **31**, 549 (1995).

[98] J. S. Aitchison. Private communication.

[99] H. Paul, U. Mohr, and W. Brunner. Change of photon statistics due to multi-photon absorption. Opt. Comm. **17**, 145 (1976).

[100] R. Loudon. Squeezing in two-photon absorption. Opt. Comm. **49**, 67 (1984).

[101] Y. R. Shen. Quantum statistics of nonlinear optics. Phys. Rev. **155**, 921 (1967).

[102] E. D. Palik. Gallium arsenide (GaAs). In E. D. Palik, editor, *Handbook of optical constants of solids*, Academic Press Handbook Series, pp. 429–443. Academic Press, Orlando, 1985.

[103] M. S. Zubairy and J. J. Yeh. Photon statistics in multiphoton absorption and emission processes. Phys. Rev. A **21**, 1624 (1980).

[104] M. M. Wefers and K. A. Nelson. Programmable phase and amplitude femtosecond pulse shaping. Opt. Lett. **18**, 2032 (1993).

[105] M. Samoc, A. Samoc, L. D. Ba, Z. N. Bao, and L. P. Yu. Femtosecond z-scan and degenerate four-wave mixing measurements of real and imaginary parts of the third-order nonlinearity of soluble conjugated polymers. J. Opt. Soc. Am. B **15**, 817 (1992).

[106] B. Lawrence, W. E. Torruellas, M. Cha, M. L. Sunheimer, G. I. Stegeman, J. Meth, S. Etemad, and G. Baker. Identification and role of two-photon excited states in a p-conjugated polymer. Phys. Rev. Lett. **73**, 597 (1984).

[107] G. Wegner. Topochemische Reaktionen von Monomeren mit konjugierten Dreifachbindungen. Makromolek. Chem. **175**, 667 (1971).

[108] K. J. Donovan and E. G. Wilson. Photocarrier creation in one dimension. Phil Mag B **44**, 31 (1981).

[109] T. Fehn, T. Vogtmann, J. Hübner, and M. Schwoerer. Anisotropy of the nonlinear optical susceptibility $\chi^{(3)}$ in polydiacetylene single crystals. Appl. Phys. B **59**, 203 (1994).

[110] H. Shim, M. Liu, C. Hwangbo, and G. I. Stegeman. Four-photon absorption in the single-crystal polymer bis(paratoluene) sulfonate. Opt. Lett. **23**, 430 (1998).

[111] D. K. Serkland, P. Kumar, M. A. Arbore, and M. M. Fejer. Amplitude squeezing by means of quasi-phase-matched second-harmonic generation in a lithium niobate waveguide. Opt. Lett. **22**, 1497 (1997).

[112] V. G. Kozlov, V. Balovic, D. G. Burrows, and S. R. Forrest. Laser action in organic semiconductor waveguide and double heterostructure devices. Nature **389**, 362 (1997).

[113] N. Tessler, G. J. Denton, and R. H. Friend. Lasing from conjugated-polymer microcavities. Nature **382**, 695 (1996).

[114] B. Luther-Davies and M. Samoc. Third-order nonlinear optical organic materials for photonic switching. Curr. Opin. Solid State Phys **2**, 213 (1997).

[115] G. T. Boyd. Polymers for non-linear optics. In C. P. Wong, editor, *Polymers for Electronic and Photonic Applications*, pp. 467–505. Academic Boston, Mass., 1993.

[116] S. R. Marder, B. Kippelen, A. K.-Y. Jen, and N. Peyghambarian. Design and synthesis of chromophores and polymers for electro-optic and photorefreactive applications. Nature **388**, 845 (1997).

[117] M. Thakur and D. M. Krol. Demonstration of all-optical phase modulation in polydiacetylene waveguides. Appl. Phys. Lett. **56**, 1213 (1990).

[118] E. Goobar, A. Karlsson, and G. Björk. Experimental realization of a semiconductor photon number amplifier and a quantum optical tap. Phys. Rev. Lett. **71**, 2002 (1993).

[119] L. D. Smullin and H. A. Haus. Noise in Electron Devices, Electronic Apparatus and Appliances Noise. Wiley, 1959.

[120] M. J. Freeman, H. Wang, D. G. Steel, R. Craig, and D. R. Scifres. Wavelength-tunable amplitude-squeezed light from a room-temperature quantum-well laser. Opt. Lett. **18**, 2141 (1993).

[121] T. Hirano, G. Shinozaki, J. Abe, and T. Kuga. Investigating statistical properties of light from high-efficiency light-emitting diodes. Prog. Crystal Growth and Charact. **33**, 339 (1996).